Jül-4404

Zentralinstitut für Engineering, Elektronik und Analytik (ZEA)
Systeme der Elektronik (ZEA-2)

Assessment of changes in the electro-optical performance of Silicon Photomultiplier (SiPM) modules after irradiation with cold neutrons

Shashank Kumar

JÜLICH
FORSCHUNGSZENTRUM

Assessment of changes in the electro-optical performance of Silicon Photomultiplier (SiPM) modules after irradiation with cold neutrons

Shashank Kumar

Berichte des Forschungszentrums Jülich; 4404
ISSN 0944-2952
Zentralinstitut für Engineering, Elektronik und Analytik (ZEA)
Systeme der Elektronik (ZEA-2)
Jül-4404

DE 464 (Master, Duisburg, Univ., 2017)

Vollständig frei verfügbar über das Publikationsportal des Forschungszentrums Jülich (JuSER)
unter www.fz-juelich.de/zb/openaccess

Forschungszentrum Jülich GmbH
Zentralbibliothek, Verlag
52425 Jülich
Tel.: +49 2461 61-5220
Fax: +49 2461 61-6103
E-Mail: zb-publikation@fz-juelich.de
www.fz-juelich.de/zb

Abstract

The detection and measurement of neutrons are vital in a wide range of fields including homeland security, radiation protection and scientific research. Small-angle neutron scattering (SANS) experiments have become important techniques in the investigation of the material properties on the atomic scale. For a long period ^{3}He based detectors were extensively used for neutron detection in these experiments, but due to the scarcity of ^{3}He, researchers started to look for alternatives. Scintillation based solid state detectors appeared as a prominent alternative. A neutron scattered by a sample under test impinges a scintillating material and initiates a nuclear reaction that produces secondary particles which in a second scattering process generate a light emission that can be detected by an underlying photodetector. By determining the neutron scattering angle, the momentum transfer of the scattered neutron can be identified. Using this information the investigated sample structure can be determined with very high spatial resolution.

These experiments using scintillation based detectors rely on efficient detection of photons, hence on the performance of photodetectors. Silicon photomultipliers (SiPM), having lower bias voltages compared to photomultiplier tubes (PMTs), being able to operate in high magnetic fields, offering the possibility of modular design, and yielding higher readout rates have the potential to become a photon detector of choice in these experiments. The concern regarding SiPMs to be used in these experiments is especially their neutron radiation hardness. When exposed to the neutron irradiation, the amount of defects caused by the impinging neutrons increases the dark count rate and diminishes the photon detection efficiency in the SiPM.

In order to study the performance degradation of SiPMs due to neutron irradiation, three different SiPM modules (two analog SiPM arrays provided by manufacturers *SensL* and *Hamamatsu Corporation* and one digital array by *Philips Digital Photon Counting GmbH*), were irradiated at the KWS-1 instrument of the *Heinz Maier-Leibniz (MLZ)* research reactor in Garching, Germany with cold neutrons having a 5Å wavelength. The scope of this work is to perform a quantitative comparison of the photodetection efficiency (PDE) for these SiPM technologies before and after irradiation with cold neutrons and assess the feasibility of the SiPM as the technology of choice for scintillation-based photodetectors.

Acknowledgements

This dissertation was written as a part of the fulfilment of the master degree in Embedded Systems Engineering, part of International Studies in Engineering at the University of Duisburg-Essen in collaboration with the Central Institute of Engineering, Electronics and Analytics - Electronic Systems (ZEA-2) at Forschungszentrum Jülich GmbH, Germany. My investigation for this work was sponsored by Forschungszentrum Jülich GmbH to whom I am thankful for this rich research experience.

I would like to thank all those who have made a contribution to this work, no matter how small.

I would like to take this opportunity to thank Prof. Dr.-Ing. Stefan van Waasen for his support and suggestions regarding different aspects of this work.

My deepest gratitude goes to my internal supervisor Dr.-Ing. Daniel Durini Romero for his continuous encouragement, nutritional support and invaluable discussions.

I am also thankful to Prof. Dr.-Ing. Andreas Czylwik for his readiness to become the second examiner of this work.

Moreover many thanks to Jakob Smitz and his workshop team at the Central Institute of Engineering, Electronics and Analytics - Electronic Systems (ZEA-2) for their prompt help.

Furthermore a big “Thank you” is not enough for my family and friends. I am grateful to them for all their encouragement, never ending love and the great moments.

Last but not least, I would like to thank my better half, Shalini for believing in me all these years and for supporting me through all my decisions. This work is dedicated to her.

Contents

List of Figures

List of publications derived from this work

1. D. Durini, C. Degenhardt, A. Palomino-Razo, **S. Kumar**, A. Feoktystov, H. Frielinghaus, H. Rongen, M. Schlösser, S. van Waasen "Assessment of the photodetection performance of different silicon photomultiplier technologies under irradiation with cold neutrons" poster, *Nuclear Science Symposium and Medical Imaging Conference (NSS/MIC)*, Strasbourg, France, 29.10 - 05.11.2016.

2. D. Durini, C. Degenhardt, M. Herzkamp, A. Palomino-Razo, **S. Kumar**, H. Nöldgen, A. Feoktystov, M. Streun, A. Erven, S. van Waasen "SiPM-based Scintillator Detectors for Small Angle Neutron Scattering Experiments" oral session, *Emerging Technologies Communications Microsystems Optoelectronics Sensors (ETCMOS)*, Warsaw, Poland, 28. - 30.05.2017

3. **S. Kumar**, D. Durini, C. Degenhardt, S. van Waasen, "Photodetection characterisation of SiPM technologies for their application in scintillator based neutron detectors" poster, *19th International Workshop on Radiation Imaging Detectors IWORID,* Krakow, Poland, 02.-06.07.2017

I. Introduction

A neutron is a chargeless subatomic particle having almost zero dipole moment. If interacting with soft or condensed matter, these properties causes a neutron to penetrate deep, as it will exclusively interact with atom nuclei. Neutrons are isotope sensitive and, having a magnetic moment, they get scattered from magnetic structures [1]. The latter makes neutron scattering a good choice for studying the structure of different materials.

Small angle scattering was discovered in the late 1930s by A. Guinier during X-ray diffraction experiments on metal alloys [2]. Development of neutron scattering techniques for material research started in the 1960s. Since then, this technology has evolved gradually over time. It involves four basic steps after neutron generation, namely monochromation, collimation, scattering and detection. With this technique, a neutron beam is scattered by a sample and the resulting scattering pattern is analyzed to get the information about the sample under investigation. It can be utilized to investigate microstructures of near optical scale (micrometers) and up to near atomic scales (nanometers). For these applications, neutrons generated in research nuclear reactors using monochromatic neutron beams, or time of flight instruments at pulsed neutron sources can be used [3].

Small-angle neutron scattering (SANS) technique has managed to grow rapidly and evolve into a sophisticated method of characterization for studies in thermodynamics and morphology [3]. It has wide application range in the research field, e.g. in the environment, energy, medicine, electronics and manufacturing industry. The ability to provide statistically averaged information on structures allows the investigation of biological molecules such as proteins, micelles and polymers. By tracking e.g. the cholesterol, these experiments could be utilized to improve chances of developing successful drugs for Alzheimer's disease in cooperation with pharmaceuticals. In combination with X- ray scattering technique, neutron scattering has led to the determination of antibody structures. This has successfully enabled the manufacture of efficient vaccines used to improve the immunity system of very young or elderly people [4].

1.1 Problem and Objective

The basic principle for detection of scattered neutrons is to convert neutrons into charge or photons by nuclear reactions. For a long time neutron detection material of choice was ^{3}He due to its high detection efficiency (70%) for thermal neutrons and good gamma radiation discrimination ratio ($\sim 10^{-6}$) [5], but low worldwide availability and increased cost enticed scholars to search for alternatives. There are two types of current detector developments, one focused on converter materials with gas proportional detectors and other focused on converter materials with scintillator-based detectors. Scintillator-based solid state detectors are so far the most promising alternative available [5]. When cold or thermal neutrons interact with a scintillating material (e.g. GS20 glass ^{6}Li enriched cerium activated (Ce^{3+}) scintillator [6]) then two secondary particles, a tritium ^{3}H and an α particle, as well as additional energy of 4.7 MeV are produced. These secondary particles undergo additional scattering process with the Ce^{3+} atoms producing visible photons isotropically. The visible photons produced in such a way can be detected by an underlying photodetector. This leads to the possibility to determine the scattering angle and the reconstruction of the structure of the sample under investigation. The schematic representation of a scintillation based solid-state detector proposed to be used in SANS experiments is shown in Fig. 1.

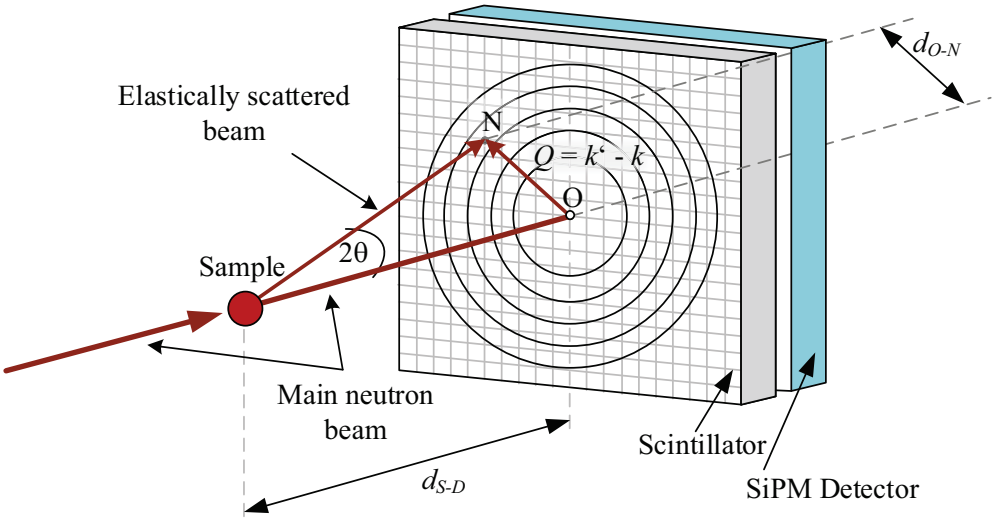

Fig. 1 Schematic representation of a scintillation based solid-state detector proposed to be used in small angle neutron scattering (SANS) experiments [7]

Conventionally, photomultiplier tubes (PMTs) have been used for photon detection in these experiments but their limitations namely sensitivity to the magnetic field, operating voltages in kilovolts, and complex mechanical structures, has motivated to look for other viable options. Recent investigation [7] on the dark signal characterization of the SiPM technology, has proposed an attractive alternative based on pixelated photon sensing with efficient low-intensity light detection. SiPM consists of an avalanche photodiode array fabricated on a silicon substrate and is capable of detecting near single photon events [8][9]. These solid state photodetectors are immune to high magnetic fields, have relatively low power consumption, and offer a superior spatial resolution. In this work the photodetection efficiency (PDE) performance of three different SiPM arrays has been studied in the range between the ultraviolet and the near infrared region of the spectra before and after their irradiation with cold neutrons (wavelength $\lambda_n = 5$ Å or energy of $E_n = 3.27$ meV) up to a dose of 6×10^{12} n/cm^2. The dark signal performance of the same three technologies was previously assessed and reported in [7].

1.2 Outline of the study

This thesis is divided into five chapters. Chapter 1 introduces SANS experiments and neutron detection developments along with proposed scintillation-based detectors and utilization of SiPM technologies that serves as motivation for this work.

Chapter 2 covers the theoretical background related to this test, which includes properties of the neutron, neutron scattering experiments and an overview of SiPM photodetectors and their electro-optical characteristics as well as their radiation hardness.

Chapter 3 introduces the specification of sensors used to carry out this test. Later in the chapter, a description of the measurement setup, method and procedure envisaged to achieve the desired task are revealed.

Chapter 4 includes the test results and the detailed analysis of the photon detection efficiency under the effect of neutron irradiation.

Finally, in chapter 5 the summary of this work are formulated alongside suggestions regarding future research to be performed.

II. Theoretical background

2.1 Neutrons

The discovery of the neutron by James Chadwick in 1932 was one of the important milestones in nuclear physics. Neutrons together with protons are called nucleons. Neutrons have a mass of 1.0097 a.m.u (atomic mass unit) or 1.6749×10^{-27} kg, spin ½, magnetic moment -1.9132 μ_N (nuclear magneton), and zero charge [1]. The charge neutrality and magnetic moment of a neutron allows for investigation of magnetic properties of matter. A chargeless nature of a neutron enables it to penetrate deep into the matter without interacting with an atom. Furthermore, nuclear forces are of very short range so the neutron can easily travel to the centre of the soft or condensed matter (e.g. polymers, surfactants, micelles, biological matter etc.) because the size of a scattering centre (i.e. a nucleus) is typically 100,000 times smaller than the distance between centres of two neighbouring atoms [10].

Neutrons can be produced commonly by a nuclear reactor or by a pulsed spallation source. In the first case, continuous neutrons are produced by nuclear fission reaction whereas, in spallation, the collision of high energy protons with heavy atoms produces neutrons [3]. The energy spectra of neutrons are depicted in the following table.

Quantity	Unit	Definition	Ultra cold	Cold	Thermal	Epithermal
Energy E_n	meV		0.00025	0.25 to 25	25	1000
Temperature T	K	E/K_B	0.0029	12	290	12,000
Wave vector k	$Å^{-1}$	$(2mE)^{1/2}/h$	0.011	0.35 to 3.5	3.5	22
Wavelength λ_n	Å	$h/(2mE)^{1/2}$	570	18 to 1.8	1.8	0.29
Velocity v	m/s	$(2E/m)^{1/2}$	6.9	220 to 2200	2200	14,000

Table 1: Characteristics of Neutrons at Selected Energies [11]

Where K_B = Boltzmann's constant
m = mass
h = Planck's constant
E = energy

The wavelengths of cold or thermal neutrons (e.g. λ_n = 5 Å) are such that they lead to a "point like" scattering. Signal-to-noise ratio is also high for the neutron detection. The energy (E_n~ 3.27 meV) is too small to change the energy of an atom and also no transfer of kinetic energy takes place (in the case of elastic scattering). A neutron can exhibit also wave properties including reflection, refraction and diffraction (exploited in SANS). These properties altogether make it a suitable candidate to be used in experiments based on neutron interactions that provide the capability to see inside the material at atomic level [10].

2.1.1 Neutron Interaction

Techniques derived from the neutron interaction play a crucial role in solving some of the major global challenges along with other methods of probing material structure. Whenever a neutron

impinges a sample, there can be three possible outcomes: namely, transmission, absorption, or scattering of the neutron. The latter of these is the area of interest for this study.

The scattering of neutrons occurs in two ways, either through an interaction of unpaired electrons with the magnetic moment of the neutron (magnetic scattering) or through interaction with the nucleus (nuclear scattering) [1].

The scattering of a neutron by a free nucleus depends upon how much effective area of a nucleus it gets. This is defined in terms of a cross section σ, measured in barns (1 barn = 10^{-29} m^2). Because nucleus behaves as a point scatterer, due to the fact that the range of the nuclear interaction between the neutron and the nucleus is tiny compared with the wavelength of the neutron, scattering is equally likely in every direction i.e. it is isotropic, provided the neutron hits within this area [10].

The scattering of neutrons by matter can affect both the momentum and the energy of both, the neutron and the matter. This process is classified into two types, namely elastic and inelastic scattering based on the energy transfer.

In the case of elastic scattering, there is no exchange of energy between the neutron beam and the nuclei of matter, i.e. the energy of the neutron is conserved. This kind of neutron-nucleus interaction can be assumed only when the nuclei in the matter are fixed. In contrast to this, if atoms are moving when a neutron hits, they can impart energy to the neutron. This is called inelastic scattering [1].

As explained in [10], the magnitude of the wave vector k is related to the neutron velocity by the equation $k = 2\pi mv/h$ where h is Planck's constant and m is the mass of the neutron. The momentum transfer is $h\,Q / 2\pi = h\,(k - k') / 2\pi$, where k is the wave vector of the incident neutrons and k′ is that of the scattered neutrons. The so-called scattering vector Q can be defined by Eq. 1.

$$Q = k - k' \tag{1}$$

If we consider elastic scattering, then k= k′ and scattering vector will be calculated from Eq. 2.

$$Q = 4\pi \sin\theta / \lambda_n \tag{2}$$

For finding the scattering vector, scattering angle 2θ (~0.2˚to 20˚ [3]) is required as described in Fig. 1. In order to determine θ, the important information delivered by the detector will be the distance between the scattered and the main neutron, $d_{O\text{-}N}$ (refer to Fig. 1). The basic investigating principal of elastic scattering is to measure the scattering intensity with varying scattering angle. SANS instruments can be also called as low Q instruments [3].

2.1.2 Small Angle Neutron Scattering (SANS)

Since the development of SANS technique in the mid-1970s, the unique information that it provides is essential in making progress in contemporary material science. It is a well-established technique for probing structure and dynamics of the condensed matter. For investigation of the dynamic properties of matter, inelastic scattering is used; whereas elastic scattering is used for the investigation of structural properties.

Cold and thermal neutrons (E_n~1-25 meV & λ_n~1.9-9 Å) are ideally suited for these experiments due to the fact that a longer wavelength corresponds to a better interaction with the nuclei while keeping the sample properties intact because of the low energy. Fig. 2 [10] depicts a comparative information of different structural probing techniques.

New advances in electronics, data handling methods and computers have made SANS a sophisticated "user-friendly" characterization method. It has a wide range of application fields, not only limited to polymers, complex fluids and biology, but also has an impact on energy, environment, electronics, manufacturing industry etc., in collaboration with other research techniques [4].

A typical reactor based SANS technique involves four basic steps: monochromation (producing monochromatic neutron beam, i.e. of a single wavelength), collimation (aligning the neutron beams in a specific direction or parallel to each other), scattering (interaction of neutron beams with the sample), and at last detection of scattered neutrons by the detectors.

2.1.3 Neutron Detectors

Absorptive reaction with prompt reactions, activation process and proton recoil are three major categories for detection of neutrons [12]. Proton recoil (also known as elastic scattering reaction) is used in SANS. Accordingly, detector´s atom nuclei create ions by exchange of energy due to collision with neutrons. In general, the principle of detection is the production of secondary particles by nuclear absorption reactions and the generation of an electrical signal caused by their interaction with certain elements or detection media.

A neutron detector can be based on a solid, liquid or gas-filled detection media. Most of the neutron detectors use ^{3}He gas as a converter material, mainly due to its high cross section (high interaction probability) with neutrons, very low gamma (noise) sensitivity, and its nontoxic nature [5].

$$^1n_0 + {}^3He_2 \longrightarrow {}^1H_1 + {}^3H_1 + 765\ keV \tag{3}$$

The nuclear reaction described by Eq. 3 between a neutron and the helium gas produces two charged particles that are accelerated through the gas towards the anode of the bias gas container that finally create a signal through multiplication. The exact spot this scattered neutron hits the detector active area can be defined by using appropriate algorithms and the output signals of the ^{3}He gas tubes. Since last decade, use of ^{3}He gas in homeland security by the USA has led to a dramatic shortage and skyrocketing price raise. This has triggered all major neutron research centers to search for viable options. As reported in [5], three different alternatives are under development: namely, scintillation technology, solid boron-10 converters and BF_3 filled gas detectors.

Scintillation based detectors work on the principle of conversion of neutrons into photons. A scintillator material exhibits the property of re-emitting absorbed energy as photons (light). A scintillator based detector using GS20 (glass) ^{6}Li scintillator enriched (content 95% ^{6}Li) with cerium (Ce^{3+}) is suggested in [7]. The chemical reaction of this scintillator with the neutron is written in Eq. 4, where a neutron ($^1n_0$) interacting with the nucleus of the ^{6}Li atom produces a tritium ($^3H_1$), an α ($^4\alpha_2$) particle and an additional energy of 4.7 MeV.

$$ {}^{1}n_0 + {}^{6}Li_3 \longrightarrow {}^{3}H_1 + {}^{4}\alpha_2 + 4.7MeV \quad (4) $$

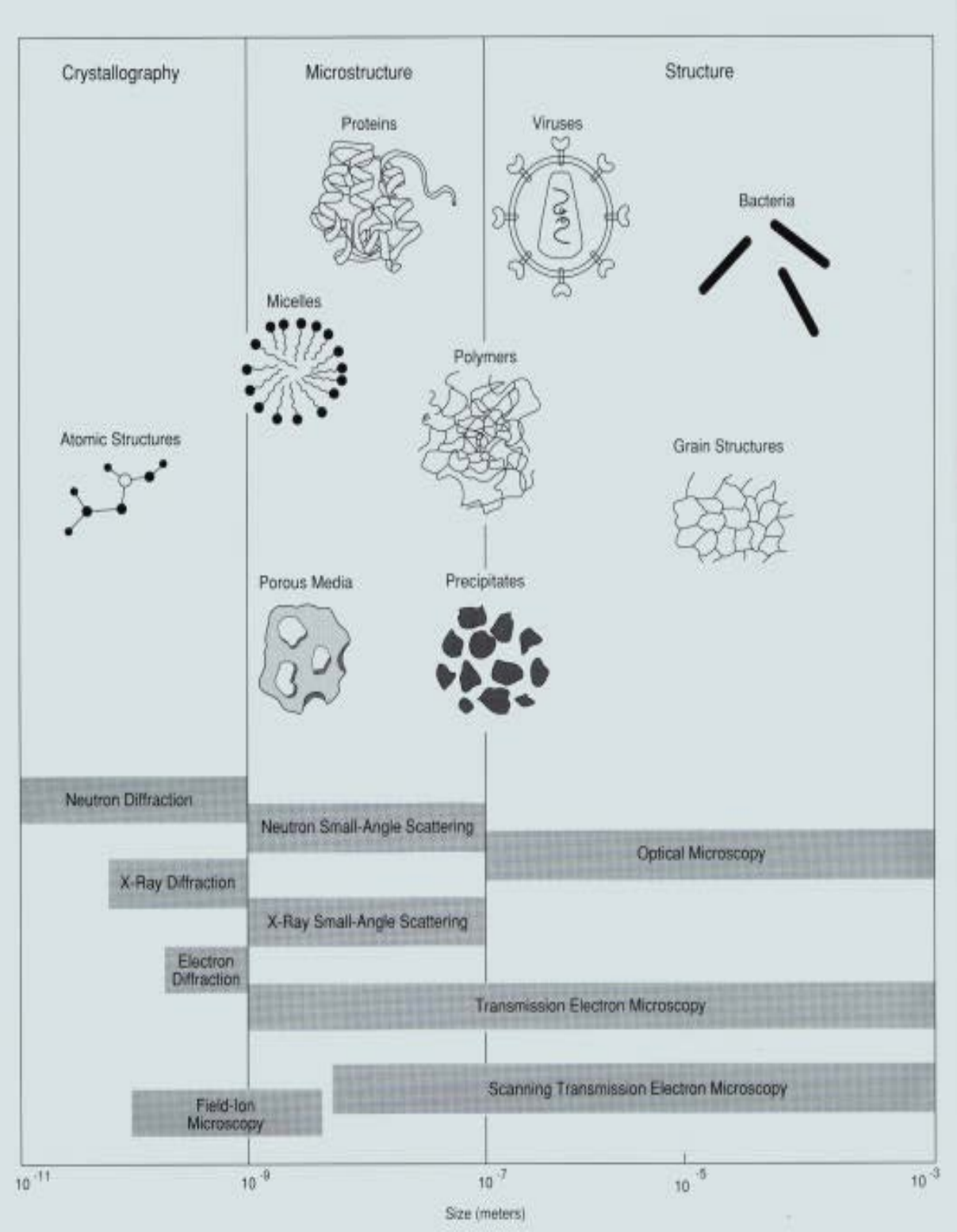

Fig. 2 Comparative picture of SANS with other technique [10]

When any of the resultant secondary particles (tritium and α) interacts with the Ce atoms, their energy is partially transferred to cerium atoms. The excited cerium, once ionized, in the process of stabilising to the ground state emits visible photons in the blue range with a wavelength of 395 nm isotropically, as shown in Fig. 3 [7].

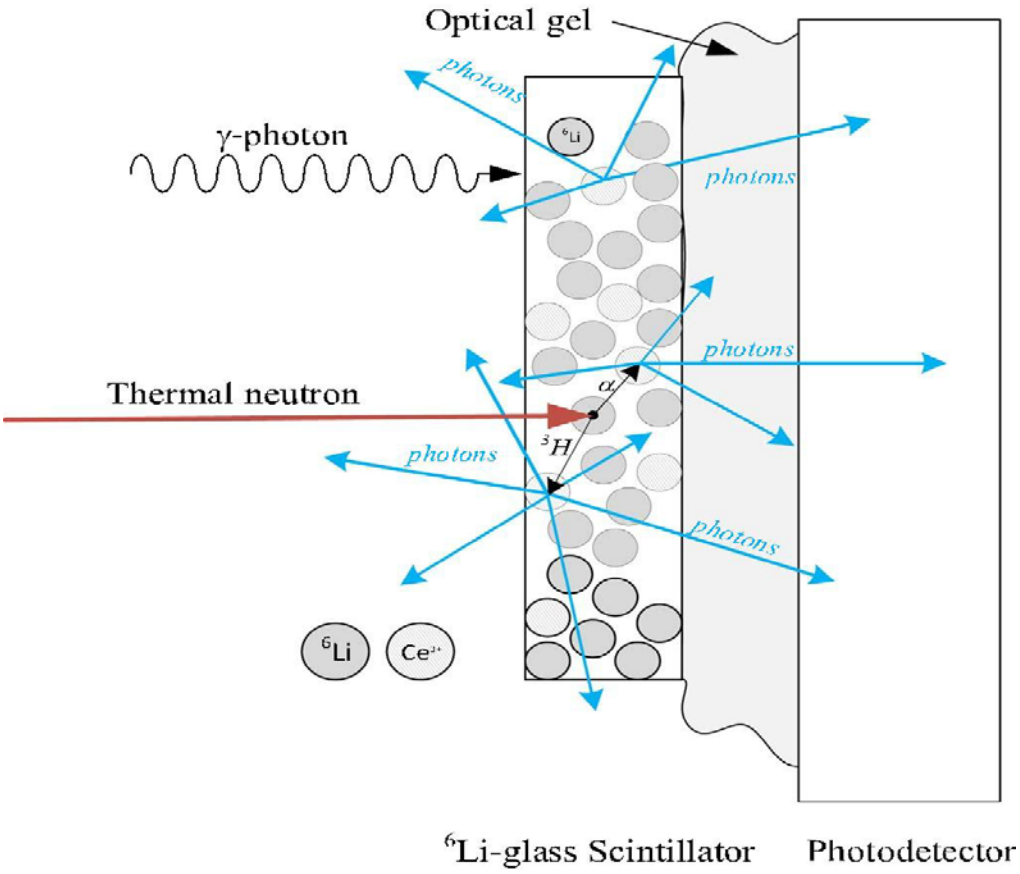

Fig. 3 Schematic representation of the visible radiation dispersion for the ^{6}Li-glass scintillator, optically coupled to a photodetector using an optical glue to diminish reflection and refraction losses. An additional gamma–photon produced by the environment is also shown that undergoes the same reaction in the scintillator as the neutron does, producing additional blue photons to be detected by the photodetector [7]

This type of detectors has a comparable performance to ^{3}He based gas proportional detectors, and can be designed due to its modular structure in any desired shape. It does not contain any toxic materials and, most importantly does not need ^{3}He gas [6].

The photons generated within the ^{6}Li glass can be detected by an underlying photodetector and hence, the exact spot of neutron impinging on the scintillator can be traced by detecting the spot of maximum emission of generated photons. In order to achieve low scattering vectors (see section 2.1.1) either the wavelength should be long or the neutron scattering angle should be low (or both). A low angle can be measured using a good area detector with good spatial resolution [3].

Traditionally, vacuum PMTs and multianode photomultiplier tubes (maPMTs) have been serving to detect photons generated within the solid state scintillators, but their inoperability in

magnetic fields, the high power consumption, electromechanical complexity and high cost initiated the search for alternative photodetectors [13]. The first effort towards this was the development of Avalanche Photodiodes (APDs) [14-16] but their gain limitation (of few thousands) and consequently the low photon flux sensitivity (~10^6-10^7 photons/s) has led to further advancements. Single photon avalanche photodiode (SPAD) [17] and SiPMs were proposed whose photon sensitivity is comparable to the one from PMTs.

The idea of making an array of SPAD gave rise to a new kind of photodetectors which not only has equivalent gain with PMTs, that means the ability to count single photons, but also provides signals proportional to the impinging photon flux [8][9]. Silicon photomultipliers (SiPM) appear to be a promising photodetector technology in neutron detector applications based on scintillation processes because of their properties such as their ability to operate in high magnetic fields, their low power consumption, low cost, and modular designing option.

2.2 Silicon Photomultipliers (SiPM)

The SiPM is a state of the art sensor that is capable of quantifying extremely low light signals due to its high internal gain (~10^6). It was introduced first in the late 1990s by the Russian scientists Z. Sadygov and V.M. Golovin [8][9]. The working principle of this solid state detector is based on internal photoelectric effect i.e. the generation of charge induced by photon radiation. It is a pn-junction diode operating in reverse bias mode beyond the breakdown voltage (refer to sec. 2.2.3.1) and evolved from several generations of silicon photodetectors developments of PIN photodiodes and avalanche photodiodes [18]. Fig. 4 shows a gradual evolvement of a Geiger-Mode Avalanche Photodiodes (GM-APD), elementary microcell of a SiPM. Since its introduction, it has been undergoing a rapid development improving its performance in terms of its photon detection efficiency (PDE) and suppressing undesirable characteristics (dark count rate, cross talk and afterpulse, explained in sec. 2.2.3). The traits of SiPM make it an attractive alternative for applications where operation in magnetic field is required [19] and space and power consumption are limited, e.g. in medical imaging, high energy physics, biophotonics, hazard and threat detection and LiDAR [20][21].

The SiPM technology also known by various acronyms given by researchers and manufacturers, such as:

- G-APD or GM-APD (Geiger mode avalanche photodiode)
- MPPC (multi-pixel photon counter), as named by the company Hamamatsu
- SSPM (solid state photomultiplier)
- AMPD (avalanche micropixel photodiode)
- DPC (digital photon counter), as named by the company Philips
- SPAD (single photon avalanche photodiode)

2.2.1 Topology

This solid state device integrates an array of small microcells (~1000/mm^2) connected in parallel on the same silicon substrate, where each microcell (SPAD or GM-APD) is an avalanche photodiode operating in Geiger mode (~10-20% above breakdown voltage) and connected in series with a quenching resistor (or an active quenching circuit). The lack of proportionality is overcame in the way that each GM-APD detects photons independently and delivers a current output which is a sum of signals produced by each individual GM-APD. In order to explain the working of a SiPM, understanding of its microcell's structure, the basic building block of a SiPM, is necessary.

Significant developments in microelectronics has enabled various approaches to design the microcells of a SiPM [22]. A generic microcell structure is depicted in Fig. 5 and a matrix of these cells builds a SiPM as shown in Fig. 6. The microcell structure can be of two types: n^+/ p /π/ p^+ or p^+/n/n-epi /n^+. In the first structure that is optimised for green light detection, a p^+silicon substrate is used to build an n^+/ p -junction on a lightly doped p-type (π) epitaxial layer; whereas in another type, a p^+/n-junction is built on a lightly doped n-type epitaxial layer grown on a n^+ substrate. A p^+/n/n-epi /n^+ type structure has the highest detection sensitivity for the blue light [18].

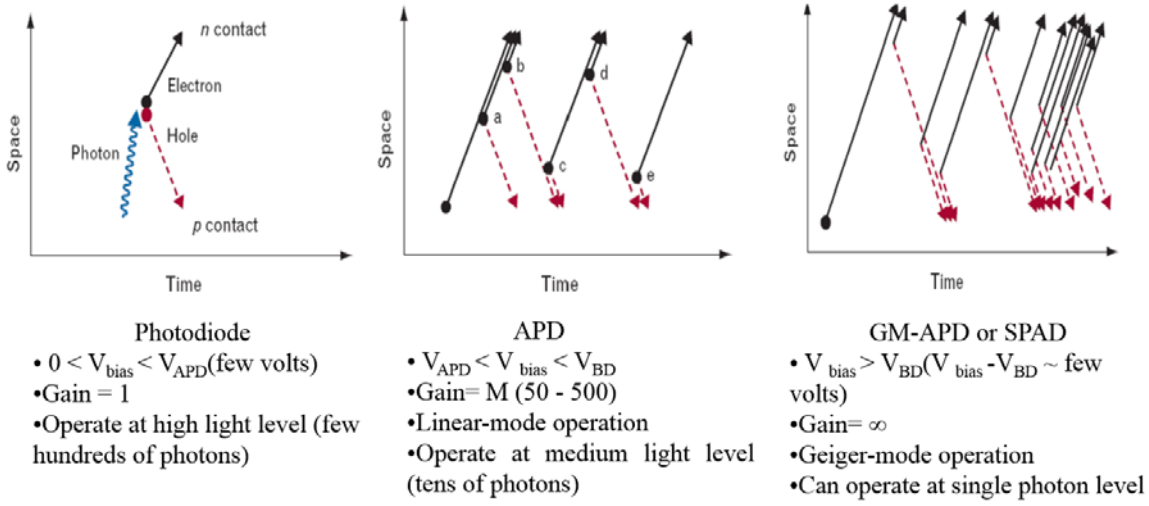

Fig. 4 A picture showing gain characteristics and overview of development in solid state photodiodes [23]

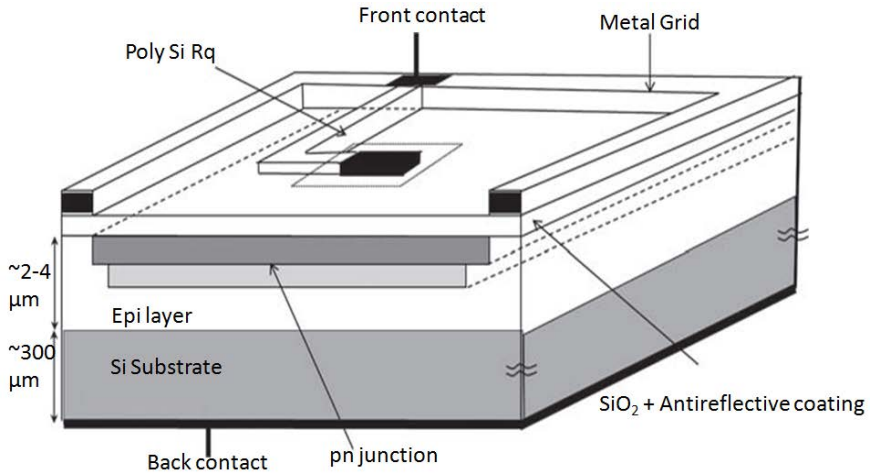

Fig. 5 Sketch of a generic SiPM elementary microcell [18]

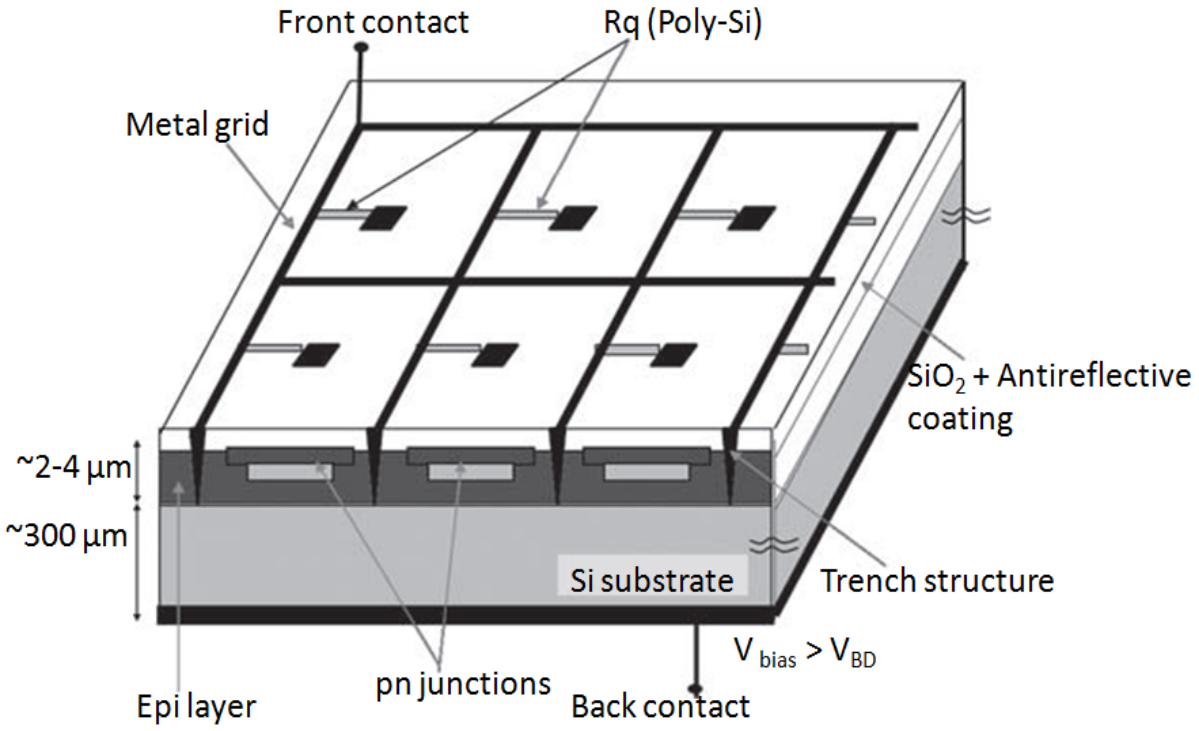

Fig. 6 Sketch of a generic SiPM (array of microcell) structure [18]

2.2.2 Operation

Whenever a photon (E_{ph} >1.1eV) illuminates a microcell (GM-APD) of a SiPM, it produces through the photoelectric effect an electron-hole pair (EHP). The exited electron in this way makes a transition from the valence band into the conduction band [24]. This process is depicted in Fig. 7. If the photoactive microcells are given a sufficiently high electric field, which is done by applying reverse bias (breakdown voltage), and the EHP is generated in this high field area (achieved by the sensor design or diffuses into it), it can lead to an avalanche breakdown due to impact ionization mechanism: a sufficiently energetic hole or electron, knocking out another bound electrons from the bound state and promoting them to the conduction band leading to new EHP generation, see Fig. 8. The latter leads to an exponential increase in the current observed. This current is proportional to the electric field present in the depletion region, which is generated by the sum of the intrinsic electric field (due to reverse biased pn-junction) and the extrinsic electric field (caused by applied bias voltage). If the bias voltage is increased further (10-20% above breakdown voltage, electric field ~10^5V/cm), it triggers a self-sustained avalanche resulting in a high current (mA) originating from photo-generated carriers (EHP). This mode of operation is called Geiger mode in analogy with the Geiger counter [27].

The generated current rises swiftly (in ns) and remains continuous until the electric field becomes low again or the bias voltage drops below breakdown voltage. This is achieved in the case of digital GM-APDs using active quenching circuits by adding a suitable circuit to the diode so that it can cease the current and prepare it to detect another photon by rising bias voltage above the breakdown again.

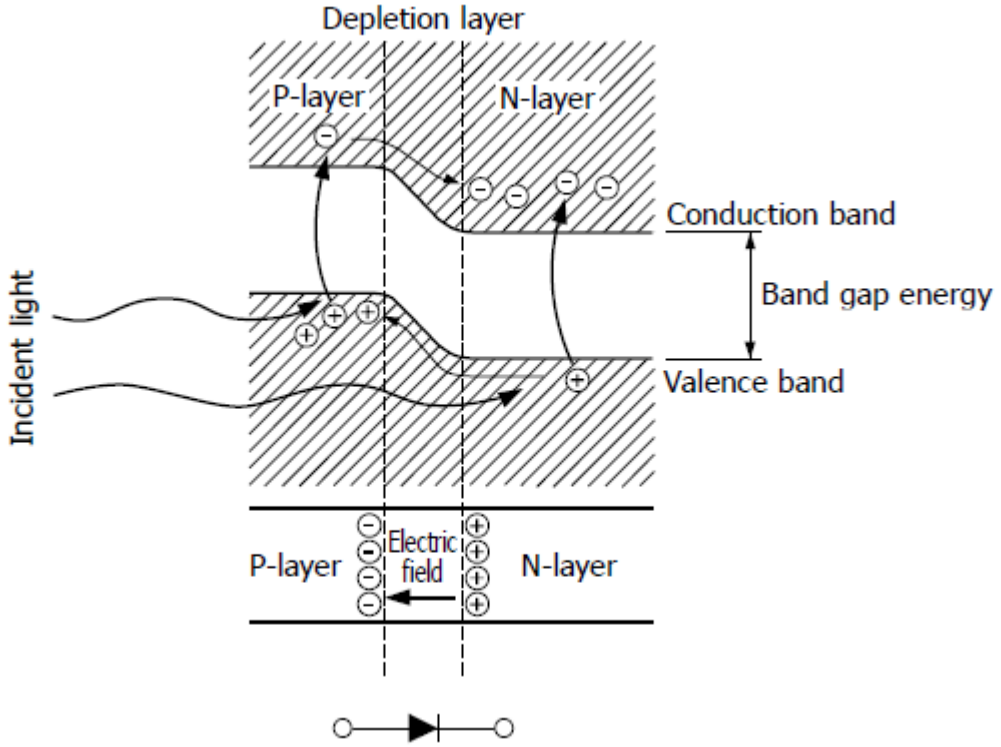

Fig. 7 Visualisation of electron-hole pair generation due to photon illumination in a pn-junction [25]

In active quenching, i.e. the process of restoring the required electric field for the Geiger-mode operation by depleting the pn- junction from generated charge carriers, a fast discriminator detects the arrival of a photon by sensing the avalanche current and gives a digital output. After that, it lowers the bias voltage quickly below the breakdown voltage [28]. In contrast to this, in passive quenching, a series resistance is connected with the microcell to limit the diode current and to quench the avalanche. This resistance is called quenching resistor (Rq). The restoring of the biasing voltage depends on the value of this resistor and also on the diode capacitance [18]. The time taken by the microcell to recover is the so called recovery time of the cell or its dead time, analogous to the fact that during this period the diode will be blind and will not detect any photon events.

The process of breaking down, quenching and resetting a GM-APD can be understood from Fig. 9.

A simplified electrical circuit of a SiPM using passive quenching is shown in Fig. 10. The total output current (I) of the SiPM represents the superposition of the currents (i_1,i_2,...i_n) of fired SPAD cells, which will deliver measurement of light flux incident on the SiPM, as depicted in Fig. 11.

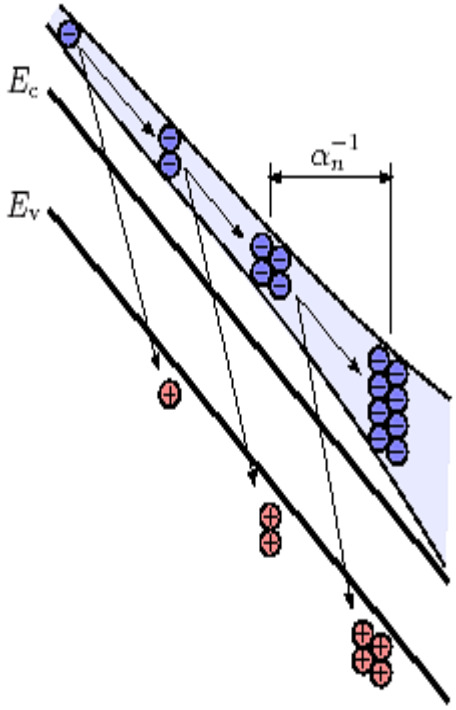

Fig. 8 Symbolised process of a pure electron induced impact ionization avalanche generation. After an electron is accelerated along an average distance α_n^{-1} it undergoes a collision and the excess energy produces a new electron-hole pair. Consecutive collisions can trigger an avalanche [26]

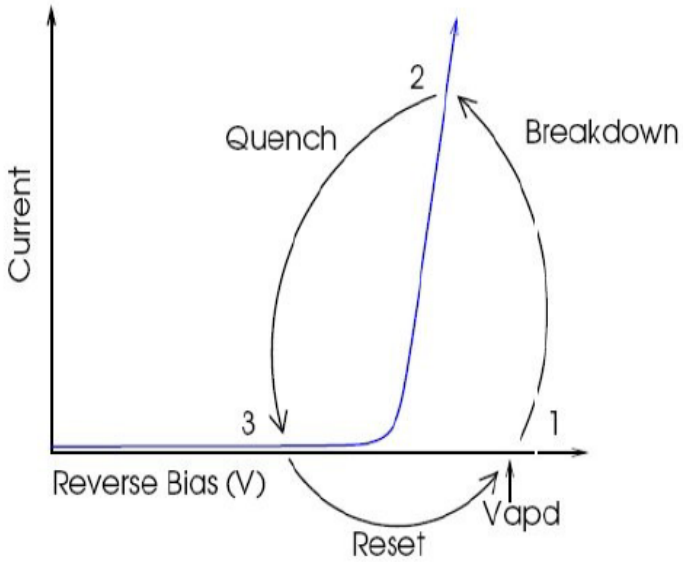

Fig. 9 Breakdown, quench and reset cycle of a SPAD working in Geiger mode [21]

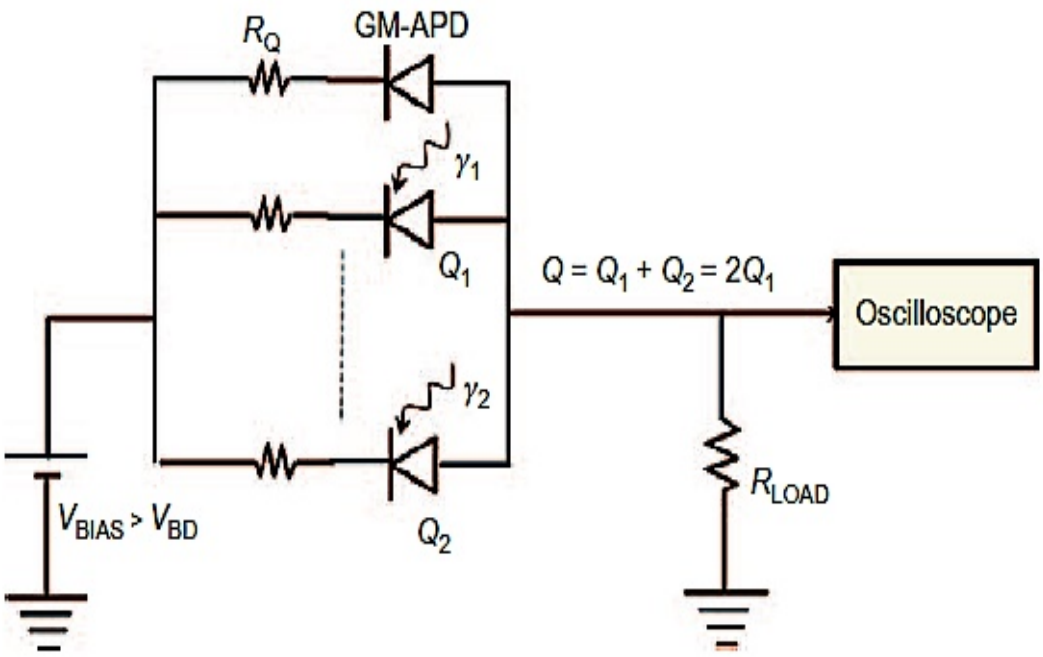

Fig. 10 Simplified electrical circuit of a SiPM (the external circuit composed of load resistance R_{Load} and oscilloscope is also represented) [18]

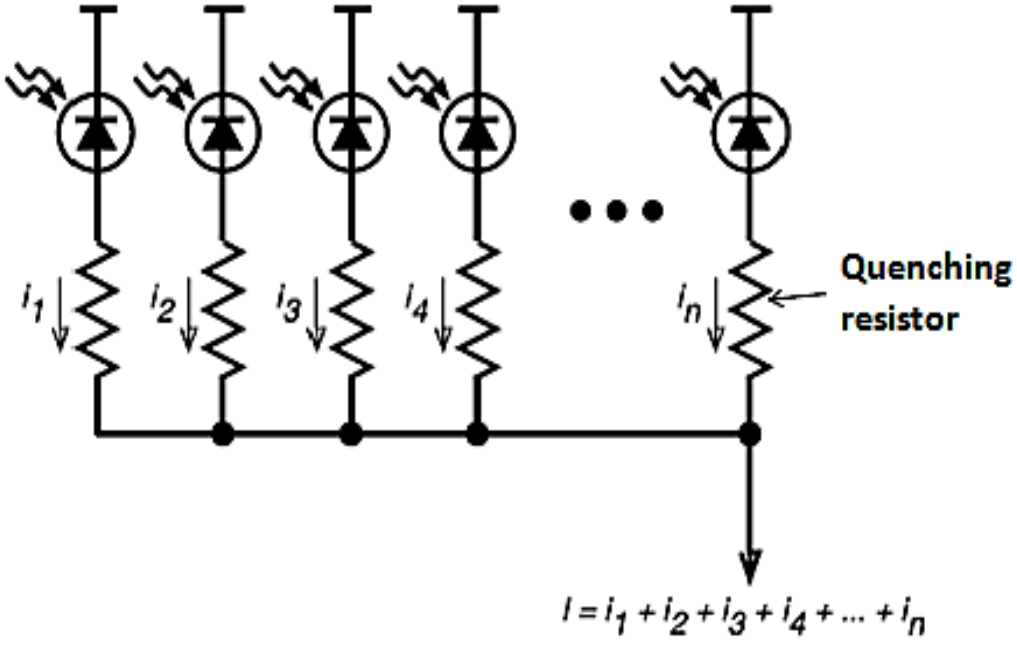

Fig. 11 Visualisation of the SiPM current which is the sum of multiple SPADs connected in parallel and each SPAD in series with a quenching resistor [29]

2.2.3 Characteristics

We will discuss here the characteristics of the SiPM that are relevant to this study. These can be categorized as electrical (breakdown voltage, photocurrent, gain, & noise) and optical such as photon detection efficiency, PDE.

2.2.3.1 Breakdown Voltage

As explained before an analog SiPM consists of hundreds of thousands of photosensitive microcells, each connected to a quenching resistor in a passive quenching circuit, and having a single short-circuited output. The reverse bias voltage, which onset the avalanche, is defined as breakdown voltage (V_{BD}) (see Figs. 12 and 13) [30]. The breakdown voltage can be determined experimentally, either by the I-V (current vs. voltage) curve method or by the G-V (gain vs. voltage) curve method. Nevertheless, discrepancy of 100-200 mV has been reported between these approaches [32][33]. The first method uses turning on of the avalanche mechanism, whereas turning off of avalanche is considered in the other method. Due to this fact, it can be assumed that the I-V method will estimate a higher value of V_{BD} compared to the G-V method.

A matter of concern for the operating condition of the SiPMs is the temperature variation. During this test, we have observed variations in the breakdown voltage due to temperature shifts, and this behavior has been investigated and reported also in [33][34]. The explanation for this temperature effect is as follows: with the rise in temperature, the carrier looses its energy due to increased scattering with the crystal lattice resulting in hindrance to impact ionization. A corollary to this is the requirement of more electric field to overcome this energy loss, so the breakdown voltage gets increased. Hence, temperature induced breakdown voltage fluctuation has to be taken into consideration for characterizing SiPMs.

2.2.3.2 Photocurrent

Photogenerated carriers are not the only ones responsible for the output current in SiPMs. The other sources of charge are noise or background signal of SiPMs due to the fact that the relevant information is given by photogenerated carriers only. This noise is mainly constituted by thermally generated carriers [7]. Therefore, the total output current of a SiPM will be the sum of the current in the absence of light i.e. I_{dark} (in dark condition) and the current induced by light (I_{ph}), as evaluated by the Eq. (5).

$$I_{total} = I_{dark} + I_{ph} \tag{5}$$

Where I_{dark} is dark current and I_{ph} stays for photocurrent. For determination of the effective photocurrent of a SiPM other noise sources like crosstalk and afterpulse also have to be addressed, which is done in the section dealing with noise.

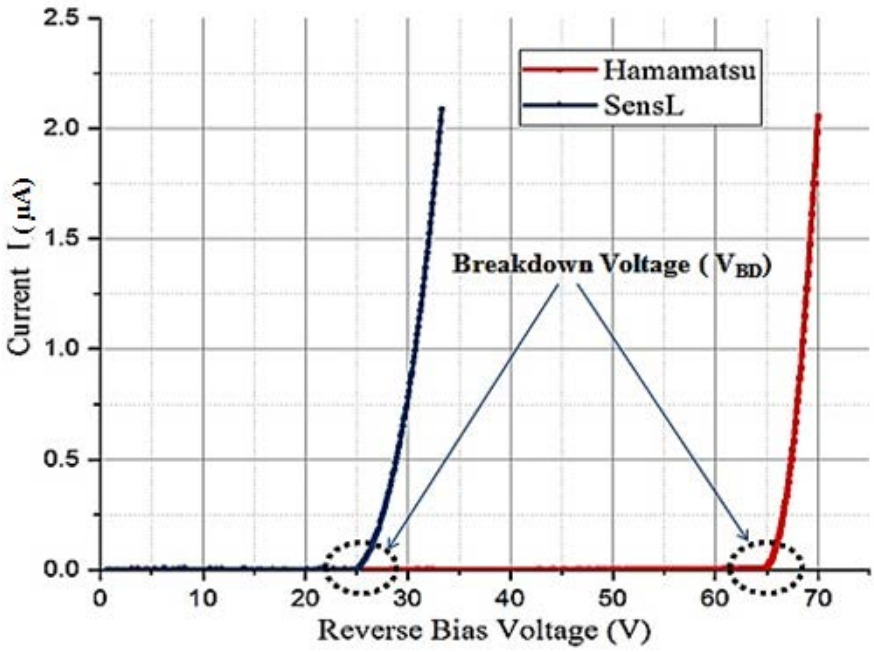

Fig. 12 I-V curve showing breakdown voltages of SiPMs used for performing this test.

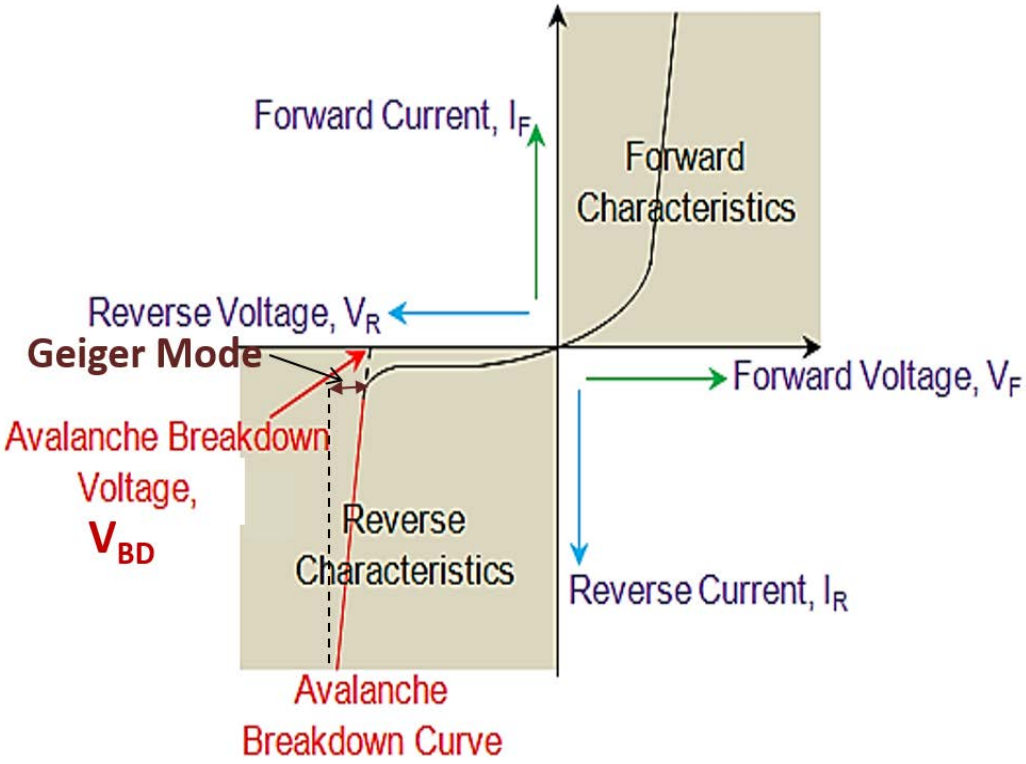

Fig. 13 I-V curve for a pn-junction depicting avalanche breakdown [31]

2.2.3.3 Gain

In the Geiger mode, the avalanche process is self-sustained because of very fast multiplication of carriers. In order to be able to calculate the amount of avalanche events or counts, a Fig. of merit is introduced, and can be defined as the number of charge carriers created during an avalanche discharge of a microcell and is mathematically expressed by Eq.(6) [18].

$$G = \frac{Q}{e} = \frac{Cj * \Delta V}{e} = \frac{Cj * (V_{BIAS} - V_{BD})}{e} \quad (6)$$

Where C_j = junction capacitance
V_{BIAS} = bias voltage
V_{BD} = breakdown voltage
ΔV = V_{BIAS} - V_{BD} = overvoltage
Q = charge developed in one avalanche event
e = elementary charge

It can be observed from Eq. 6 that gain is a function of the junction capacitance of the SiPM, and the applied overvoltage (ΔV). Experimentally, the gain can be calculated as the ratio of current integral over time related to the elementary charge from Eq. 7.

$$G = \frac{Q}{e} = \frac{\int I(t)dt}{e} \quad (7)$$

The temperature dependency is also relevant for this parameter. The breakdown voltage varies with temperature so the gain will vary with temperature proportional to $V_{BD.}$ Thus, there is indirect temperature dependence on the gain of a SiPM [33][34]. Although, if the overvoltage is held constant, temperature dependency of the gain will be only due to junction capacitance.

2.2.3.4 Noise

- **Dark count rate**

Dark signal is the main source of noise in SiPMs, created mainly by thermally generated carriers [7]. Dark count rate is defined as the rate at which the dark pulses (events due to non-photo generated carriers) occurs. It is denoted by DCR and is often quoted as pulse rate, typically expressed in kilocounts per second (kcps) or megacounts per second (Mcps). In Geiger mode, it is related with current as represented by Eq. 8 [18]. One can estimate the limitation of minimum detectable light flux from the value of DCR. Its value doubles for an increase in temperature of approximately 8°C [7]. In order to achieve better performance, this noise should be minimized. It can be reduced by improvement in the production technique in terms of impurities and crystal defects or lowering of operating temperature [13][24][33][34].

$$I = e * G * DCR \quad (8)$$

Where I = current
e = elementary charge
G = gain of SiPM

DCR = dark count rate

- **Crosstalk**

Crosstalk is a correlated noise in neighboring microcells of a SiPM that occurs due to an avalanching microcell causing an avalanche in a second microcell. There are two types of causes for crosstalk to take place. The first type is named optical crosstalk, and it occurs due to electro-luminescent emission (i.e. photons emitted in the avalanche breakdown of one cell) of the photons during an avalanche discharge by a microcell, and inducing another avalanche simultaneously in neighboring microcell either by direct propagation of photons to the adjacent cell or indirectly by internal reflection from the bottom of the device [35]. This process is shown schematically in Fig. 14. This violation of independence of microcells can be minimized by using some proper light insulating material in between microcells (e.g. trenches) at the cost of decreasing the active area of the cell [18].

However, delayed crosstalk will occur due to lateral diffusion of photo-generated carriers by primary photons to adjacent cells.

The crosstalk increases with the gain as avalanche processes created by higher electrical fields emit more photons. It contributes to the output signal, which is a superposition of the signals from primary and secondary fired microcells.

- **Afterpulse**

Impurities in silicon and crystal lattice defects can act as carrier traps for the charge carriers created during an avalanche process. These charge traps can release carriers after sometime (several ns), initiating an avalanche in the same cell and resulting in an increased output signal. Although it appears similar to delayed crosstalk it is different because of the different physical process that causes it [33]. It is dependent on cell recovery time and over voltage, due to the fact that more charge trapping will occur with an increase in overvoltage and followed by a decrease in recovery time. If afterpulse happens due to long delayed carrier, it can lead to false PDE measurement.

2.2.3.5 Photon Detection Efficiency (PDE)

Photon detection efficiency (PDE) is the probability with which a SiPM produces an output signal in response to an incident photon. PDE is a key parameter for every detector. For a sensor to deliver an output signal, the photon has to impinge upon its active sensing area to generate a charge carrier, and this charge carrier must trigger an avalanche process. Hence, it is defined by the product of the fill factor, the quantum efficiency and the triggering probability. Eq. 9 shows how to calculate the PDE of a SiPM [18].

$$PDE = QE * P_{01} * FF \tag{9}$$

Where QE is quantum efficiency, P_{01} is triggering probability and FF is the fill factor.

Quantum efficiency is the measure of likelihood that an impinging photon creates an electron-hole pair within the active area of a microcell in a SiPM. As silicon transmission efficiency, i.e. the photon absorption depth is wavelength dependent so QE also depends on the incident photon's wavelength resulting in change in PDE with different wavelengths of incident light [18].

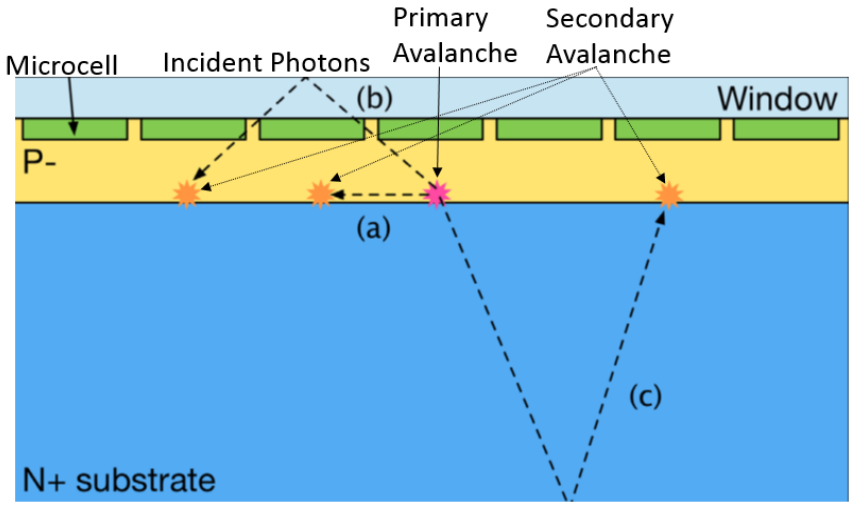

Fig. 14 Visualisations of a) direct optical crosstalk (diffusion of photons to a neighboring microcell) and in direct optical crosstalk b) reflected from the window material on the top of the sensor (usually epoxy or glass), or c) reflected from the bottom of the silicon substrate [21]

Triggering probability takes into the account that not every carrier traversing the high field region initiates an avalanche. It is the joint probability of electron and hole to trigger an avalanche when they pass through the depletion region. It has been found that the chances will increase if the electric field within the depletion region is high and the photogeneration process will happen in the p side of the junction (because of high ionization rate of electrons) [18].

The complete area of the sensor cannot be utilized to detect the photons due to different artefacts including guard-rings, quenching circuitry, metal connections etc. which results in the presence of the dead area. Hence, the effective area differs from the total area. The ratio of the active area to the total area of the sensor is referred to as fill-factor of the microcell. Advancement in fabrication techniques in silicon electronics (especially smaller technology nodes) has led to a substantial increase in the fill-factor giving rise to high PDE of SiPMs.

2.2.5 Radiation hardness

It can be defined as the extent of radiation tolerance of a material i.e. the limit of the radiation that does not significantly change the properties of the material or its sensing capability. Insufficient radiation hardness is the main concern for the SiPM technology when it comes to a prolonged exposure to impinging neutrons, as it is the case in SANS experiment.

Radiation can lead to damage in silicon detectors which can be classified as displacement damage on the one side, or ionization damage on the other. Displacement of silicon atoms from their lattice sites is called displacement damage and is also referred to as bulk damage. In ionization damage, trapping of charge at the surface happens due to drifting or diffusing, which is produced by energy absorbed by the layer [36].

When a neutron interacts with the ^{30}Si isotope, a process called nuclear transmutation take place. This approach was used for uniform n-type doping of silicon in the past. Here a ^{30}Si isotope transmutes into ^{31}Si, which finally decays into ^{31}P, releasing an additional β particle (beta decay) as described by Eq. 10 [37].

$$^{30}Si + {}^{1}n_0 \longrightarrow {}^{31}Si \longrightarrow {}^{31}P + \beta \quad (10)$$

The radiation damage in the SiPM due to neutron irradiation has been extensively studied and its major impact is on the silicon detector´s dark current [7][38]39].

The dark current of a SiPM as shown in [7], can be expressed using Eq. 11.

$$|I_{dark}| = \alpha_p \left\{ q\, A_N \left(\frac{n_i^2}{N_D} \sqrt{\frac{D_p}{\tau_{r\_p}}} + N_{def}\, W_{SCR}\, \sigma_n\, C_n\, T^2 e^{\left(\frac{-(E_C - E_T)}{k_\beta T} \right)} \right) \right\} \quad (11)$$

Where α_p = the hole impact ionization coefficient
q = elementary charge
n_i = intrinsic silicon doping concentration.
A_N = area of the p-n junction
K_B = Boltzmann constant.
N_D = donor doping concentration in the n-type substrate (or n-well).
Dp = diffusion coefficient for holes
τ_{r_p} = recombination lifetime for minority holes.
N_{def} = defect concentration within the SCR
W_{SCR} = depth of the space charge region
α_n = defect cross section
C_n = universal constant
T = temperature
E_c-E_T = emission frequency of minority holes due to the presence of defects within the space charge region

In Eq. 11, the dark current is dominated by the diffusion current term (i.e. the diffusion coefficient Dp and recombination lifetime τ_{r_p}) and the generation term from the defects within the space charge region (or depletion region). As the electron concentration will increase due to the increased ionized phosphorous concentration, the recombination time of the minority carriers (τ_{r_p}) will decrease [7].

It has been reported in [40] that thermal neutrons induce damage in silicon atoms mainly in form of point defects leading to an increase in the term N_{def} in Eq. 11.

Under the consideration of these two effects, an increase in dark current can be expected. Besides dark current, radiation induced defects can affect the operating voltage (caused by the change in doping concentration) and charge collection efficiency (due to the fact that defects may act as charge trapping centers) leading to variations in the SiPM performance.

III. Experimental Apparatus and Procedure

In the first part of this chapter, we will discuss the different SiPM detectors under study. Later in the chapter, complete experimental setup, performed methods and the measurement procedure will be explained.

3.1 SiPM Arrays

Gaining a better comparative quantification of the radiation effects in SiPMs, we used SiPM arrays fabricated by different manufacturers. The main comparative characteristic of the SiPM arrays used for this investigation is listed in Table 2, their physical description can be seen in Fig. 15. The detailed analysis of these sensors is done in the following section.

The SiPM arrays had been already irradiated with cold neutrons (λ_n = 5 Å) in a previous experiment to perform this test (see Table 3), reaching an overall neutron dose of 1.9×10^{12} n/cm² for the *SensL* array, 6×10^{12} n/cm² for the *Hamamatsu* MPPC array, and 1.85×10^{12} n/cm² for the Philips digital photon counter (PDPC) array. The entire active area of the SiPM arrays was not exposed to neutrons, rather only the limited central area was exposed. The remaining parts were covered by a boron carbide plate (see Fig. 16) in order to have a reference and be able to assess the changes not caused by neutron irradiation simultaneously.

Sensor	**Analog**		**Digital**
Model	ARRAYC-30035-144P-PCB.	S12642-0808PB-50	DPC3200-22-44
Manufacturer	SensL	Hamamatsu	Philips
No. of Pixel	144	64	64
Active area	3×3 mm^2	3×3 mm^2	3.8×3.2 mm^2
Microcell size	35µm×35µm	50µm×50µm	59.4µm×64µm
Breakdown voltage[1]	~ 25V	~ 65V	~ 25V
No. of microcells	4774	3464	3200

1 at room temperature

Table 2: A comparative data overview of all the SiPM arrays utilized for this experiment.

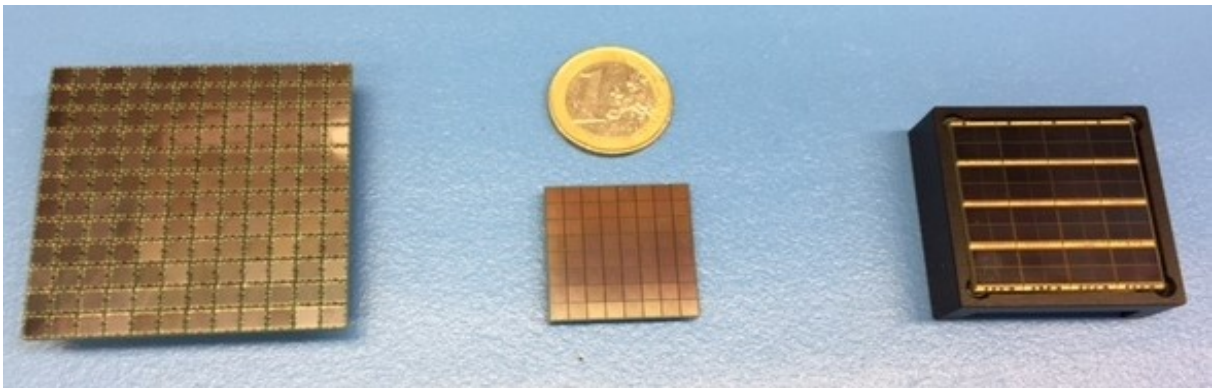

Fig. 15 Physical appearance of sensors provided by SensL, Hamamatsu & Philips (left to right)

Irradiation Phase	**Duration of the irradiation phase**	**Neutron Flux [n.cm^{-2}.s^{-1}]**	**Interruption of the flux to perform dark signal measurements?**	**Periodicity of dark signal measurem-nts**	**Accumula t-ed neutron dose [n/cm^2]**
1	150s: 30s for each of the first 5 measurements	9.96×10^6	Yes	Once after each 30 s of irradiation	1.5×10^9
2	60 minutes	9.96×10^6	No	Once every 30 s	3.7×10^{10}
3	Rest of the irradiation time	10^8	No	Once every 300 s	Up to 6×10^{12}

Table 3: Irradiation time steps and doses used during the consecutive phase 1, 2 and 3 [7].

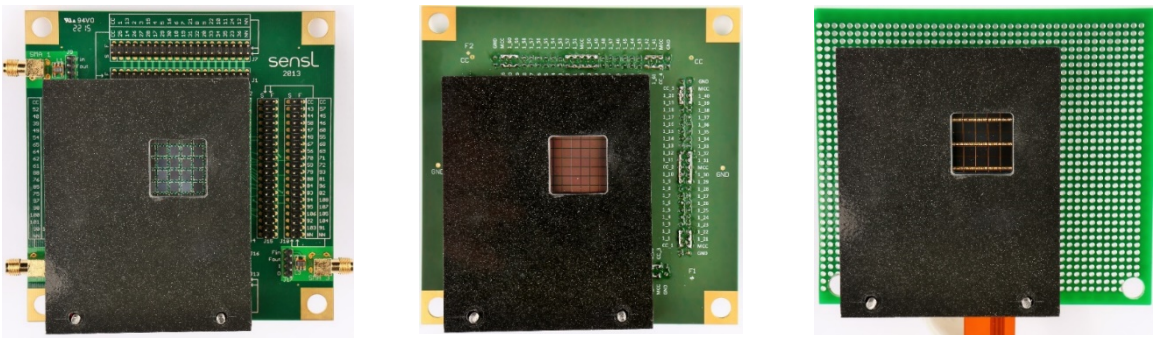

(a) (b) (c)

Fig. 16 Photographs of the SiPM technologies, covered by a 6 mm thick boron-carbide plate (neutron absorbent): (a) SensL 12×12 array mounted on a break-out board; (b) Hamamatsu 8×8 array mounted on a break-out board designed for this experiment; (c) Philips DPC3200-22-44 sensor [7]

3.1.1 Analog SiPM Array

Two analog SiPM arrays, both working with passive quenching mechanisms and having high PDE (~35%) have been chosen for the test. Having a low dark count rate and a high PDE, SensL-C series *ARRAYC-30035-144P-PCB* was tested in the study. It is an array of 144 SiPMs, each having an active area of 3×3 mm and having 4774 (35µm each) microcells (SPAD). The detailed specification of the microcell of the sensor can be found in Table 4.

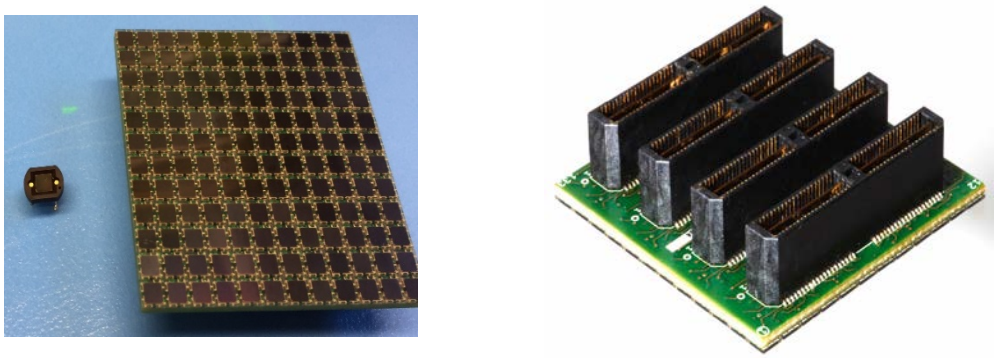

(a) (b)

Fig. 17 (a) 12×12 SensL ArrayC-30035-144P-PCB alongside its one SiPM (pixel) (front view) (b) its 80 way connector (back view)

Connections to each sensor are provided by four Samtec 80-way connectors, type *QTE-040-03-F-D-A*. These connectors mate with the *Samtec QSE-040-01-F-D-A* board-to-board connector and the Samtec EQCD High Speed Cable Assemblies. The 144 SiPM sensors have all substrate connections (cathodes) connected together to form a common I/O [41]. The array and its connector are shown in Fig. 17. This array has an area of 50.2×50.2 mm^2. The physical dimension of its microcells and the array is depicted in Fig. 18. Beside standard output (S) this sensor offers an additional fast output (F) which can be used for fast count rates (Fig. 19 (a)). For the ease of connection between the array and the readout system, a breakout board is also provided by the manufacturer, namely *MicroFB-30035-SMT*. This breakout board (see Fig. 19 (b)) has board to board connectors which route all signals from each pixel to the corresponding header pin. The breakout board can be mounted on an optical bread board also with the help of given four 7mm holes at the corners.

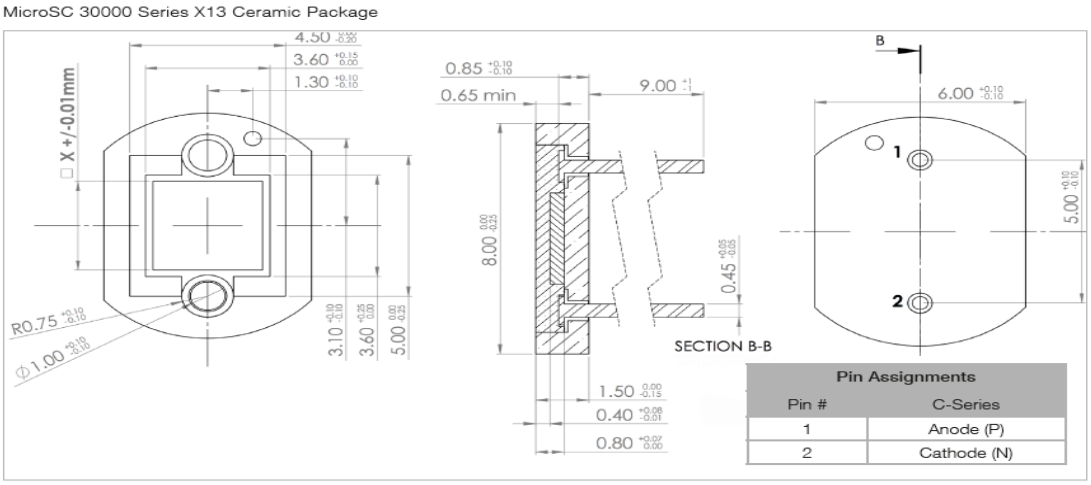

(a)

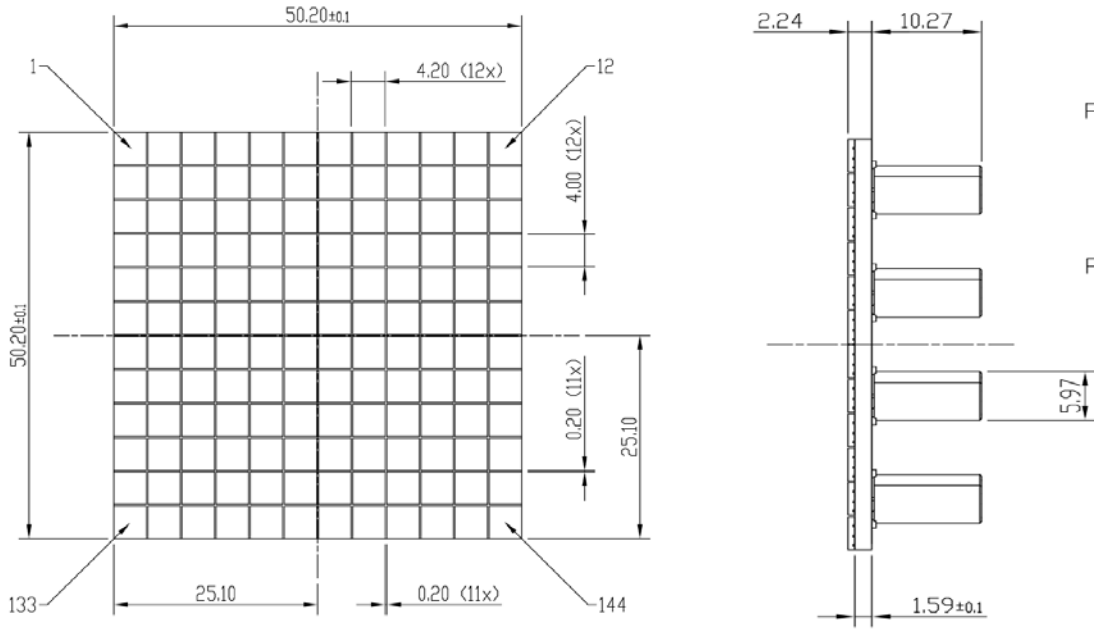

(b)

Fig. 18 (a) Schematics for the ArrayC-30035-144P-PCB microcell (b) Schematics for the 12×12ArrayC-30035-144P-PCB [41]

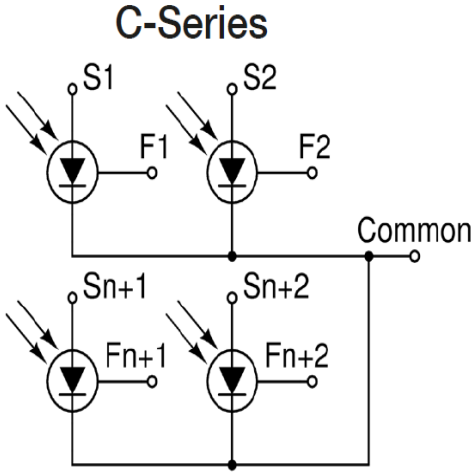

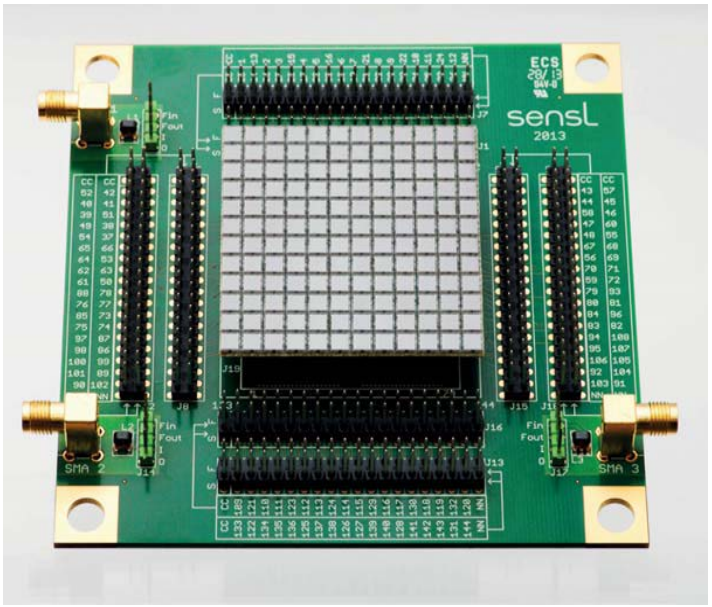

(a) (b)

Fig. 19 (a) Schematic presentation of the 12×12 ArrayC-30035-144P-PCB electrical connection (S – standard output, F – fast readout output); (b) SMT array Breakout Board (MicroFB-30035-SMT) [41].

Parameter[1]:	**Value: Max. / typ. / min.**	**Unit:**
Sensor active area	3 x 3	mm²
Microcell size	35	mm
No. of micro-cells	4774	
Micro-cell fill-factor	64	%
Packaging	Surface mount package (SMT)	
Soldering conditions	lead-free, reflow soldering process compatible	
Package dimensions	4 x 4	mm²
Recommended operating temperature range	80 /- / -40	°C
Encapsulate refractive index @ 589 m,	1.54	
Breakdown voltage (V_{br})[2]	24.40 / 24.65 / 24.90	V
Recommended overvoltage range(voltage over V_{br})[3]	1/2.5/5	V
Max. Current level	15	mA
Spectral range	800/-/320	nm
Peak Wavelength (λp)	420	nm
Dark Current[4]	443 / - / 154	nA
Dark Count Rate (DCR)(@V_{BIAS} = V_{br}+2.5V)	860 / - / 300	KHz
Capacitance[5] (anode-cathode) (@V_{BIAS} = V_{br}+2.5V)	850	pF
PDE[6] at λp (@V_{BIAS} = V_{br}+2.5V)	31	%
Gain (@V_{BIAS} = V_{br}+2.5V)	3×10^6	
Microcell recovery time[7]	180	ns
Temperature dependence of V_{br}[8]	21.5	mV/°C
Temperature dependence of Gain[9]	-0.8	%
Crosstalk (@V_{BIAS} = V_{br}+2.5V)	7	%
Afterpulse	0.2	%

1 All measurements made at 2.5V overvoltage and 21°C unless otherwise stated.
2 The breakdown voltage (Vbr) is defined as the value of the voltage intercept of a parabolic line fit to the current vs. voltage characteristic curve.
3 Please consult the maximum current levels when selecting the overvoltage to apply.
4 Dark current derived from dark count data as DC*M*q*(1+CT)*(1+AP), where DC is dark count, M is gain, q is the charge of an electron, CT is cross talk and AP is afterpulsing.
5 Internal capacitance of the sensor. Typically add 2-3pF for sensor in package. Listed by unique microcell size for each part version.
6 Note this is true "sensor PDE" which does not contain afterpulsing or crosstalk
7Time for microcell to recharge (90% to 10% of pulse peak amplitude).
8Calculated as the change in Vbr extracted from pulsed laser gain measurements.
9Quoted as the percentage change per degree C from measured value at 21°C

Table 4: Datasheet provided by the manufacturer for SensL *ARRAYC-30035-144P-PCB* [41]

Another analog SiPM used for this test is the chip on board type Hamamatsu KSX-I50024-E_S12642 Series *S12642-0808PB-50* array fabricated using through silicon via (TSV) technology. In this technology no wire bonding is used, which makes it very compact with small dead space (0.2mm) as compared to SensL (1.2 mm). Hamamatsu array has significantly reduced afterpulse and yields high PDE (35%) (refer to Table 5).

Parameter :	**Value:**	**Unit:**
Photosensitive area	3 x 3	mm²
Microcell size	50	μm
No. of micro-cells	3464	
Micro-cell fill-factor	62	%
Packaging	Chip on board (Surface mount type)	
Package dimensions	3.1 x 3.1	mm²
Recommended operating temperature range[1]	-20 to 60	°C
Encapsulate refractive index @ 589 m,	1.55	
Breakdown voltage (V_{br})	65±10	V
Recommended operating voltage(V_{op})	2.6	V
Spectral range	320 to 900	nm
Peak Wavelength (λp)	450	nm
Dark Count Rate (DCR)[2]	2-3	Mcps
Terminal capacitance	320	pF
PDE[3] at λp	35	%
Gain (V_{op}= V_{br}+2.6V)	1.25×10^6	
Temperature coefficient of reverse voltage	60	mV/°C
V_{op} variation between channel	±0.05 to ±0.15	V
Crosstalk (V_{op} = V_{br} +2.5V)	35	%

1: No condensation
2: The data will be measured by current.
3: Photon detection efficiency does not include crosstalk and after pulse.
5: Characteristics change with applied over voltage. Please refer to next section in detail.
6: Refer to the data attached for each product.

Table 5: Datasheet provided by the manufacturer for 8×8 Hamamatsu MPCC array *S12642-0808PB-50* [42]

This array also has a SAMTEC Header ST4-40-1.00-L-D-P-TR installed at the back side of the package, which makes it convenient to use, but the manufacturer does not provide any board to board connectors. The array with its pixels and the connector is shown in Fig. 20. Fig. 21 shows the schematic of this sensor. For sorting out this connection problem, we had an in-house developed customised break out board with connector analogous to the SensL breakout board (Fig. 22). This allowed to connect the array with another measurement set up and getting output signals easily.

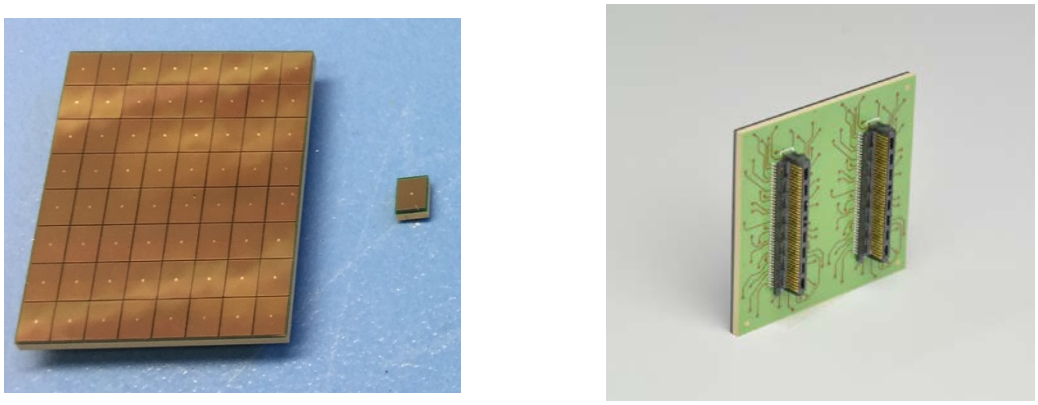

(a) (b)

Fig. 20 Photograph showing (a) Hamamatsu MPCC array S12642-0808PB-50 with its one SiPM (pixel) (front view) (b) HamamatsuS12642-0808PB-50 connector (back view) [42].

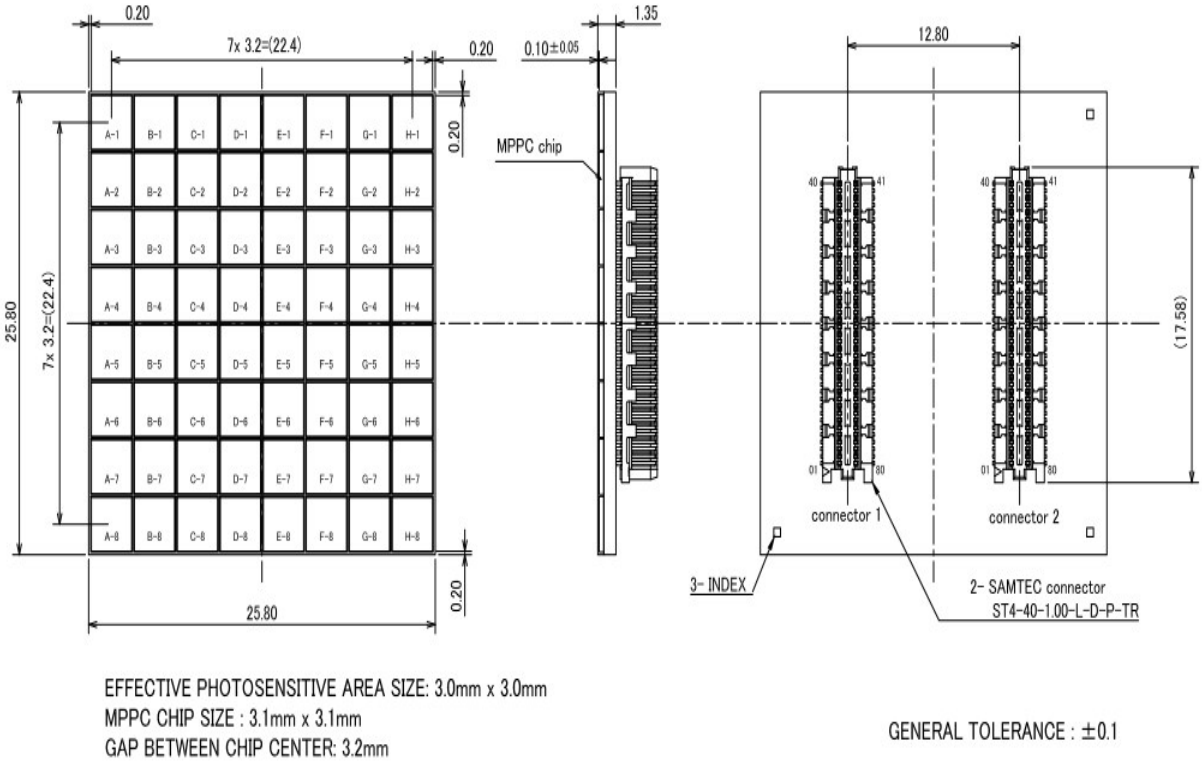

Fig. 21 Schematic of 8×8 Hamamatsu MPCC S12642-0808PB-50 array alongside its connector [42]

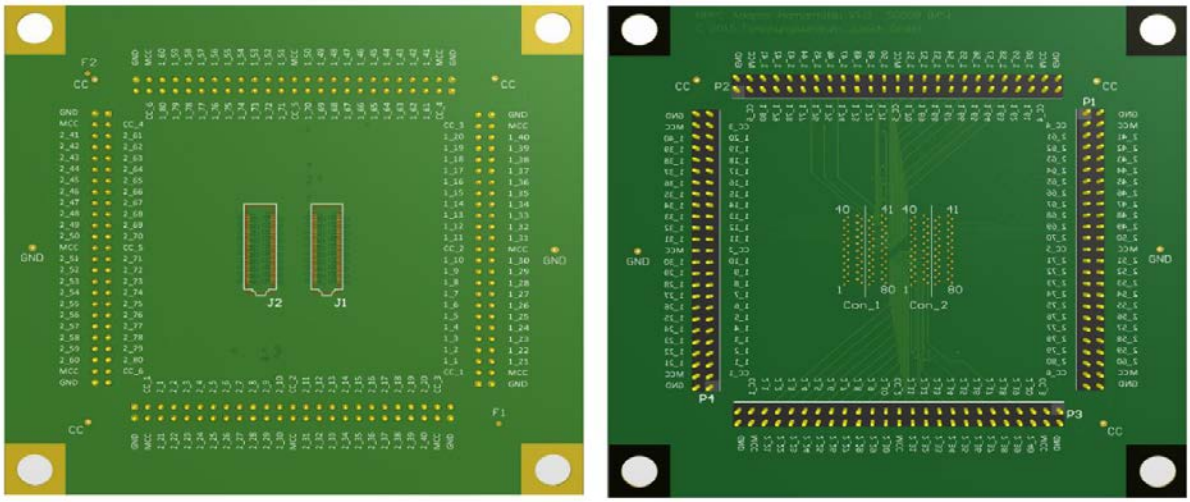

Fig. 22 Picture depicting the layout of the breakout-board designed at the ZEA-2 for the Hamamatsu 8×8 MPPC array S12642-0808PB-50

3.1.2 Digital SiPM Array

Philips Digital Photon Counting GmbH has developed a state of the art SiPM array with an integrated CMOS circuit for readout, making it a fully digital photon counting (DPC) detector. Each microcell has its own readout circuit and can be enabled or disabled separately from all the other cells for the photon counting. Its bias voltage adaptability makes it insensitive with temperature drifts [28]. The 8×8array *DPC3200-22-44* (Fig. 23) [43], which is modelled on active quenching mechanism with the use of transistors and a discriminator, is a leading technology in SiPMs. It offers time-to-digital conversion, good timing resolution of 40 ps and software control for effective dark-count suppression.

The manufacturer also provides a tile evaluation kit (TEK). Each DPC tile consists of 64 (8×8) channels, divided into 16 dies and further subdivision of a die into 4 pixels (Fig. 24). The array area is 32.6×32.6 mm^2 and each pixel has an active area of 3.8×3.2 mm^2 (schematics of PDPC tile is shown in Fig. 25). Its peak sensitivity is at 420 nm and it gives a PDE around 40%. The complete characteristics can be found in Table 6.

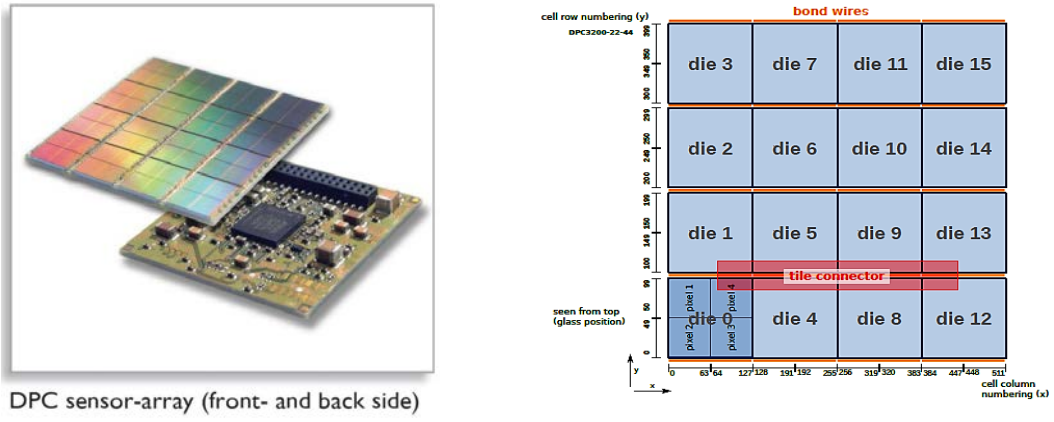

Fig. 23 The photograph shows a) picture of Philips DPC 3200-22-44 b) tile sensor layout of Philips DPC 3200-22-44[43].

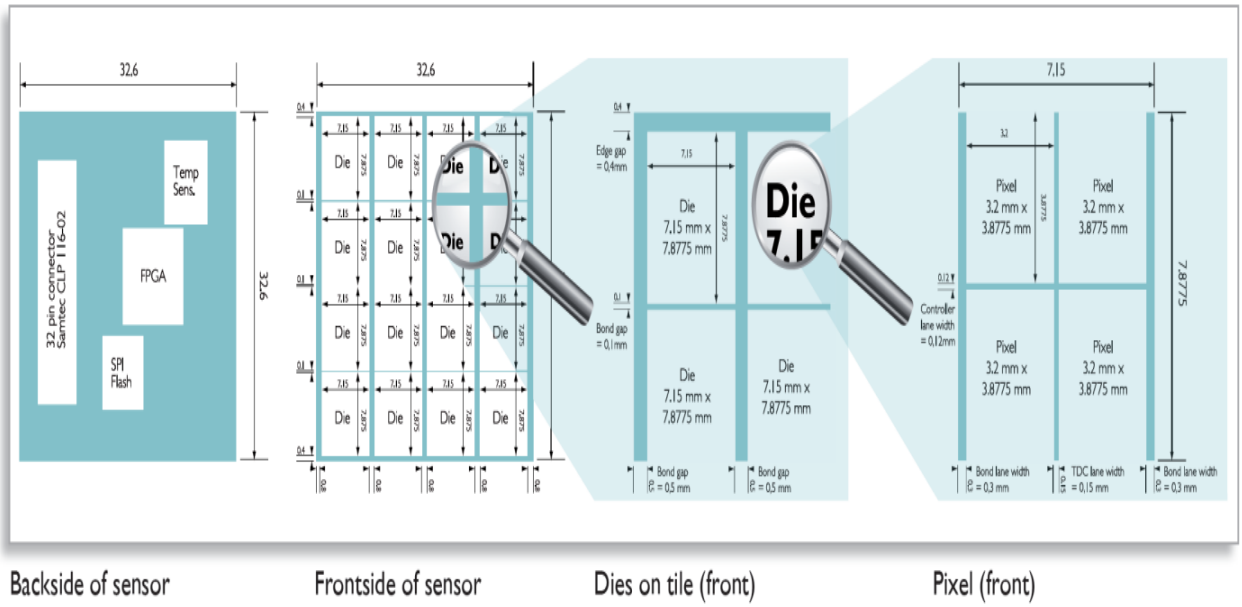

Fig. 25 Schematic of Philips DPC 3200-22-44 [43]

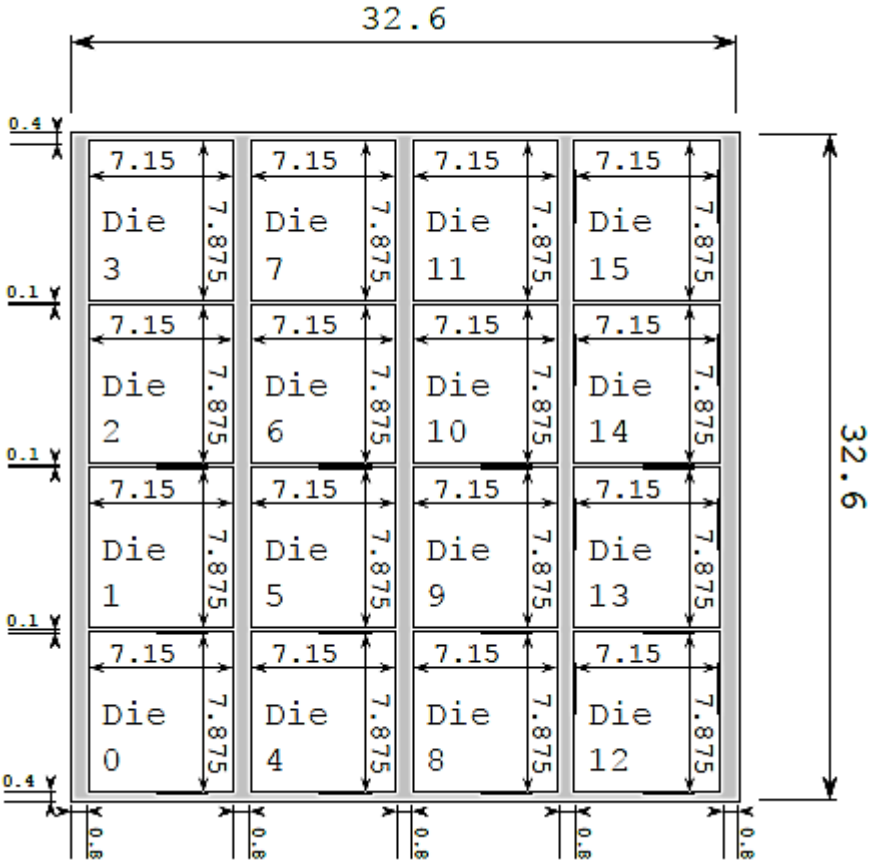

Fig. 24 DPC3200-22-44 tile dimension in mm (front view) [43]

Parameter	DPC3200-22-44
Outer dimensions	32.6 x 32.6mm^2
Pixel Pitch	4.0 mm×4.0 mm
Pixel Active Area	3.8 ×3.2 mm^2
Number of cells per pixel	3200
Cell size	59.4 x 32 μm^2
Spectral Response Range	380 nm – 700 nm
Peak Sensitivity Wavelength (λ p)	420 nm
Photon Detection Efficiency (PDE)	40 %
Pixel Fill Factor (already included in PDE)	54 %
Tile Fill Factor	75 %
Dark Count Rate (95% cells active)	< 5 Mhz / pixel at room temperature
Temperature Dependence of PDE	-0.33%/ °C in the range of 15 °C – 25 °C
Intrinsic Timing Resolution	44 ps
Operating temperature	0°C- 40°C

Table 6: Operation data of the Philips DPC 3200-22-44 module [43]

3.2 Apparatus

Three measuring systems, namely opto measurement system, electronic measurement system and tile evaluation kit (TEK), have been used for this experiment. Opto measurement system, used as a monochromatic light source to illuminate the sensors, is developed by *aSpect Systems GmbH [44]*, Germany and the TEK is provided by *Philips Digital Photon Counting GmbH [43]*, Germany, along with the digital sensor (PDPC) for their readout. The Electronic system was developed in frame of this work to read out analog sensors.

3.2.1 Opto Measurement System

We have used a customised measurement system (1.8×0.8×2.3m), primarily having a monochromatic light source and a lock-in amplifier based readout system. The purpose for the use of this system (Fig. 26) is to produce a uniform monochromatic light in the UV to NIR range of the spectra, which can be incident on detectors held under dark conditions at constant temperature. It consists of mainly seven parts. The schematic of the system is shown in Fig. 27.

- **Xenon arc lamp**

  It is a specialized gas discharge lamp, which emits white light seemingly close to sunlight, through an electric arc. Within it, xenon gas is ionized by applying high voltage, which leads to a discharge (arc) between metal electrodes in a glass bulb at high pressure and produces light. The 150 W lamp used is ozone free and is manufactured by *LOT* [45].

- **Optical Chopper**

  The chopper *Thorlabs MC2000* [46] serves to control the intensity of light coming from the arc lamp by periodically interrupting the light beam and modulate the light signal to be used for phase lock-in based readout. It uses a phased-locked loop motor speed control design to precisely maintain the chopping speed and phase of the reference signal (in this case 9 Hz, recommended by the manufacturer). It is synchronized with lock-in amplifier to increase the signal to noise ratio.

- **Monochromator**

  In order to transmit the mechanically selectable narrowband of light chosen, produced by the xenon lamp, a monochromator is used. The light coming out of the chopper is fed to the monochromator, whose output is light of a desired wavelength. It is based on Czerny-turner design. The monochromator used in this system is *LOT QD MSH-300* [45]. It has a bandwidth of 4nm and uses reflection diffraction grating (grating groove density of 1200 l/mm). It is capable of producing monochromatic light in the range of 200 nm - 1.1 µm, with an accuracy of 0.2 nm over the entire wavelength range. The wavelength reproducibility is 0.05 nm [45].

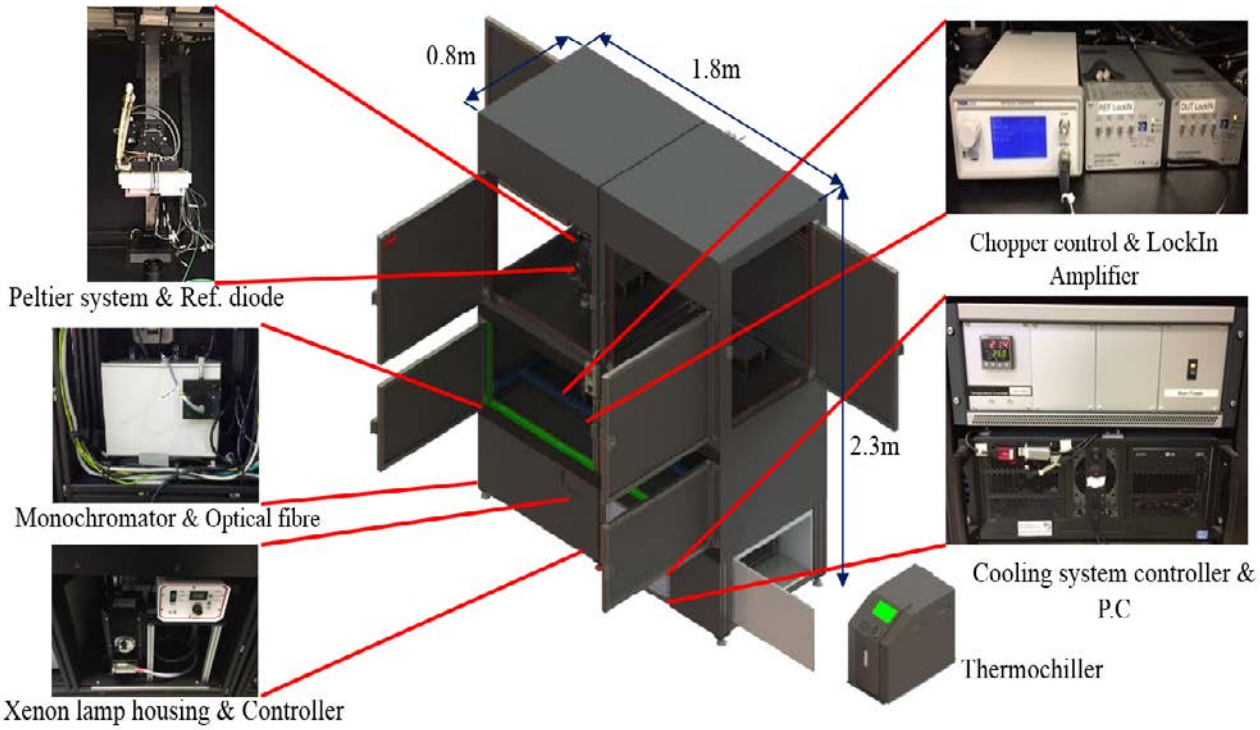

Fig. 26 A view of opto measurement system with its components.

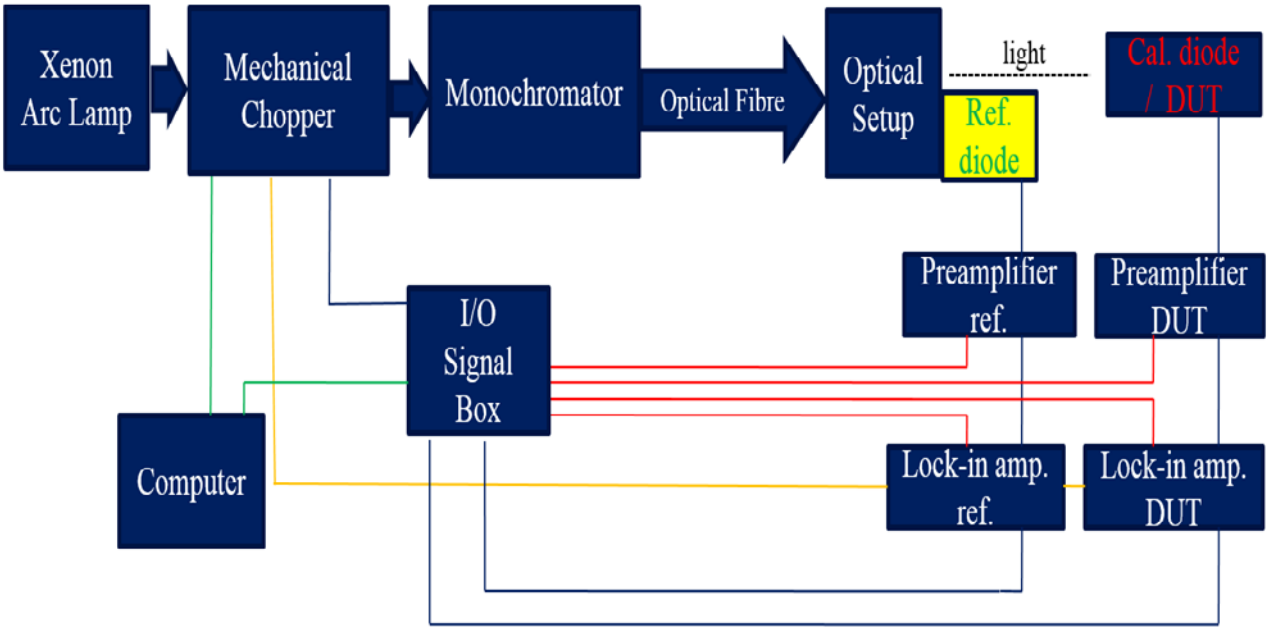

Fig. 27 Schematic of the opto measurement system, used as a monochromatic light source under dark conditions at constant temperature to evaluate the number of photon, which is illuminated to the detectors.

- **Optical setup**

  The output of the monochromator is connected with a bundle of fiber *(LOT LLB592)* [45], which is 1m long and has an output diameter of 3 mm. The light from the fiber is coupled to the optical bank through which it is finally incident on the sensors.

  Two certified and calibrated photodiodes *S1336-5BQ* used in this setup are manufactured by Hamamatsu and have a maximum dark current of 30 pA. One of the diodes is used for control and reference for the system and the other one for the calculation of impinging photon flux on the detectors. The certification indicates the uncertainty of ±4.5%, in the optical sensitivity of the photodiodes, expressed in units of AW^{-1}, which should be included in the estimation of the overall uncertainty of this test. The diodes photosensitive area is 2.4×2.4 mm^2 and has sensitivity from the UV region to near IR part of the spectra. With the help of this reference diode the impinging photon flux on the detectors is calculated from their output currents by using their wavelength specific AW^{-1} values.

- **Preamplifier and lock-in amplifier**

  The signals from the calibrated photodiode under the illumination are amplified by a variable gain low noise current amplifier (*FEMTO DLCPA-200* [47]). It allows accurate and ultra-low noise DC measurement down to femtoampere with gain variance of 10^5 and 10^7 V/A. The current signal from the preamplifier is passed to the lock-in amplifier to increase the signal to noise ratio, which works on the orthogonality of sinusoidal signals.

Lock-in amplifier, *FEMTO LIA-MVD-200-L* [47], extracts the signal from a known carrier wave from an extremely noisy environment. It multiplies the frequency of the signal from preamplifier with the reference signal frequency from the chopper and results a dc signal. Where any signal other than the reference signal frequency, is ideally attenuated to zero.

- **Cooling system**

  In order to maintain the temperature (-20ºC to 60ºC) within the system, a double stage Peltier cooling systems used in combination with a thermochiller *SMC HEC012-W2A* [48] and *idCOOL system* [44]. The *idCOOL* offers the programmable control of the temperature of the whole system. In order to avoid the condensation at low temperature, compressed air is used within the measuring box.

  The sensor is mounted on the copper plate of the first peltier system, and is cooled by the conduction of heat. The second peltier system has a connection with water circulating system and the thermochiller, which leads to fast cooling of the first peltier system.

  If normal temperature conditions are required then the use of the peltier system without the water cooling (i.e. using air) is enough, whereas for low temperature and fast cooling, peltier system in combination with the thermochiller is used.

- **Automatized positioning system**

  This measurement system offers a flexible positioning of SiPMs in x (0-1100mm), y (0-200 mm), z (0 to 40 mm) and θ ($\pm 30°$) directions. The sensor mounted on the copper plate can be placed to a desired coordinate by a motor (only in x & y directions) with a step of 50 µm. The z and θ coordinates have to be set manually.

  The measurement control for the whole system is done via a computer having *LabView* based graphic user interface, developed by the manufacturer.

3.2.2 Tile Evaluation Kit

The Tile Evaluation Kit (TEK) is provided by Philips Digital Photon Counting (PDPC) along with the digital SiPM array, as their readout system. This enables us to get a digital signal per pixel caused by a photon detection under different conditions, without any additional setup requirement. The TEK [43] comprises a base unit, a power supply unit and a laptop with preinstalled software.

Fig. 28 shows the schematic of the base unit. This base unit (Fig. 29) controls all the data communications of the PDPC. It is connected to a laptop via USB and has connection with the power supply unit. It offers communication with 4 PDPC tiles simultaneously via tile connectors. The power unit is used to provide the suitable voltage to the base unit so that sensor can be biased. The setup of the TEK can be seen from Fig. 30.

Fig. 29 Photograph of a base unit of DPC 3200-22-44[43]

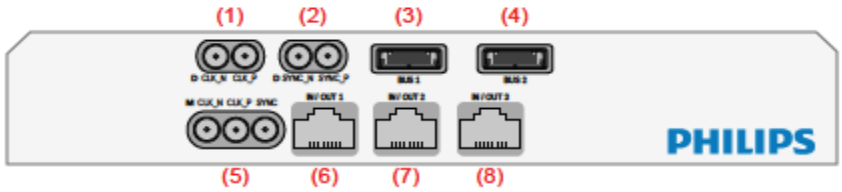

(a) Front

(b) Back

Front		Back	
(1)	LVDS clock	(9)	Fuse (2 A(T); min. 35 VDC)
(2)	LVDS SYNC	(10)	Power input
(3)	Module bus 1	(11)	USB connector
(4)	Module bus 2		
(5)	LVDS clock (FPGA processed) + SYNC		
(6...8)	General purpose I/O *(future use)*		

Fig. 28 DPC 3200-22-44 base unit schematic [43]

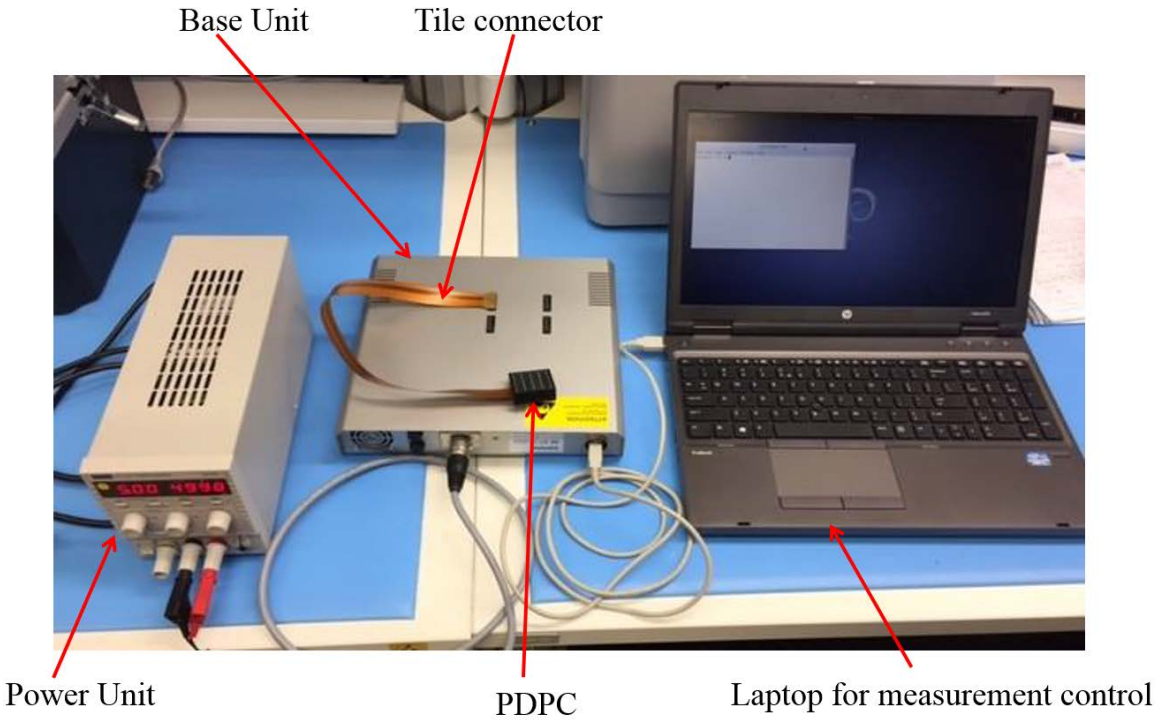

Fig. 30 TEK setup for the PDPC read out

The data acquisition from the TEK can be initiated by setting parameters (such as trigger threshold, validation interval and integration interval) of measurement. Fig. 31 depicts the event acquisition sequence along with timing parameters of the PDPC for one avalanche event initiated by a photon.

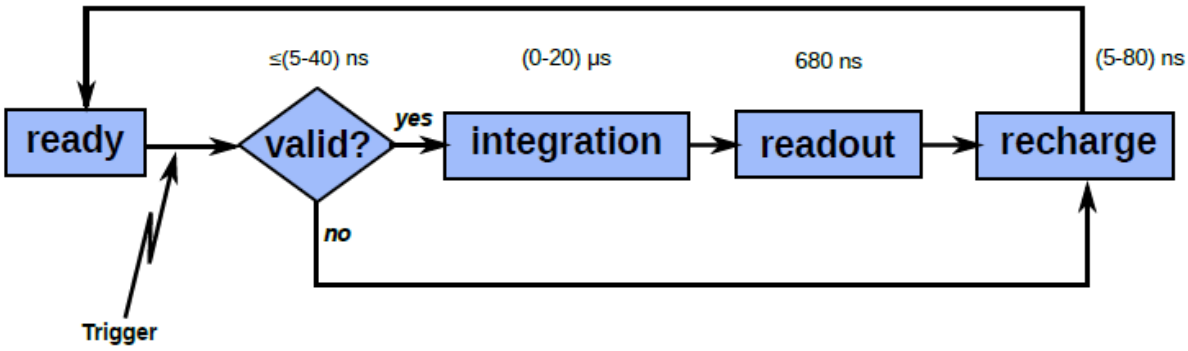

Fig. 31 Event acquisition sequence of DPC 3200-22-44 for one event [43].

The TEK offers not only a digital counting of photon events per microcell simultaneously but, also it features digital counting for each individual microcell sequentially and keeping all other microcells off. This mode of operation ceases any possibility of crosstalk between pixels.

In this experiment four pixels of die 10 have been considered for the measurement and individual reading mode of microcells is used.

3.2.3 Electronic Measurement System

Electronic measurement system is developed for readout of analog SiPM arrays. In order to find the breakdown voltages and currents, detectors are biased with a programmable power supply (*EA-PSI 6150-01*[49]), having a resolution of 10mV and dc output voltage (0-150V), and the signals from the detectors are read out via USB connections using a data acquisition system (see Fig. 32). A *Meilhaus Electronic USB RedLab TC* [50] digital thermometer is also used at the detectors surface to get precise temperature measurements. The automation of the system is realised in a *LabView* environment. The schematic of the setup is depicted in Fig. 33.

As shown in Fig. 33, instead of all the pixels (64 for the Hamamatsu or 144 for the SensL) only four pixels of SiPM arrays are utilized for this measurement so as to avoid electromechanical complexity. Each pixel is grounded with a load resistance of 1MΩ, and the signals from them via co-axial cables are fed to the *National Instruments NI 6343*[51] data acquisition system (DAQ), to read the output voltages of each pixel via this load resistance for a specific time period under different biasing conditions. The current is calculated by the software using the measured voltage and the value of the load resistor. The DAQ has 32 analog (parallel) input channels, 10ns timing resolution, input impedance of 10 GΩ in parallel with the load resistance, and a maximum sampling rate of 500 kS/s.

The detectors were reverse biased and a voltage sweep at a step of 100 mV was set until reaching the Geiger mode bias for each detector, correspondingly I-V curves were plotted through the PC unit. After this measurement, the data were extracted for the further calculations.

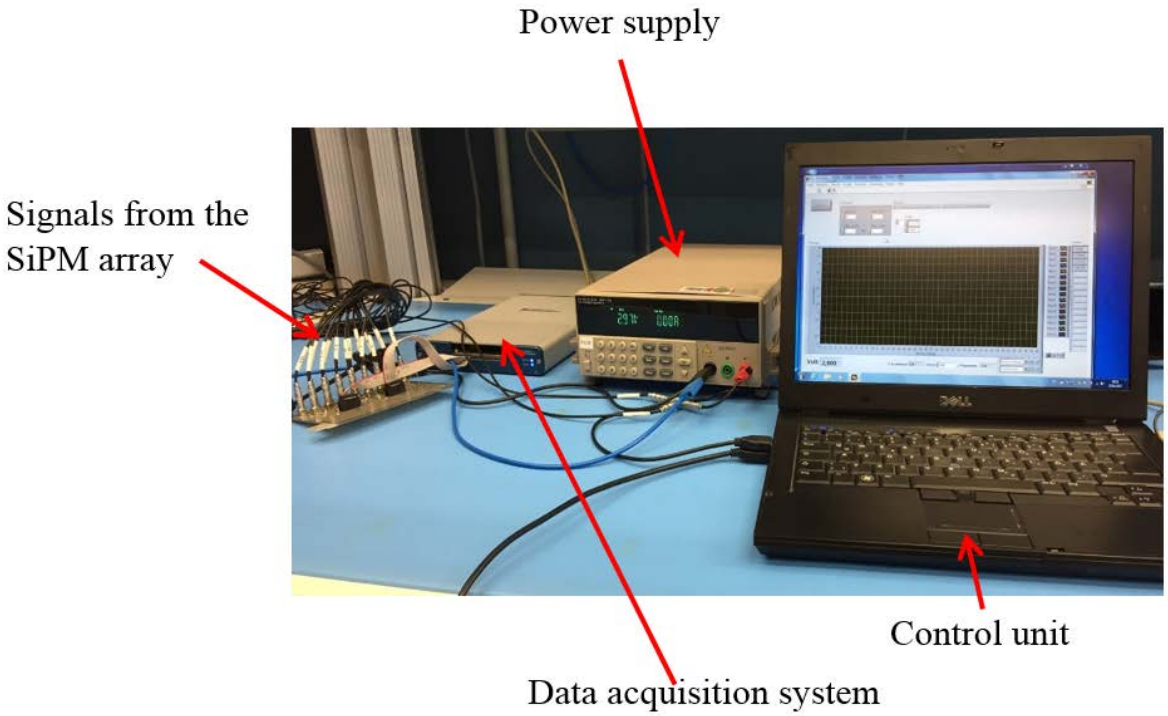

Fig. 32 Photograph of the setup of electronic measurement system for analog SiPM arrays readout

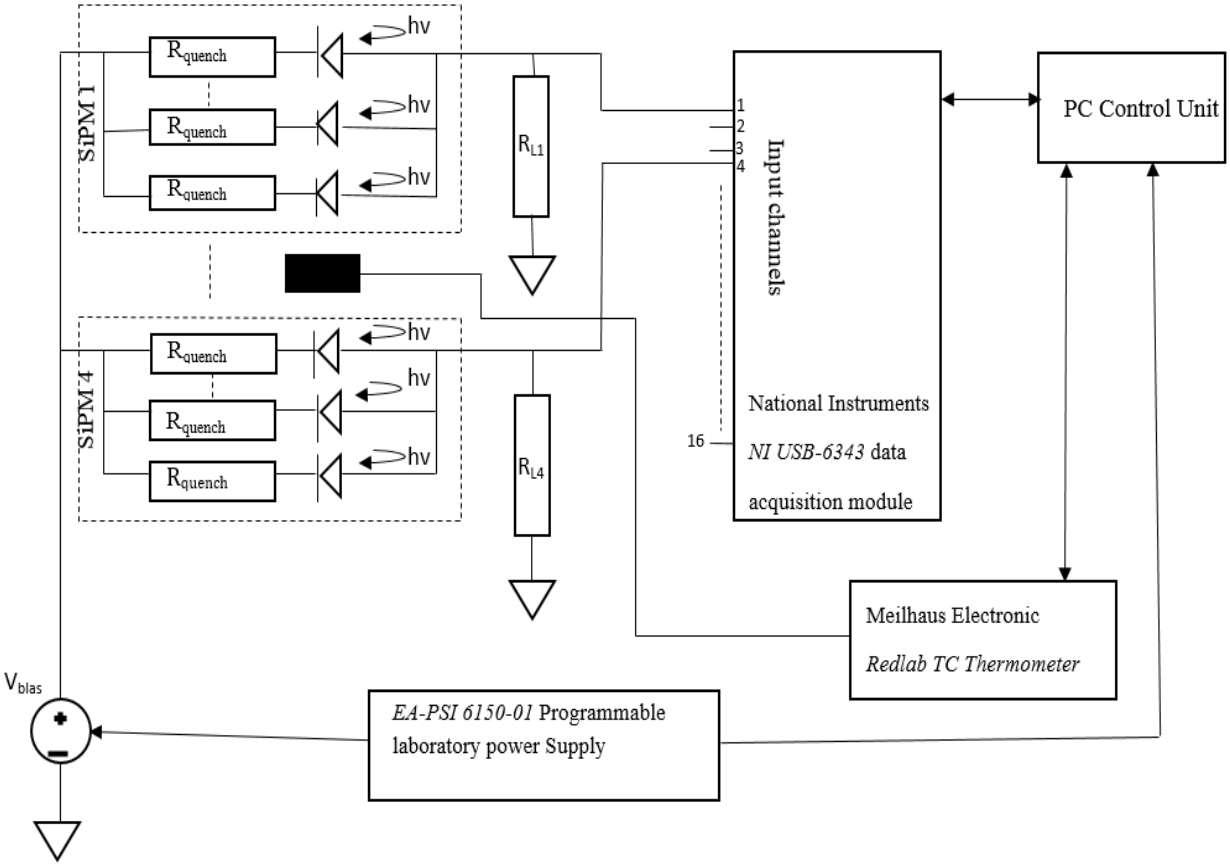

Fig. 33 Schematic of the electronic measurement system for analog SiPM arrays readout.

3.3 Measurement Method

The test concept envisaged for investigating effects of cold neutron irradiation on the SiPM arrays, focusing on photo detection efficiency, is based on their response to photons in comparison with a calibrated photodiode response, maintaining the same experimental conditions.

The basic principle undertaken for the evaluation of the PDE is to measure the number of photons of certain wavelength from the certified calibrated diode and then finding the number of photons perceived by the SiPM arrays for the same light signal.

Two different approaches, namely photocurrent and photon counting, have been adopted for evaluating the response of the detectors. Measurement of current as generated charges: photocurrent approach is utilized for the analog SiPM arrays, whereas counting the produced events: photon counting approach for the digital SiPM array. The measurement has been done primarily in two steps.

Step 1: In order to quantify the incident photons, the irradiance at different wavelength was calculated using the output current signal from the calibrated diode with known spectral sensitivity. Eq. 12 and Eq.13 describes the underwent calculation.

$$E = \frac{I_{ph,r}}{S*A} \tag{12}$$

$$I_{ph,r} = I_{tot,r} - I_{d,r} \tag{13}$$

Where E = irradiance (Wm^{-2})
$I_{ph,\,r}$ = photo current of reference diode (A)
S = spectral sensitivity of reference diode (AW^{-1})
A = area (m^2)
$I_{tot,\,r}$ = total current of reference diode (A)
$I_{d,\,r}$ = dark current of reference diode (A)

Then, dividing the irradiance by the energy of photons to calculate the number of photons, as shown in Eq. 14 and Eq.15.

$$Ph_i = \frac{E * t_{int} * A}{E_{ph}} \tag{14}$$

$$E_{ph} = \frac{h * c}{\lambda} \tag{15}$$

Where Ph_i = number of impinging photons
t_{int} = integration time (s)
A = area (m^2)
E_{ph} = energy of photon (J)
h = Planck´s constant (J.s)
c = speed of light (ms^{-1})
λ = wavelength of light (m)

Step 2: Evaluating the PDE by dividing the Ph_i by the photons detected by sensor (Ph_d) (Eq. 16).

$$PDE = \frac{Ph_d}{Ph_i} \tag{16}$$

- Ph_d for the analog SiPM arrays is calculated as the ratio of the sum of the charges (or produced photoelectron) to the gain of the SiPM (Eq.17):

$$Ph_d = \frac{I_{ph,s} * t_{int}}{e * G} \tag{17}$$

$$I_{ph,s} = I_{tot,s} - I_{d,s} \tag{18}$$

Where $I_{ph,\,s}$ = photo current of SiPM (A)
t_{int} = integration time (s)
e = elementary charge(C)
G = gain of SiPM
$I_{tot,s}$ = total current of SiPM (A)
$I_{d,s}$ = dark current of SiPM (A)

- Ph_d for the digital SiPM array is the output signal counted by the TEK.

3.4 Measurement Procedure

The measuring procedure is mainly categorised as integration and characterisation of the opto measurement system, carrying out premeasurement check and, finally, the determination of the breakdown voltage for the analog SiPM arrays.

3.4.1 Integration and Characterisation

The first task, in order to evaluate the PDE, was to integrate the opto measurement system. After the integration, the system was characterized. For finding the irradiation for the 300-1100 nm range, several measurements were performed so as to estimate the cumulative uncertainty of the lamp, positioning system, and the data reproducibility of the system. In each measurement, the experimental conditions were held constant and the lamp was used only after stabilisation, i.e. after 30 to 45 minutes of waiting period before the measurement started. In the Fig. 34, the variation in the irradiation measurement by the system is shown over few measurements. This process was repeated twenty times (each output having an average value of 5 measurements) to find the systematic deviation, which was observed as 10.21 % for the entire investigation period.

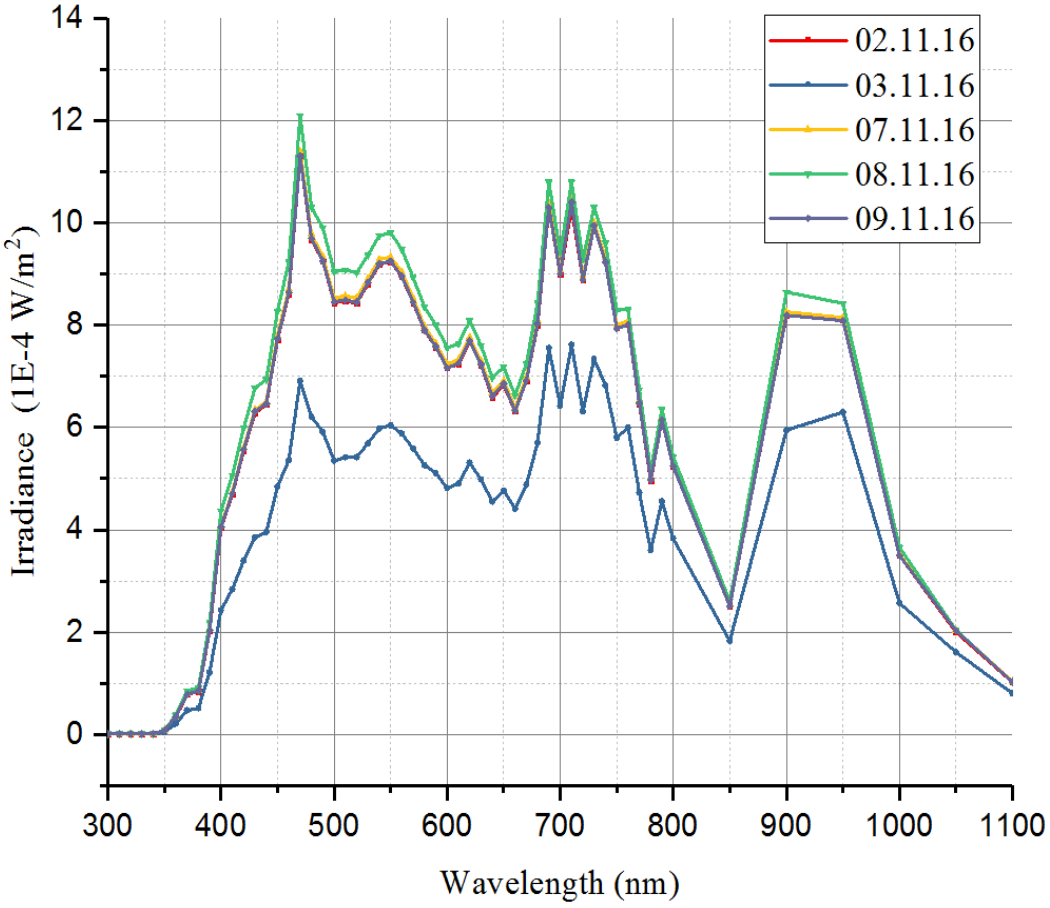

Fig. 34 Graph showing the irradiation (using absorptive neutral density filters of optical density 1) variation over time for few measurements.

It was important to illuminate the sensors with a light spot having uniform distribution. As we decided to illuminate four pixels of a SiPM, we needed at least 8×8 mm^2 spot area, i.e. the maximum value of the area of 4 pixels of three choosen SiPM array. Fig. 36 depicts the schematic of the four pixels of PDPC module. The spot diameter available to us was either of 25 mm or 1 mm diameter. Hence, we characterized the full spot area of 25 mm and pointed out the area of 8×8 mm^2 with maximum uniformity in light distribution. Fig. 35 shows the scanning of the complete spot area (at a step of 1mm) with the reference photodiode (or so called calibrated diode). Fig. 37 depicts the selected spot area profile based on the light distribution profile.

The maximum uniformity achieved had a standard deviation of 1.42 % within the area of 8×8 mm^2. We selected this spot area as our illumination area for the SiPMs, and positioned the four pixels of SiPM within this illumination area.

After the selection of the best homogenous spot area, we illuminated the PDPC first and tried to measure the desired parameters, but we found that the light intensity was too much and the PDPC was saturated (explained in next section). Hence, we had to reduce the light intensity impinging on the PDPC. We did this through the inbuilt system parts, i.e. with absorptive neutral density filters provided by *Thorlabs*.

The problem for the use of absorptive filters was that, the measurement system was assembled to offer reduced light intensity but only with 1mm diameter pinhole illumination area (Fig. 39).

This was not enough for us, as we needed minimum illumination area of 8×8 mm^2. Therefore, we had reassembled the optical setup in order to get the desired illumination area with less intensity of light. This was done by taking out the absorptive filters combined with the pinhole from the optical setup and getting rid of any other optical hindrance placed between the light illumination source and the device under test (DUT), i.e. SiPMs (see Fig. 38).

With the reassembled optical setup, we got the freedom to use the full spot area of illumination with the absorptive filters, i.e. the desired light intensity in combination with the required area. Characterisation of the new optical setup has also performed and the homogenous spot area of illumination (8×8 mm^2) has been determined again. The deviation in the light distribution within the selected area remains almost the same. In this way, we adapted our system to the light intensity and the area requirements.

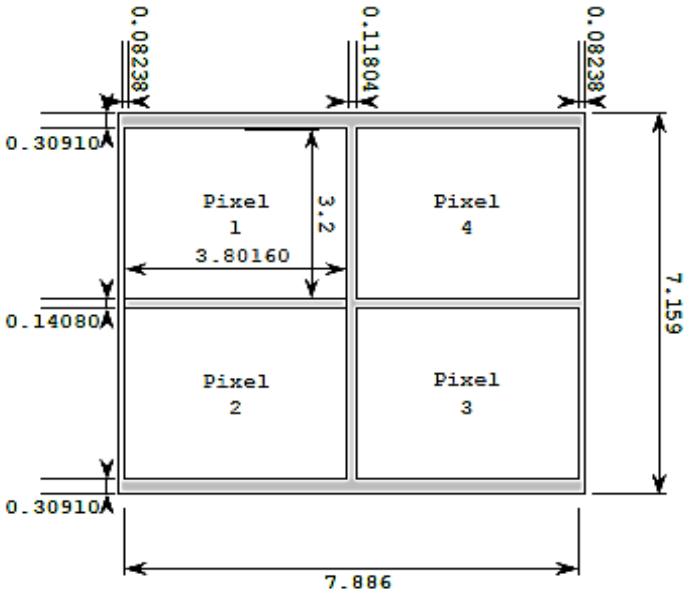

Fig. 36 DPC3200-22-44 die dimension in mm[43]

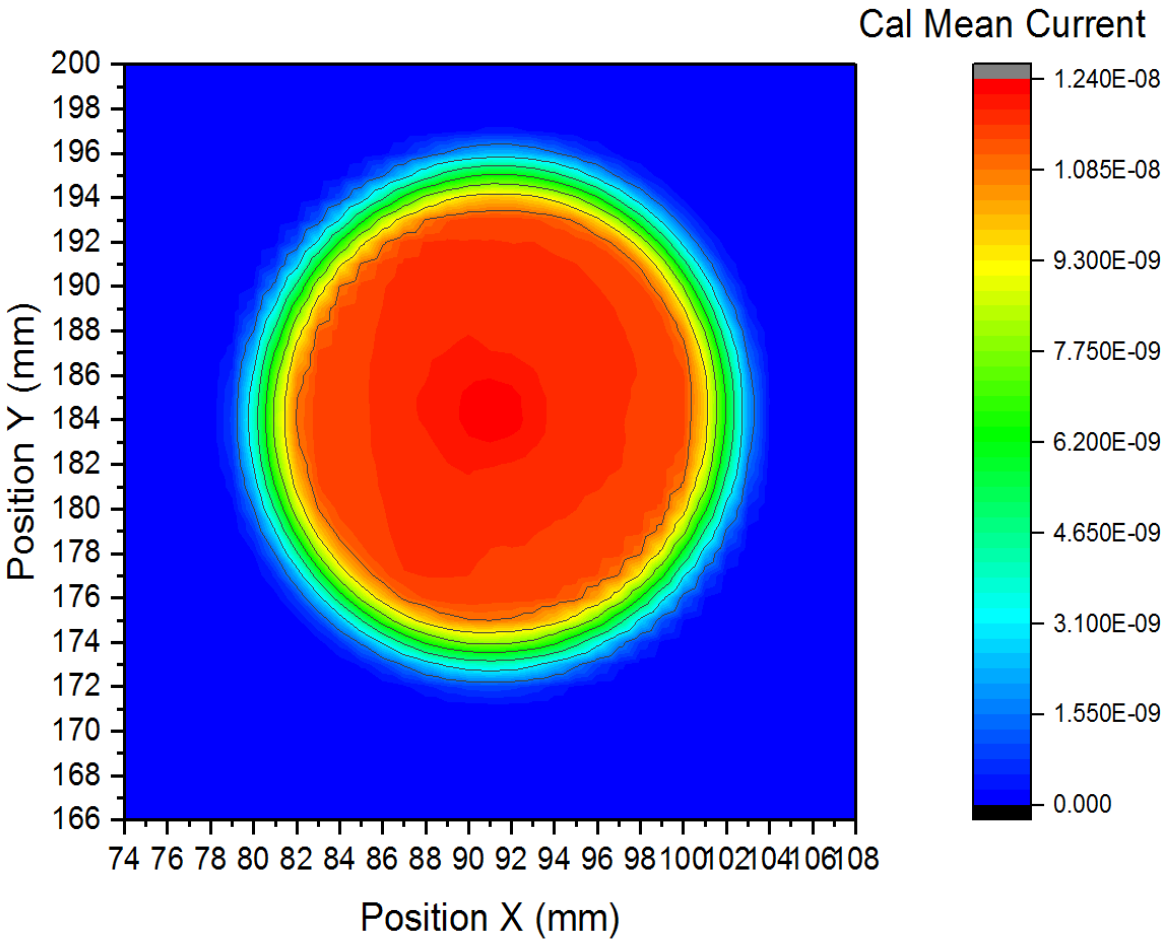

Fig. 35 Picture showing the scanning (light distribution profile) of complete spot area (25mm) with the full intensity of light at a step of 1mm by the calibrated diode.

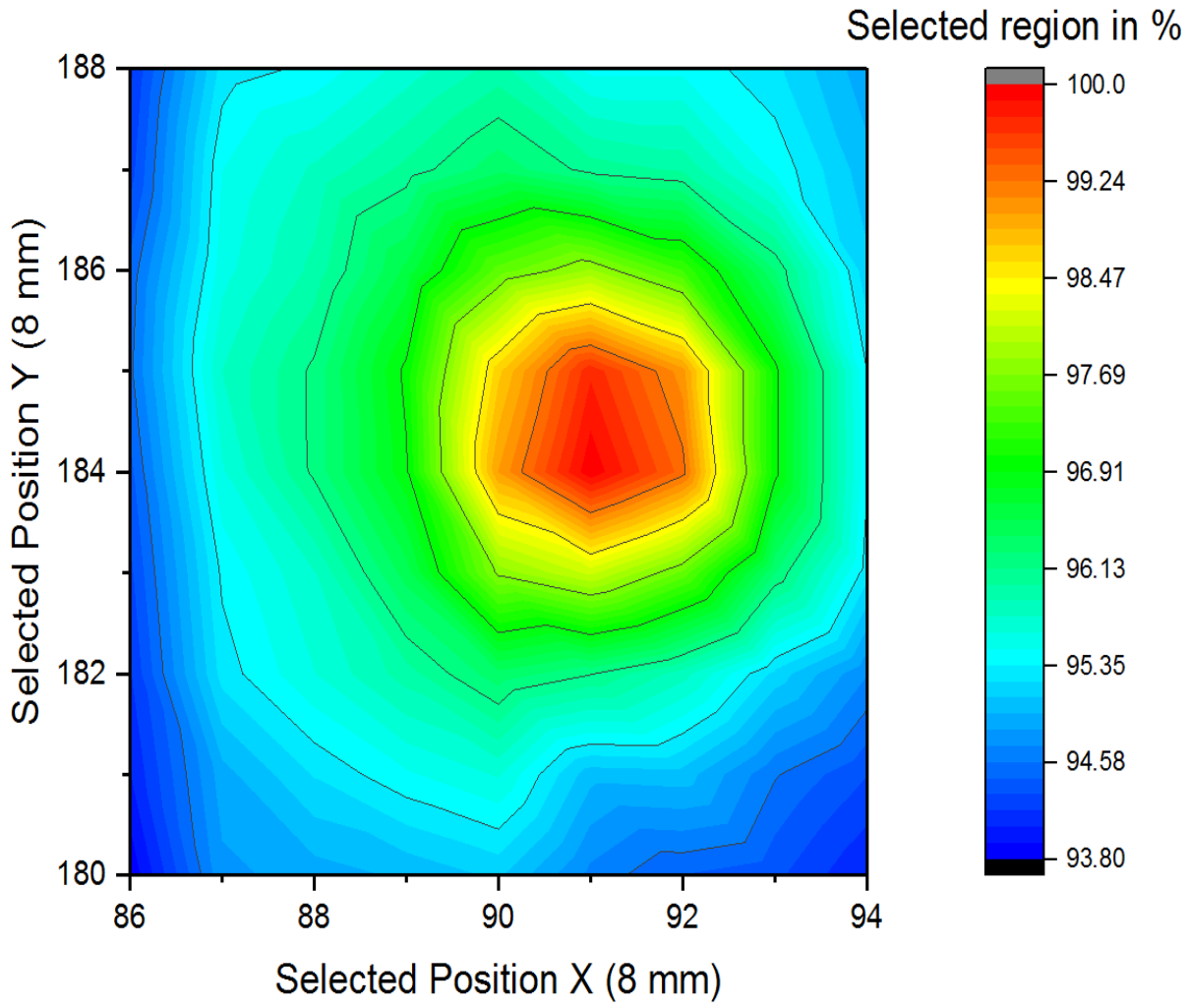

Fig. 37 Picture showing selected spot area (8×8mm) scan (light distribution profile) with the full intensity of light at a step of 1mm by the calibrated diode

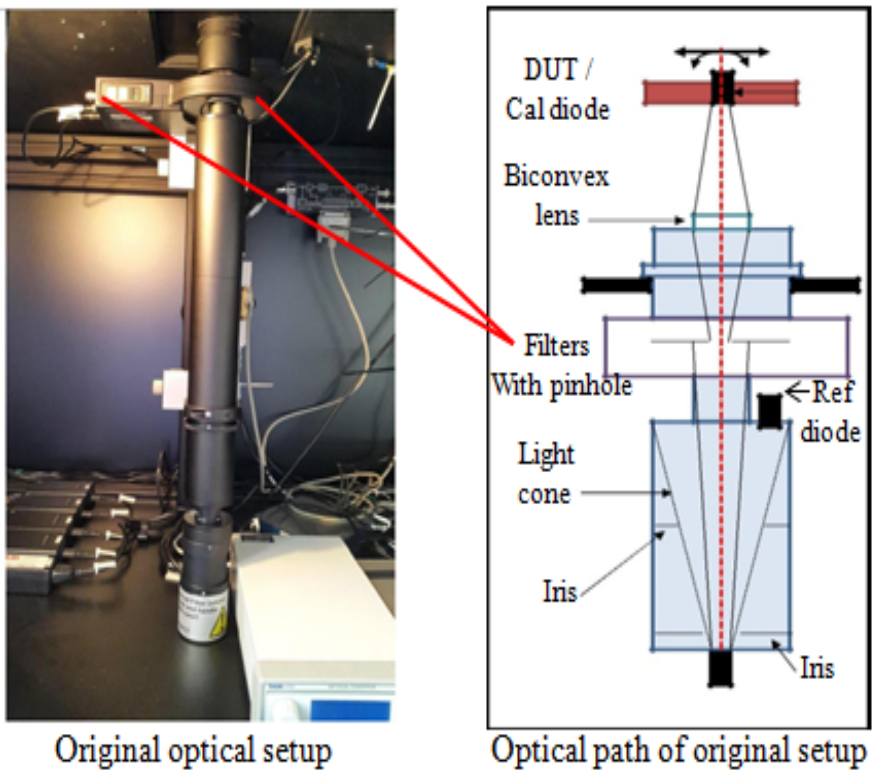

Fig. 39 Picture showing the inbuilt optical setup (filters and pinholes combined) and the optical path of the setup

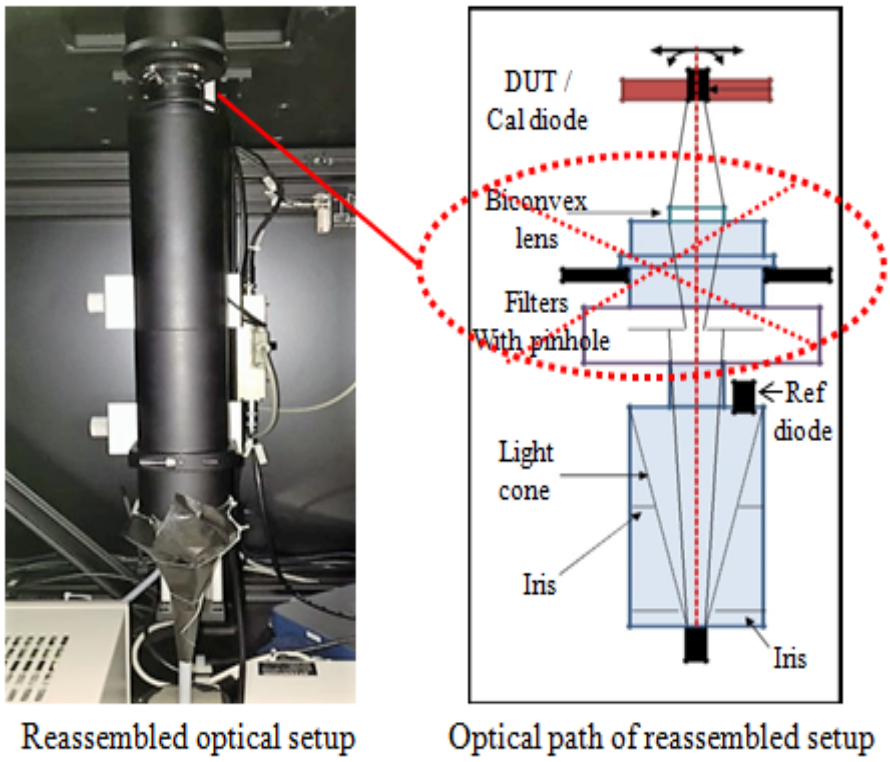

Fig. 38 Picture showing the reassembled optical setup (without filters, pinholes and lens) and the optical path of the reassembled setup.

3.4.2 Pre Measurements

Although, SiPM provides output proportional to the light flux, its linearity is limited. The finite total number of microcells in the SiPMs and the quenching time of each photoactive cell, limits the optical range over which the detector provides a linear output. This means that for each microcell, the average number of impinging photons should be low or else the photons will not be detected by the SiPM. If the number of incident photons is higher than the number of fired cells then it will not detect all the photons and it will get into saturation, i.e. for a high intensity of light it will give the constant output. For avoidance of this effect, low light intensity should be used. This characteristic represents the dynamic range of the SiPM, and can be evaluated as shown in Eq. 19 [21].

$$N_{fired} = M\left(1 - e^{-\frac{PDE * N_{ph}}{M}}\right) \tag{19}$$

Where N_{fired} = number of fired cells.
N_{ph} = number of incident photons
M = number of cells in the SiPM
PDE = photon detection efficiency

The saturation of SiPM can take place also due to its deadtime. If the light is impinging the detector over a defined integration time shorter than the dead time of the microcell, then also it will not be able to provide the proportional information because the cell will be recovering in that time, and is not ready for another avalanche event. Therefore, a suitable time period for illumination should be chosen.

Hence, it is advised to characterise the saturation range for the SiPM and find a suitable light intensity to be used before measurements of the PDE, else one can easily underestimate or evaluate a false PDE of the SiPM. This is also done in this test and we found the range of photons to be illuminated with for the SiPM. A rule of thumb will be maximum ~10^7-10^8 photons/s/mm^2 is suitable. Nevertheless, the unexpected early saturation of the analog SiPM arrays violates this maximum range and we were struggling to understand this phenomenon which will be further studied but not in the frame of this work. An example of a linearity check to find the saturation range of a PDPC is shown in Fig. 40.

After the determination of the saturation region, we came to a conclusion that the direct light intensity was too much for the PDPC. The quick solution for reducing the light intensity, was to put a paper at the end of the light output window. We found the PDE curve also but, later came to realize that it was not a good scientific practice and then we used the absorptive filters to come up with satisfactory results. The results and explanation for this test can be found in the next chapter.

The saturation started too early (~10^6 photons/s/mm^2) in the case of analog arrays, which was much lower than the theoretical value. Hence, we had to use the absorptive filters of optical density (O.D) 4 to reduce the light intensity, which was beyond the sensing capability (till O.D 3) of the reference diode.

Therefore, for the irradiance calculation, we considered the optical effects in the irradiance with the filter having O.D 1 and then interpolated the irradiance for the filter having O.D 3 by the factor multiplying the transfer function of the filter of O.D 1.

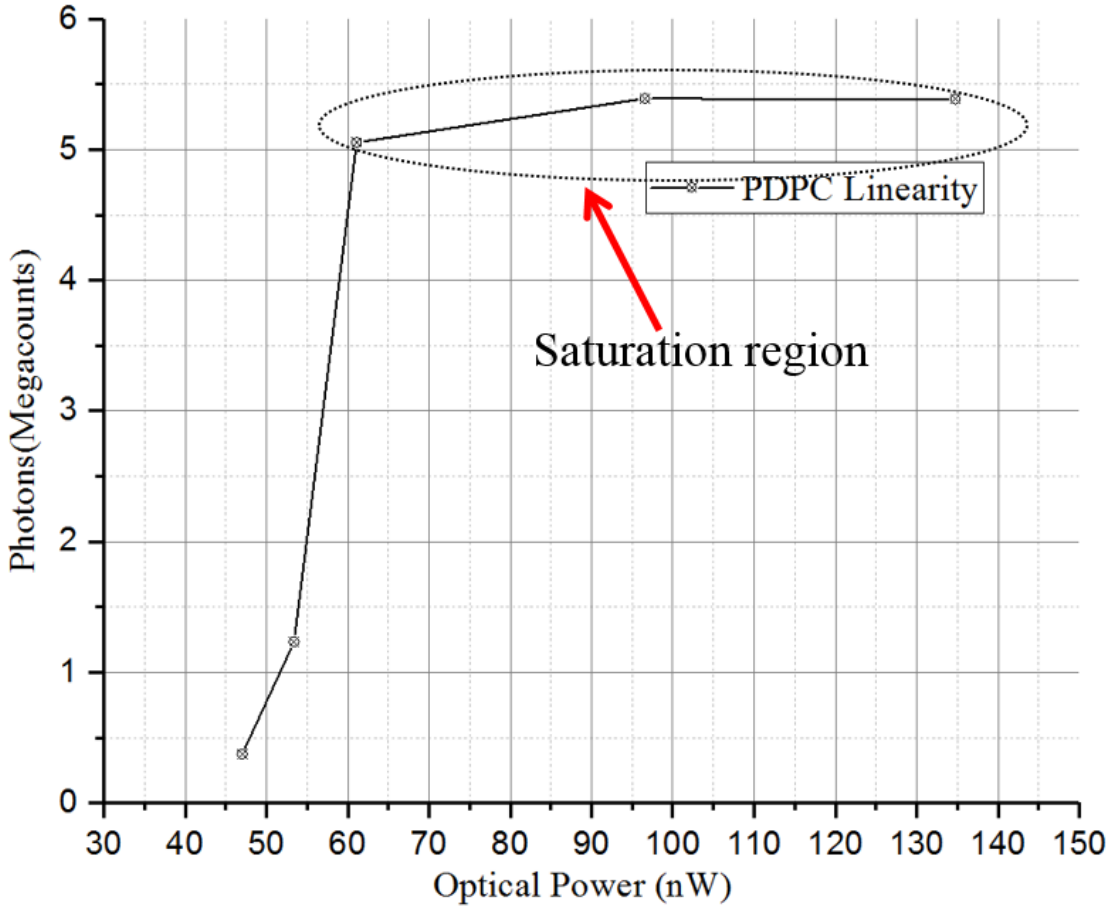

Fig. 40 Graph showing response of PDPC under different light intensity to find the suitable light intensity by observing the nonlinear range and staying below this limit to avoid saturation of the sensor.

3.4.3 Determination of the breakdown voltage

For reading out analog SiPM arrays using the electronic measurement system, determination of breakdown voltage was necessary. Determination of breakdown voltage can be done either by dynamic-type measurement (G-V curve method) or static-type measurement (I-V curve method). We tried to follow the first method in the beginning but, were unsuccessful due to lack of detailed knowledge, limited equipment for the arrays and high noise.

Later on we concentrated on relatively easy method: I-V curve method. This apprehension of ease, faded soon after, as we did not find any concrete way to determine the precise value of the breakdown voltage of the SiPM arrays. It was important to find out the exact breakdown voltage and then locate Geiger mode bias voltage (recommended overvoltage of 2.5V for SensL and 2.6V for Hamamatsu) to determine the photocurrent. It was very difficult to point out the breakdown voltage from the simple I-V curve. Several methods and their differences can be found in [32][33][52]. We came up with three different approaches, all of them are based on the concept of inverse logarithmic derivative method (ILD)[53], and explained below:

- Maximum of $(d\ln(I)/dV)^{-1}$
- Maximal of $(dI/dV)/I$
- Minima of $(d\ln(abs(I))/dV)^{-1}$

Since in the dark condition, total current of SiPM is contributed by dark counts, crosstalk, and afterpulse all of these showing an approximate linear dependency with the breakdown voltage and the gain of the SiPM, the SiPM output current can be approximated by Eq.20 [54].

$$I = \alpha(V_{bias} - V_{BD})^n \tag{20}$$

Here α and n are constant, which determines the shape of the I-V curve, V_{bias} and V_{BD} are the bias and the breakdown voltage respectively. Therefore, inverse logarithmic derivative of this current is expressed by Eq. 21:

$$\left[\frac{d\ln(I)}{dv}\right]^{-1} = \frac{(V - V_{BD})}{n} \tag{21}$$

Equating this term to zero gives the value of the breakdown voltage, and can be determined as the maximal change from the original tendency of the curve.

Although, all of the three approaches are almost same, but each yields a discrepancy of ~ ± 0.2V with respect to the other ones. The I-V curves have been analysed to find the best suited approach for this study. A picture showing the comparative behaviour of these approaches can be found in Fig. 42. After the analysis of these curves we decided to use the (dI/dV)/I approach (pink curve in the Fig. 42) to determine the breakdown voltage, due to the fact that the value obtained by this approach was closer to the value claimed by the manufacturer.

After the approach selection, we had illuminated the detectors with the desired spectral range and tried to find the breakdown voltage for individual wavelengths. Nevertheless, sometimes it was not clearly distinguishable to find the peak (see Fig. 41) from this approach for breakdown mark, so repetitive measurements and approximations were considered. The total samples for each individual measurement were set to be 128 at a sampling rate of 1kHz in a preconfigured *LabVIEW* program, leading to an individual current measurement time (t_{int}) of 128 ms for every bias voltage step. This was sufficiently enough to get a better measurement, compared to the dead time (in ns) of SiPM arrays.

After obtaining the breakdown voltage for the entire spectral range, we could not find the uniformity in the pixel breakdown voltages (see Fig. 43). Hence, we considered the average value of all the pixels breakdown voltages for the entire spectrum for the sake of calculation ease. This non uniformity in pixels (manufacturer claimed a uniform response among the pixels) can be assumed due to measurement errors, but still this huge deviation cannot be justified by this logic. The non-uniformity across different SiPM detectors could be documented in this way.

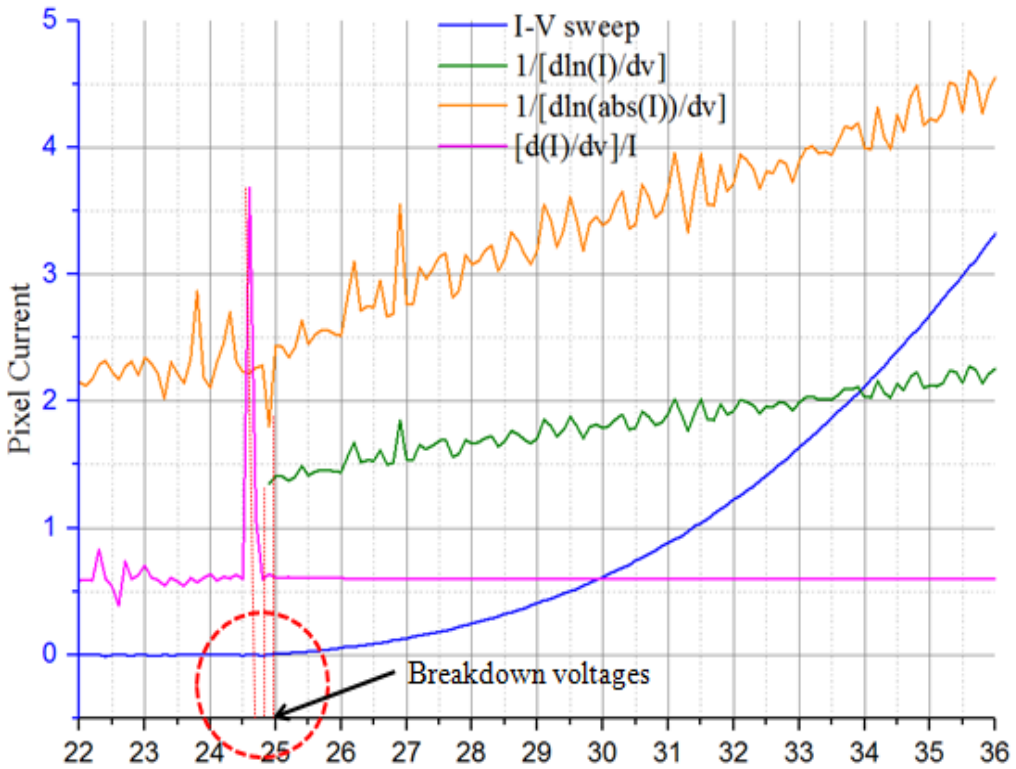

Fig. 42 Breakdown voltage determination by different approaches (shown e.g. curve is for the SensL array).

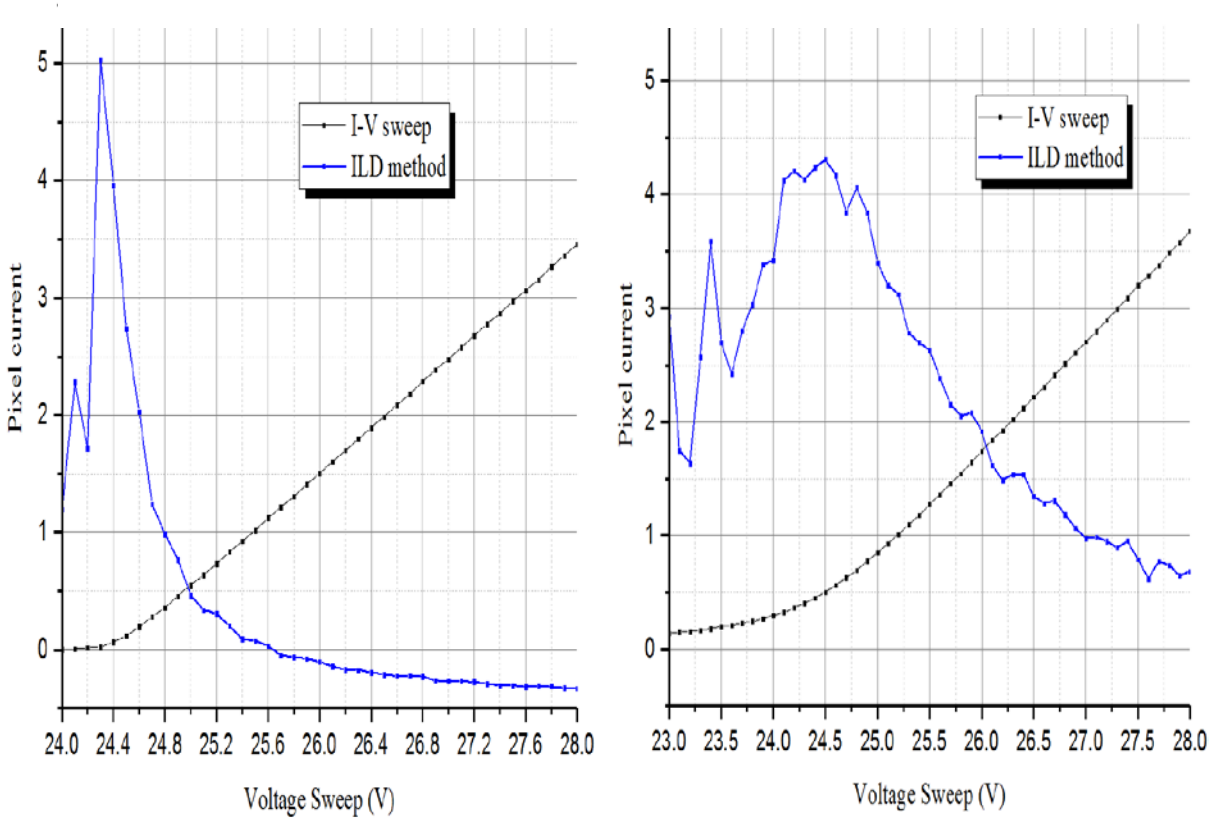

Fig. 41 Curves comparing difficulty in pointing out the peak i.e. breakdown voltage of the detectors (shown eg. curve is for the SensL array)

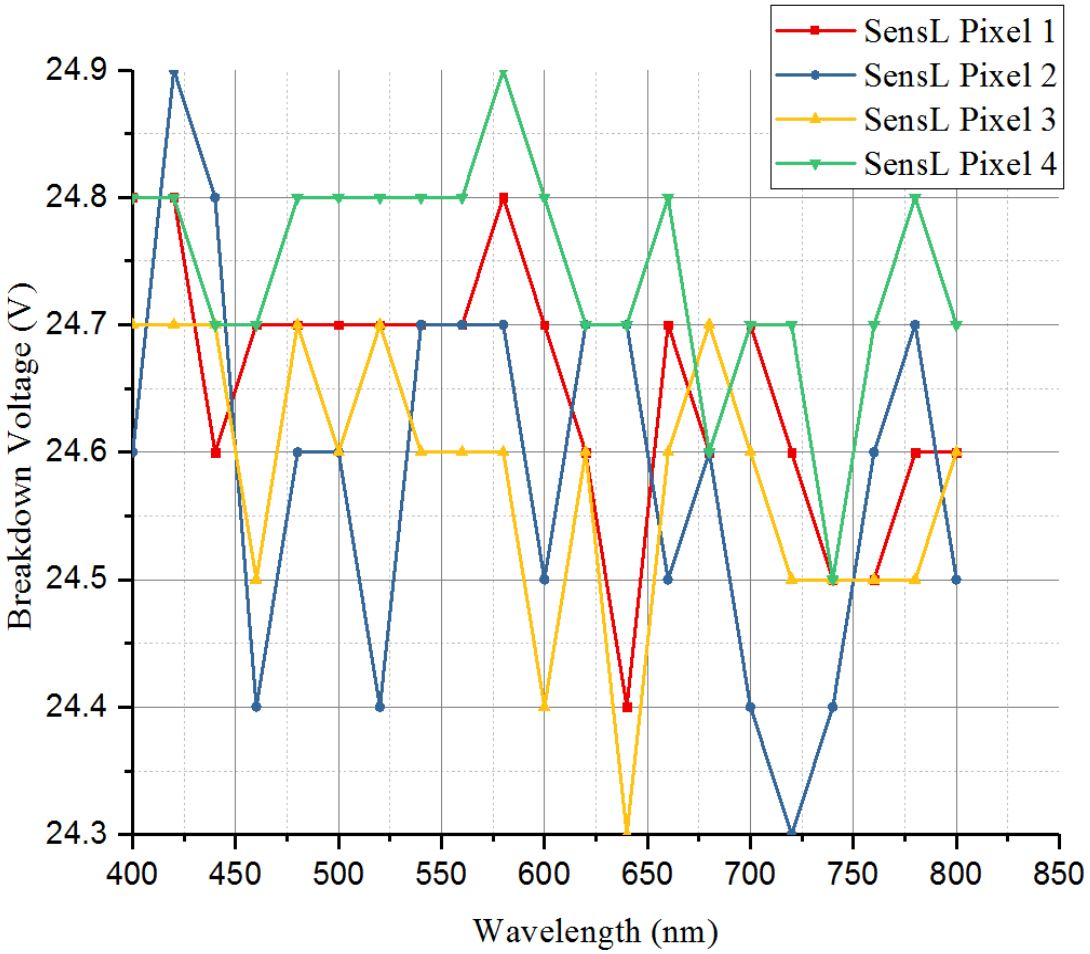

Fig. 43 Variation in breakdown voltage among the pixels of the SiPM array (shown eg. curve is for the SensL non-irradiated array) for the different wavelengths of light.

It should be noted that we did not find the absolute value of the breakdown (up to two orders in mV) and had observed that the slight deviation of 100 mV resulted in big difference to our results. Hence, the PDE curves should be perceived as the relative comparison of irradiated and non-irradiated SiPM arrays, not as the absolute PDE.

This process was performed for all the four arrays (irradiated and non-irradiated array of both SensL and Hamamatsu) and then the current was calculated to evaluate the PDE. The measurement uncertainty obtained for the electronic measurement system was 6.03%.

IV. Results and Discussion

As per the explained method and procedure, all the data were extracted from the three different measuring systems and were analysed in a scientific graphing and data analysing program "Origin" produced by the *OriginLab Corporation*. The results are divided accordingly into digital and analog array for the better understanding.

4.1 Results obtained for digital SiPM array

The first PDE curve obtained was for the non-irradiated PDPC tile, using the relations expressed by the Eq. 16, utilizing the opto measuring system and the TEK. The spectral range chosen was between 300 nm to 1100 nm with a step of 10 nm in the relevant zone i.e. in the range of 300 nm to 800 nm, and a step of 50 nm for the remaining zone. We had utilized the single cell counting mode, keeping the other cells off, to avoid any crosstalk. The measurements were performed in darkness and under illumination using the dark count mapping (DCM). Finally, the results obtained in darkness were subtracted from those obtained under illumination using Eq.12-15. This was achieved using a single command given to the TEK and getting the results for all the pixels of the sensor after few minutes. The data were further sorted out by a *MATLAB* program so that we can get the values for four pixel of die 10 (located near the center of tile) only, which was the die of choice for our experiment.

In this mode, the data acquisition time taken by the TEK for every single wavelength and each individual cell was on an average ~2 frames (1 frame= 327µs), i.e. integration time of approximately 710µs for single cell, ~2.2s (138 frames) for one entire pixel (3200 cell) and in total ~140s for the complete tile (64 pixel).

As already explained the light illumination at the full intensity was too high for the PDPC, and it was saturating, in order to reduce the intensity we used paper as absorber of light and evaluated the PDE (see Fig. 44). We obtained the measurement uncertainty standard deviation also for the PDE curves and found it was 16.6 % in total.

From the PDE curves obtained using paper, we observed a strange behaviour (higher PDE by a factor of 3 approximately) in the UV part of the spectra, i.e. between 300nm to 400nm. Later on, after some analysis, we came to know that the bleaching agent used in paper, leads to fluorescence.

This means that paper was not acting as neutral density filter, i.e. other effects were also taking place in combination with transmission of light in the UV part. The paper was absorbing the UV region light and emitting the light in blue region (420 nm – 470 nm).

This explained the irregularity in the curve as the light impinging on the senor was in fact the blue region light instead of the UV spectra. The PDE in the remaining spectra of wavelengths was also not being considered free of error, hence we discarded this entire PDE curve.

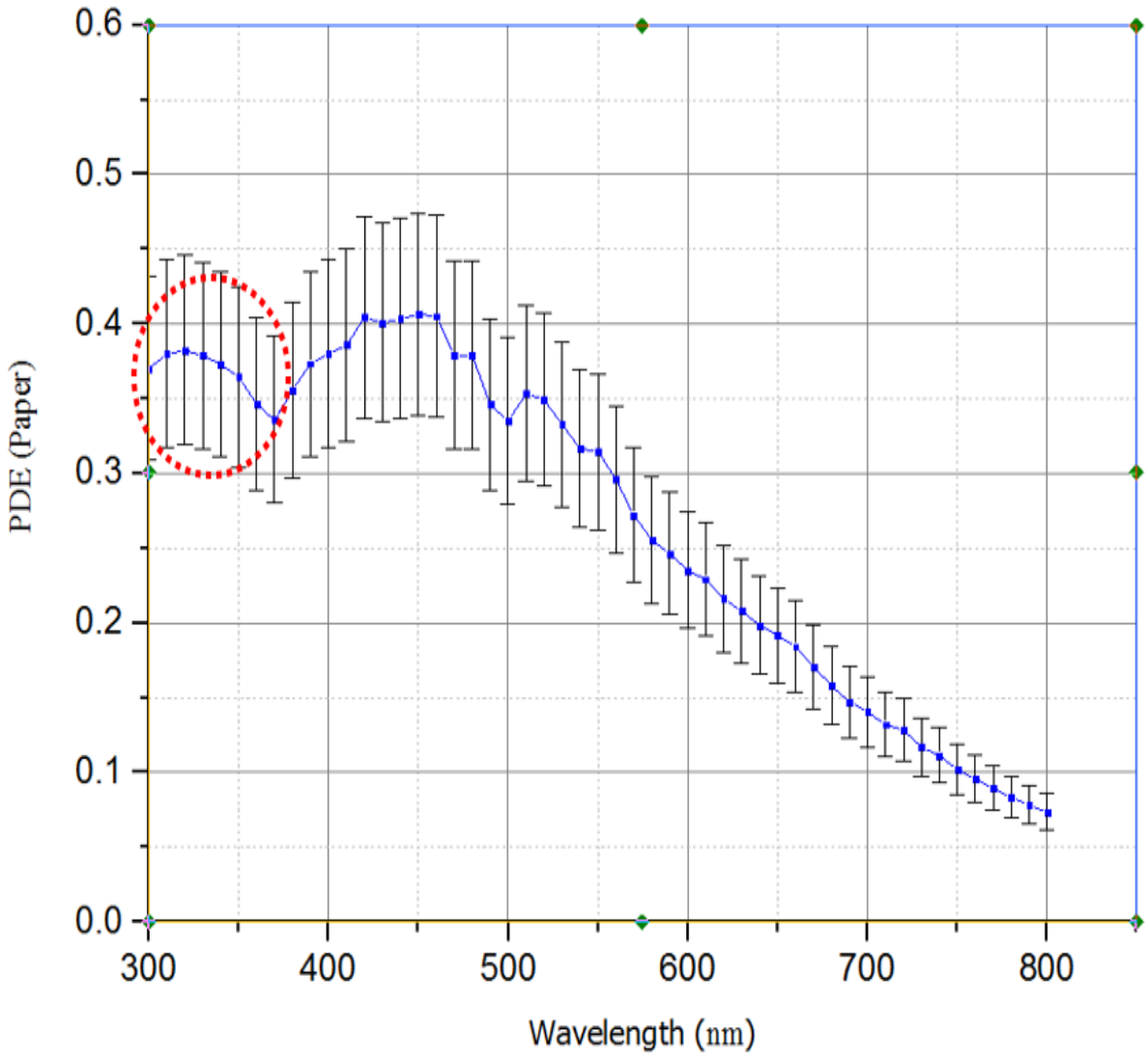

Fig. 44 PDE curve for Non-irradiated PDPC (die 10) with the use of paper as a light intensity reducer.

Later on, we used the absorptive neutral density filter to get rid of the saturation problem by decreasing light intensity and did another measurement to plot the PDE curve again. But this time we faced another problem. As the filter has the ability to response only after 350 nm, below 360 nm it was not transmitting light, i.e. it was blocking the light completely. This leads to darkness for the sensor and hence, in this part of the curve (300 nm-360 nm), we observed only noise. It can be observed in Fig. 45 that the uncertainty bar for this region is quasi infinite. The remaining part of the spectra shown satisfactory results and was comparable with the manufacturer data sheet [43].

We managed to get an acceptable PDE curve for the range between 370 nm and 1100 nm, but were still lacking the data for the part of the spectra below 370 nm.

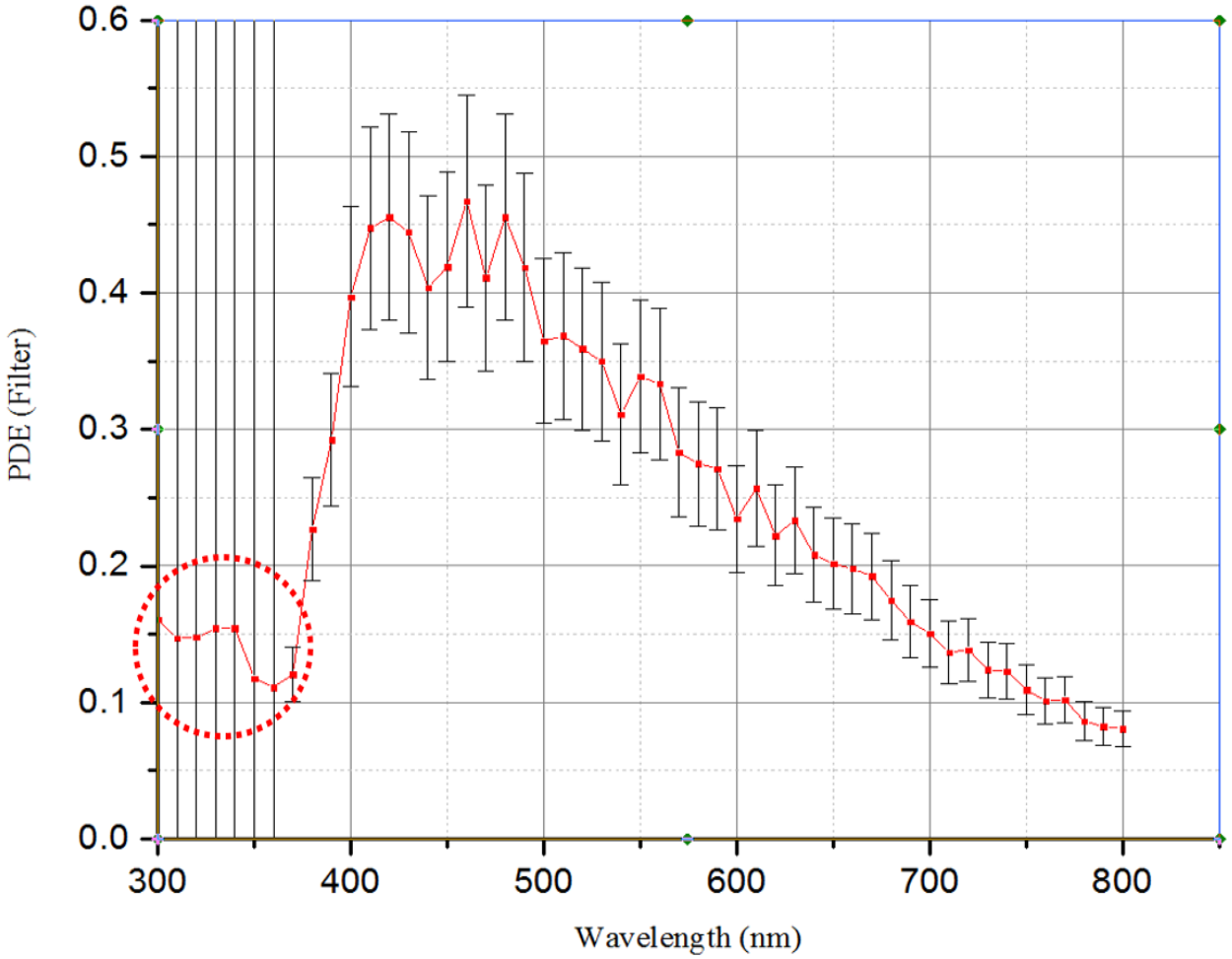

Fig. 45 PDE curve of PDPC (die 10).with the use of filter having O.D 1, showing errors in the range 300 nm -360 nm, due to the limitation of the filter.

We tried to evaluate the PDE in the full intensity again, but this time using the principle of divergence of light. This means that as the distance between the illumination source and the sensor increases, the light intensity impinging on the sensor decreases (inverse square law). The distance was increased further to a value where the sensor behaved linearly up to a certain extent, without going into saturation. Fig. 46 depicts the PDE curve of the PDPC under this condition.

After doing a detailed analysis of PDE shown in the Fig. 46, we came to a conclusion that till 360 nm this PDE curve shows linearity but above 360 nm it is nonlinear, and the PDE was underestimated due to the saturation of the sensor. The reason behind this was that the photons detected by the sensor due to longer wavelengths were deviating from the expected value.

In this way, we got the three PDE curves, under different conditions and after investigating each of them (refer to Fig. 47 for the comparison), we got the solution to evaluate the PDE for the entire wavelength range of the spectra. The chosen approach was to use the PDE data from the PDE full intensity curve for the range between 300 nm and 360 nm and to use the PDE filter curve for the range between 360 nm and 1100 nm. A corollary to this, we found the ideal light conditions to be used for illuminating the sensor and the other measurement parameter to find the corrected PDE in the desired range of the spectra.

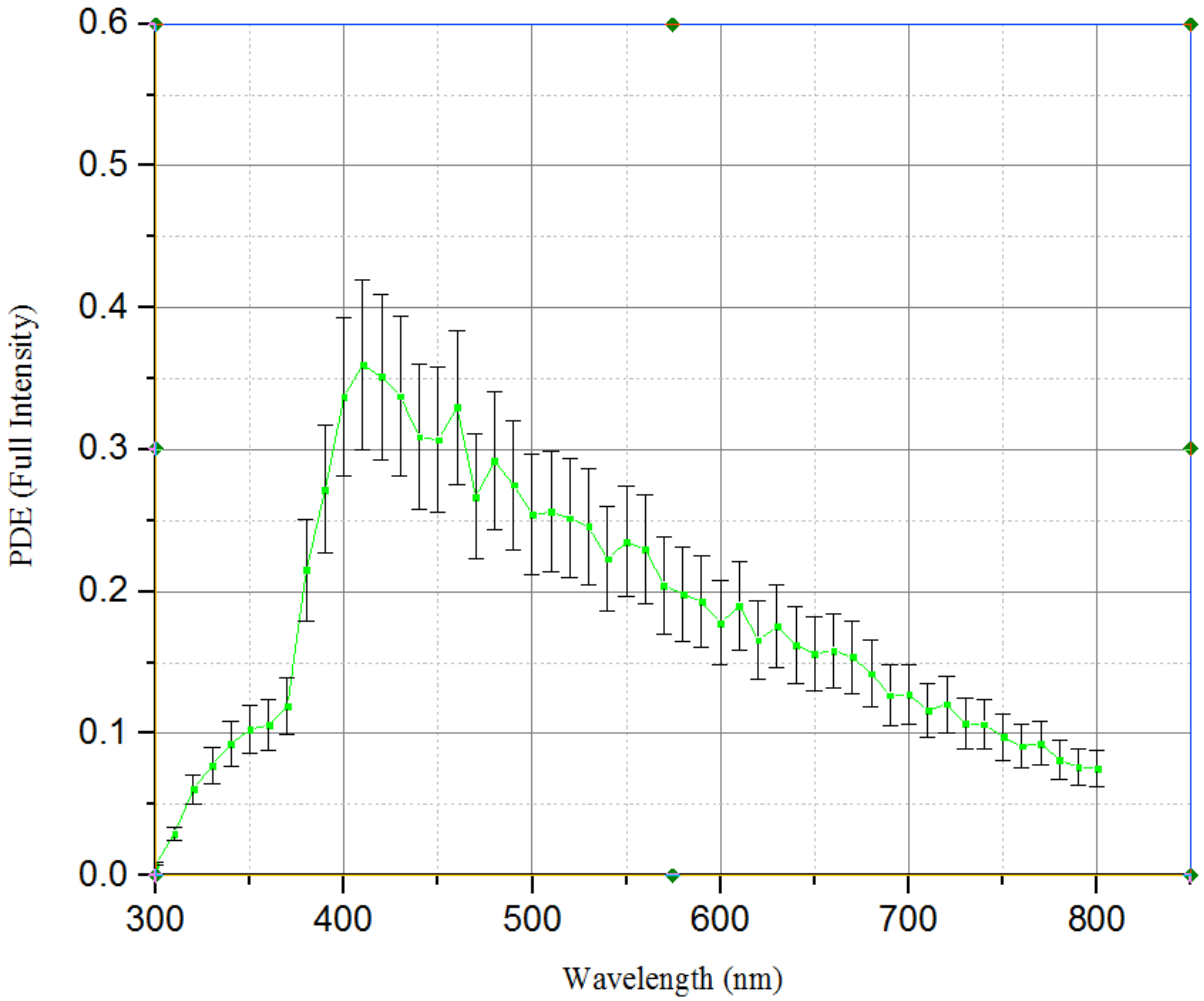

Fig. 46 PDE curve of the PDPC (die 10) under full intensity of light but with the use of light divergence principal in order to avoid saturation up to a certain extent.

Once we got the final approach for the measurement and plotted the PDE curve for the non-irradiated PDPC tile, we maintained the same experimental conditions to measure the irradiated PDPC tile and compared the both curves to quantify the effect of neutron radiation. The combined curve for both, the irradiated and non-irradiated PDPC tiles, can be observed in Fig. 48.

The change over short wavelength periods shown in the PDE curve are caused by reflectivity characteristic known as Fabry–Pérot interferometer (FPI) or etalon, arising at the different silicon-oxide and silicon-nitride based layer interfaces covering the SiPM photoactive areas. The sensor is covered by several layers of silicon-oxide that can give rise to multiple reflections, leading to a constructive or destructive interference, resulting in varying transmission of light through the sensor. Hence, sometimes the sensor may get more light or sometimes less, resulting in high or low PDE.

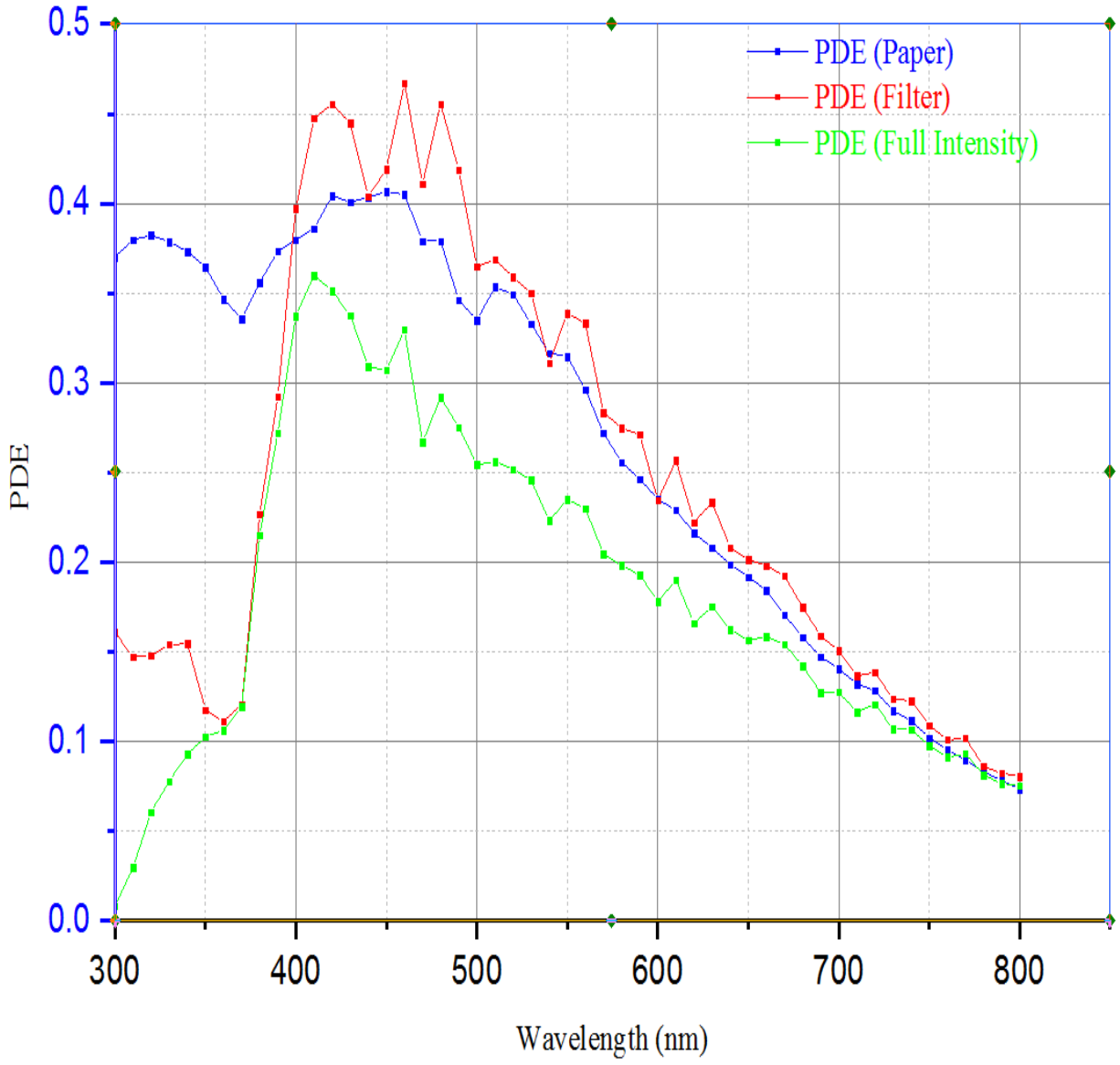

Fig. 47 A comparative PDE curve for detailed analysis of PDE measurements with the use of paper, filter and the full intensity of light, in order to find the ideal measurement set up for finding the corrected PDE of the PDPC (die 10).

We quantified the effects, the cold neutron radiation has on the PDPC and found that under the measurement uncertainty of 16.6 %, there are no significant changes observed. This means that due to the cold neutron irradiation, there is almost no degradation, or a degradation below the measurement uncertainty, in the PDE of PDPC.

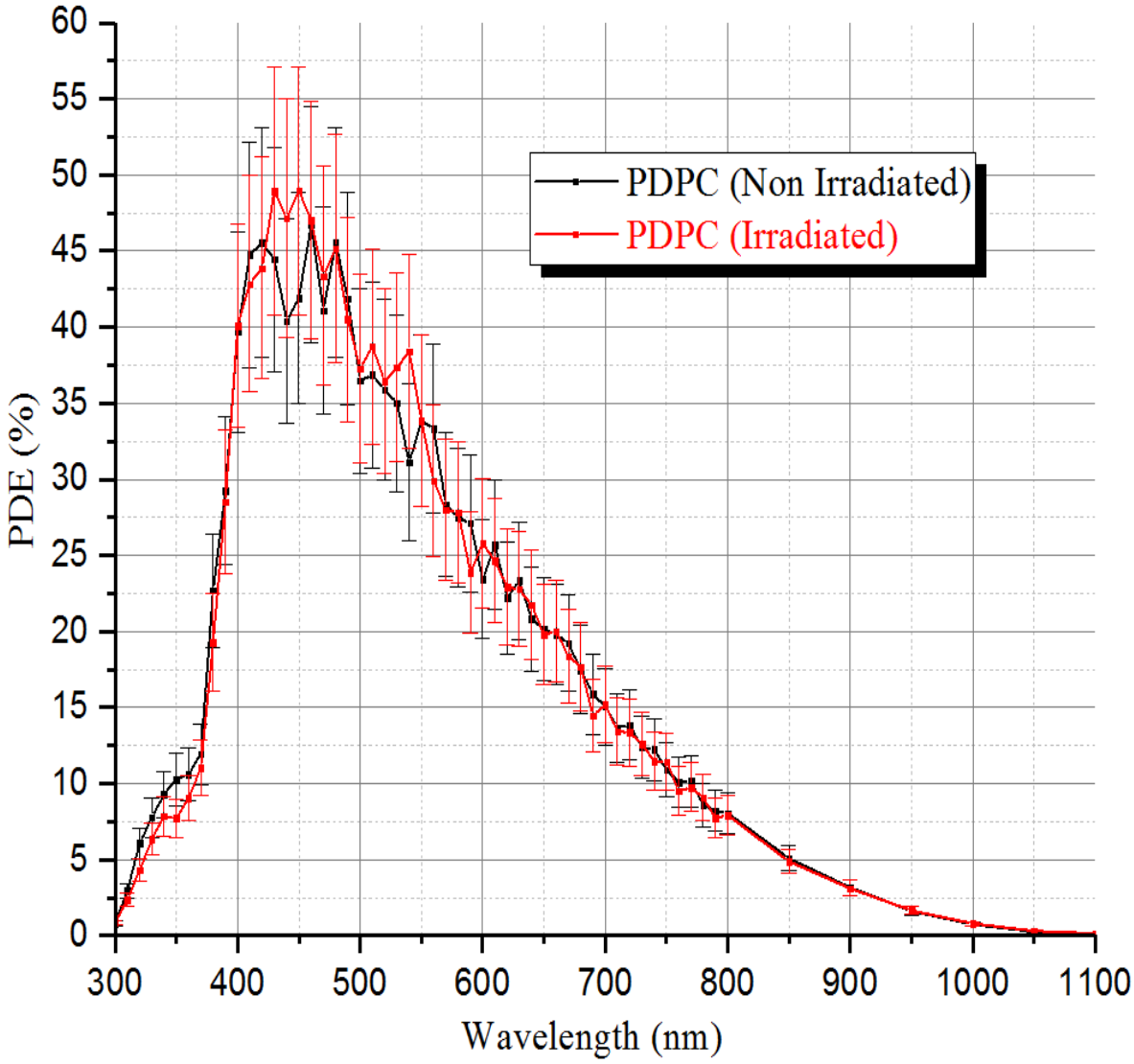

Fig. 48 Graph showing a comparison of PDE between non-irradiated and irradiated PDPC tile (die 10).

4.2 Results obtained for analog SiPM arrays

For avoidance of the measurement difficulties experienced for the PDPC, the wavelength range chosen for the analog arrays was between 400 nm and 800 nm at a measurement step of 20 nm. With the help of electronic measurement system, the breakdown voltages of SiPM arrays for each wavelength of incident light were obtained. The overvoltage for determining the currents in Geiger mode were 2.5V for the SensL and 2.6V for the Hamamatsu, respectively recommended by the manufacturers.

For evaluating the photocurrent, the arrays were firstly measured in dark conditions, and then this dark current were subtracted from each evaluated total current generated by the SiPM array under illumination for each individual wavelength (Eq. 18), holding all other experimental conditions constant, especially the temperature.

Once the light intensity requirements were met to avoid the saturation, irradiance and currents were determined using Eqs.12-15. To evaluate the number of photon detected by the sensor, photocurrent was divided by the gain. In order to avoid measurement complexity, the gain values were taken from the datasheet of the manufacturer (3×10^6 for *SensL* and 1.25×10^6 for *Hamamatsu*). Then, PDE values were calculated using Eqs. 16 and 17.

The first measurements were made on non-irradiated arrays, followed by the irradiated ones. PDE for each pixel was evaluated individually and then the mean value of these results was obtained to find an average PDE for the array. Fig. 49 shows the PDE of 4 pixels for the SensL non-irradiated array, whereas Fig. 50 contains the average PDE. The same curves for the Hamamatsu array are depicted in Figs. 51 and 52. The overall measurement uncertainty, which includes 1.42 % for the used area of light distribution to consider only four pixels, 10.21% for the irradiance, 4.5 % for the certified calibrated photodiode and 6.03% for the electronic measurement system, was finally obtained being 12.76%, using the square-root of the sum of the squares of all individual contributions according to uncertainty propagation rules.

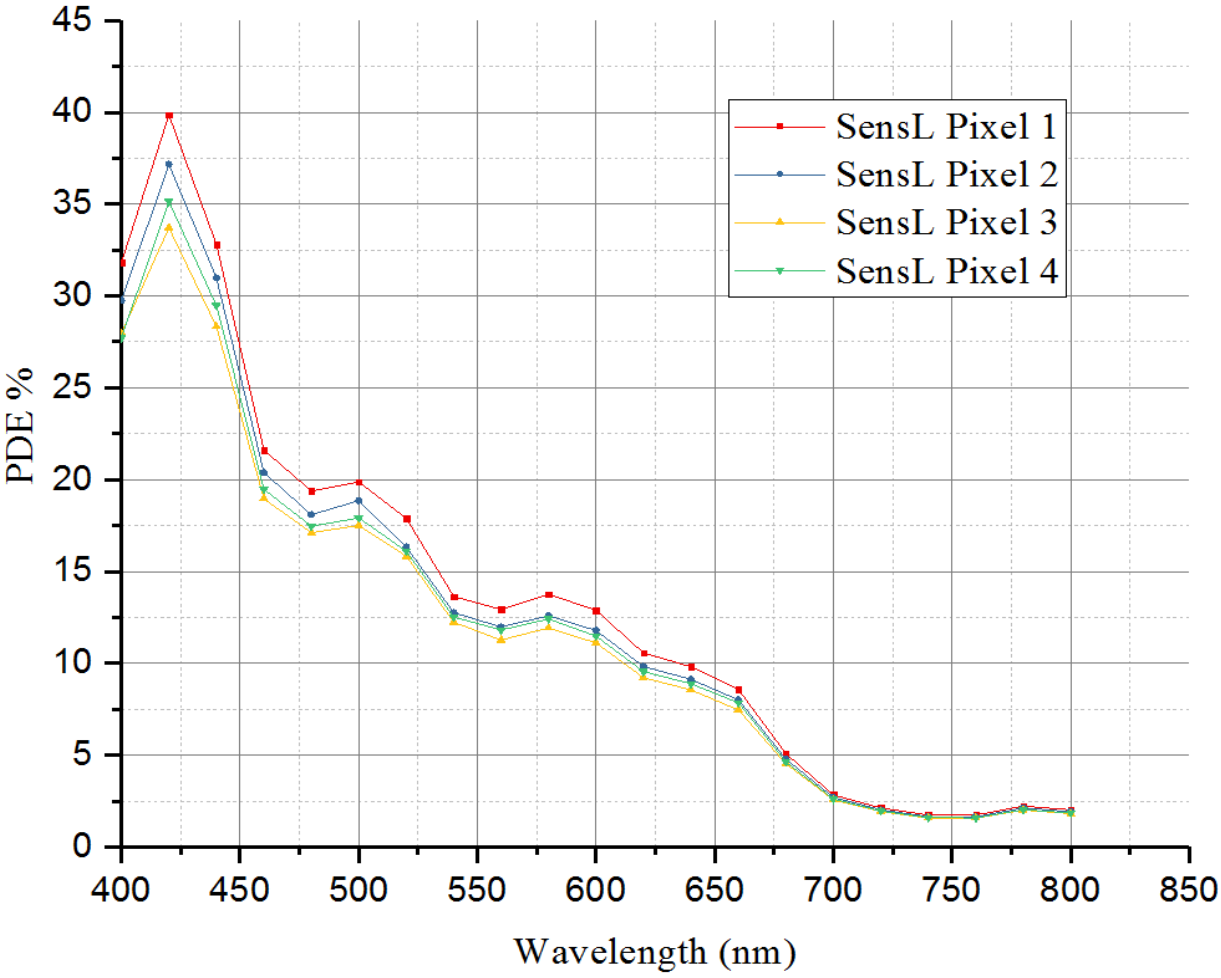

Fig. 49 PDE curve @ 21°C for the four pixels (located at the center of the array) of SensL non-irradiated array.

All measuring steps were performed for the irradiated array also to find the PDE. For the irradiated arrays, the dark currents at room temperature were higher as expected, therefore we cooled them down to -7 ºC to improve the signal to noise ratio and find better measurement results. The PDE outcome was plotted from the obtained measurement data and the average PDE was compared with the avg. PDE of non-irradiated array (see Figs. 53 and 54).

A negligible relative change of 4.9% @ 420 nm was observed between non-irradiated and irradiated array of the SensL with the measurement uncertainty of 12.76%, whereas a change of 11.3% was evaluated for the Hamamatsu (Table 7).

SiPM Array	Relative change (%) in PDE @420nm	Received overall neutron doses
PDPC	3.8	1.85×10^{12} n/cm²
SensL	4.9	1.9×10^{12} n/cm²
Hamamatsu	11.3	6×10^{12} n/cm²

Table 7: Comparison of relative change in PDE for the investigated SiPM array, before and after irradiation with cold neutrons having wavelength of 5Å.

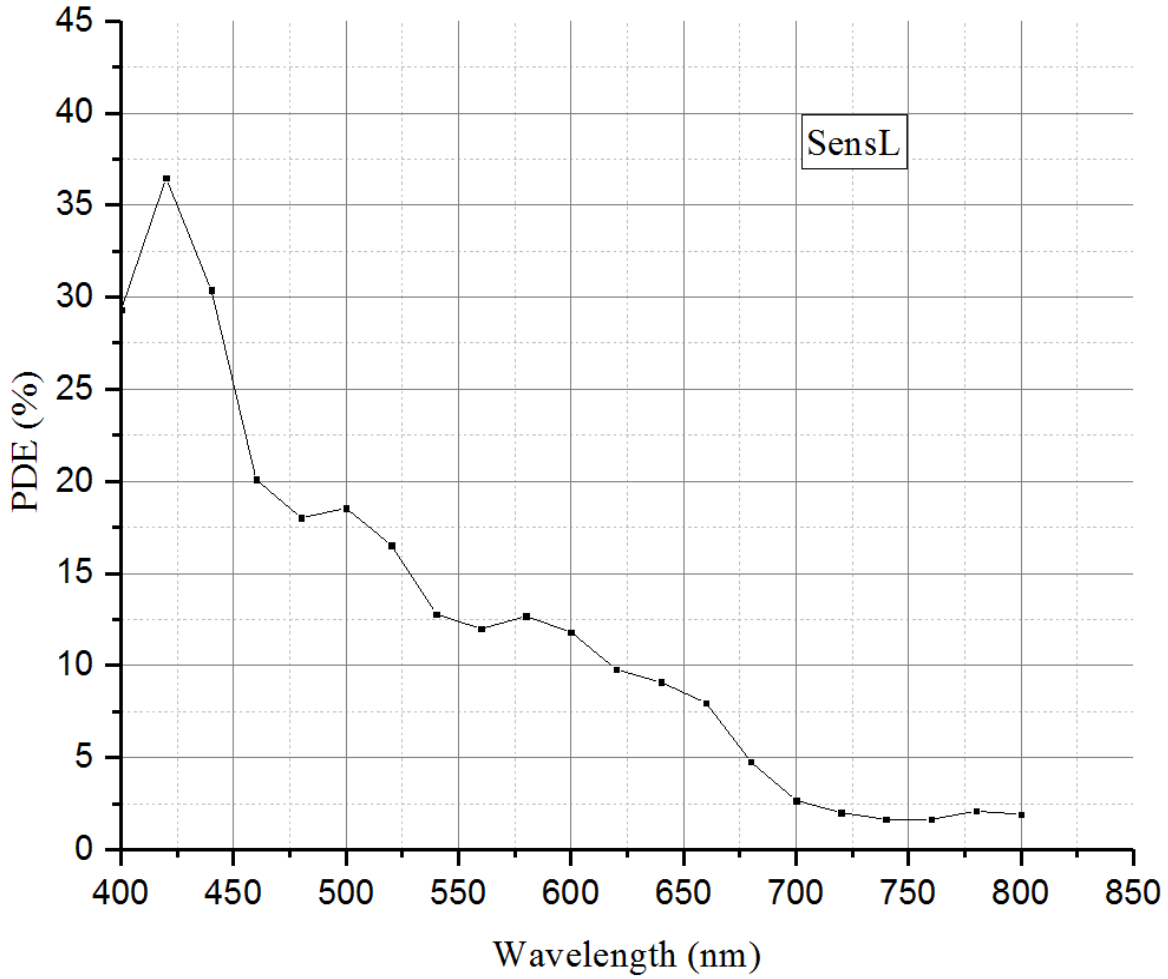

Fig. 50 PDE (avg. of 4 pixels) curve @ 21ºC for the SensL non-irradiated array

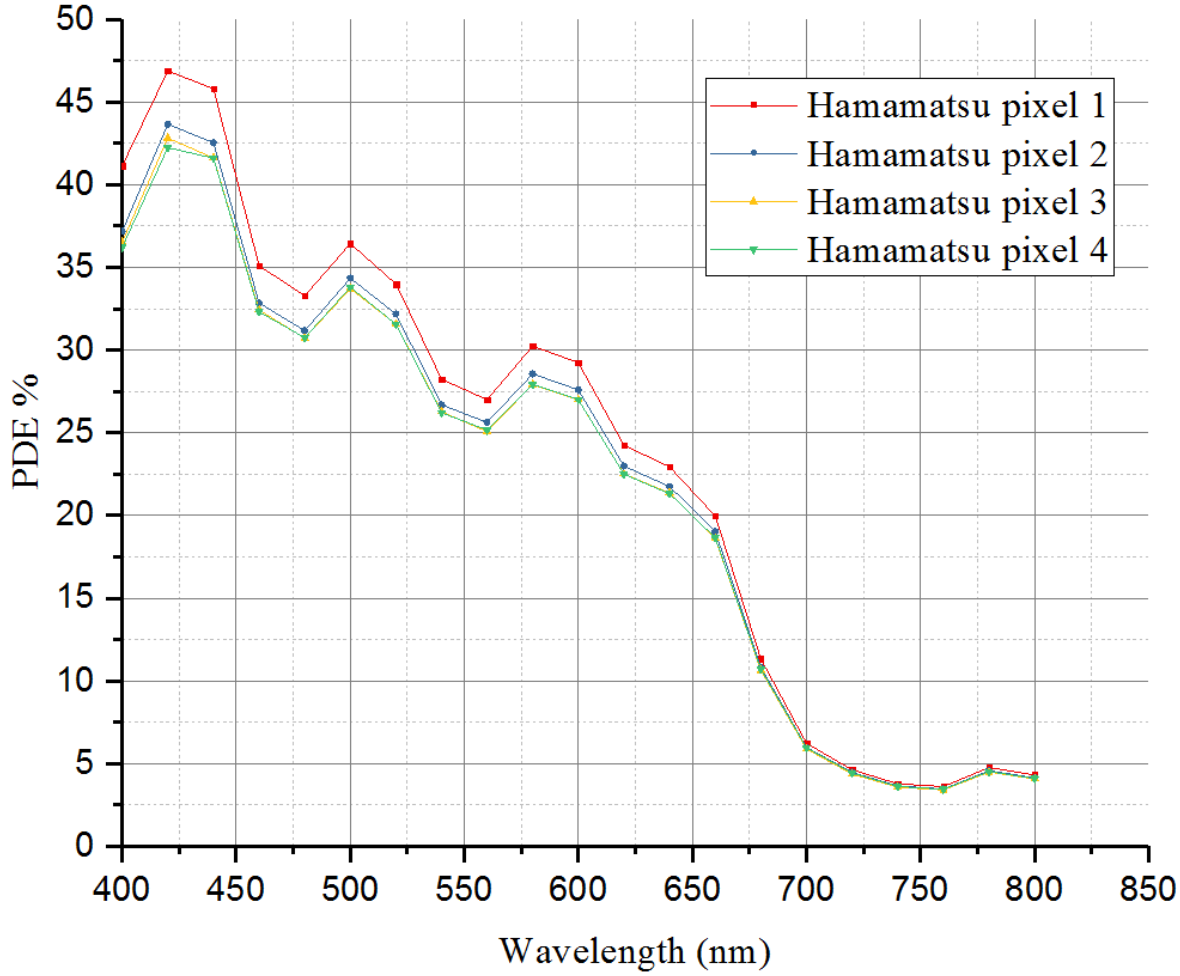

Fig. 51 PDE curve @ 16ºC for the four pixels (located at the center of the array) of Hamamatsu non-irradiated array.

One of the significant effects in the interaction of neutrons with the SiPM, as explained earlier, was shorter recombination life-time of the minority charge carrier caused by increased doping concentration. Due to this, a decrease in diffusion components of the photocurrent is expected. Nevertheless, if the microcell fabrication was done in the form of a p^+ shallow implantation on top of an *n*-well, then the diffusion part of the photocurrent coming from the silicon substrate surrounding this *n*-well equals zero. Hence, no significant difference in photocurrent can be assumed and therefore PDE will remain similar [55].

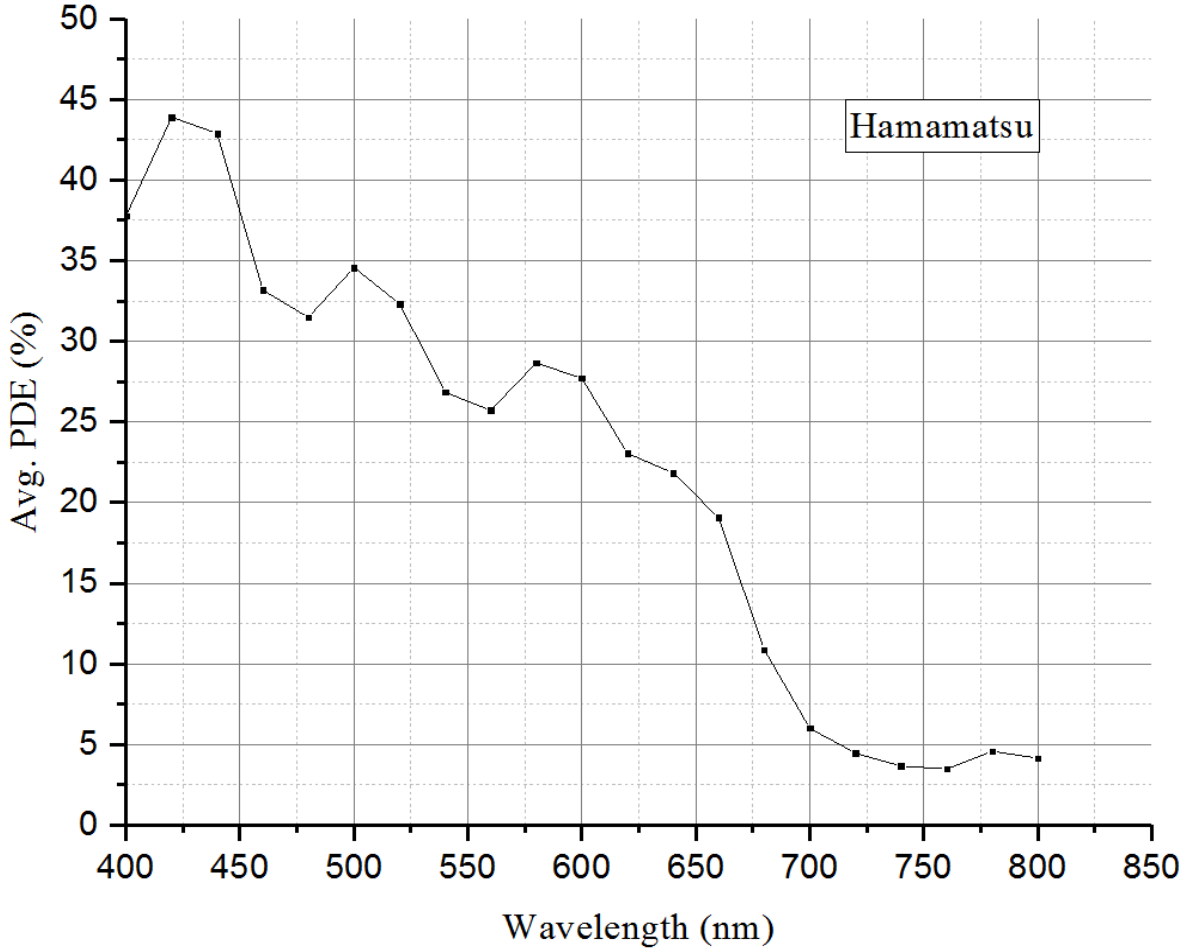

Fig. 52 PDE (avg. of 4 pixels) curve @ 16ºC for the Hamamatsu non-irradiated array.

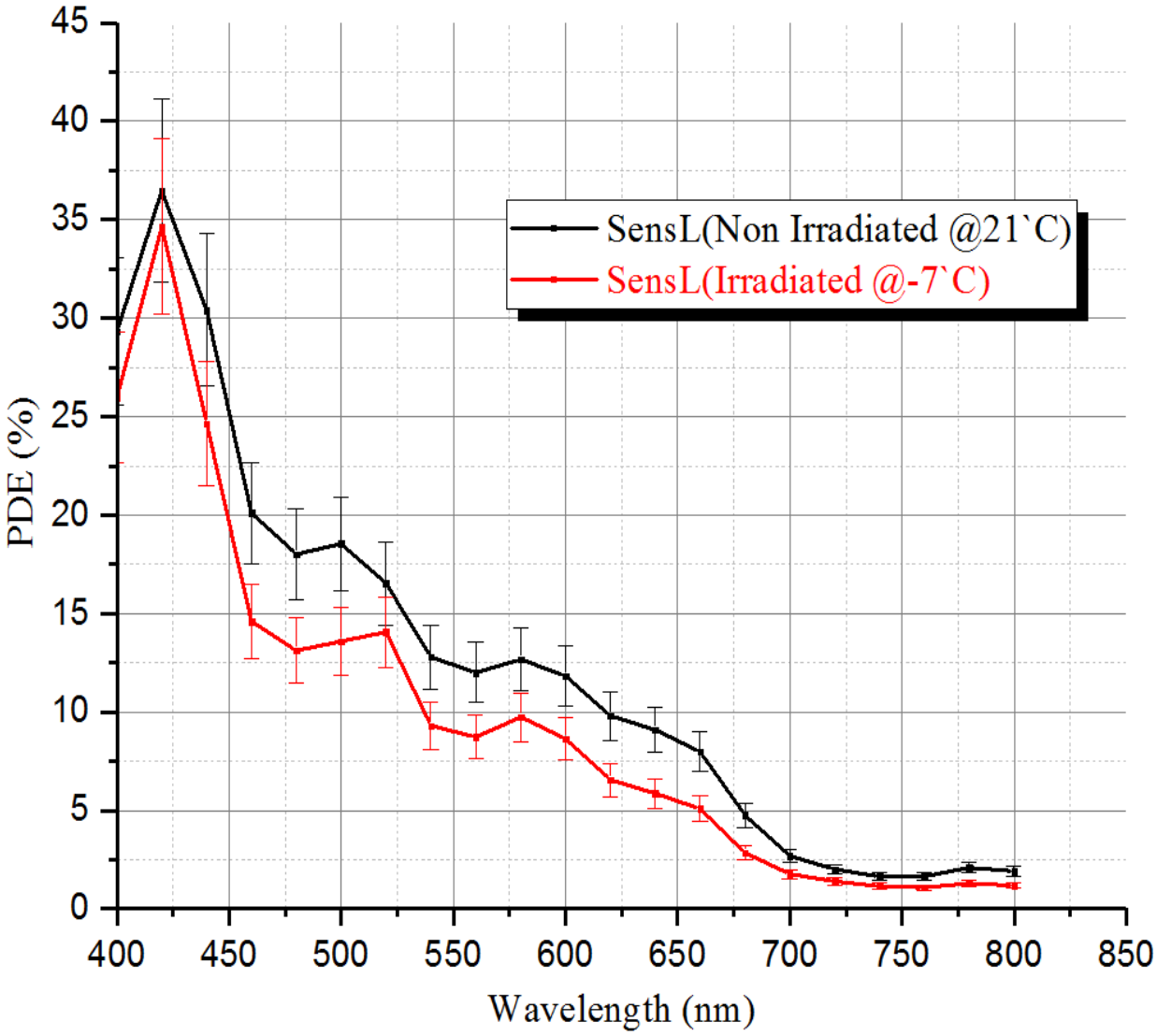

Fig. 53 Graph showing a comparison of PDE (avg. of 4 pixels) between SensL non-irradiated and irradiated array.

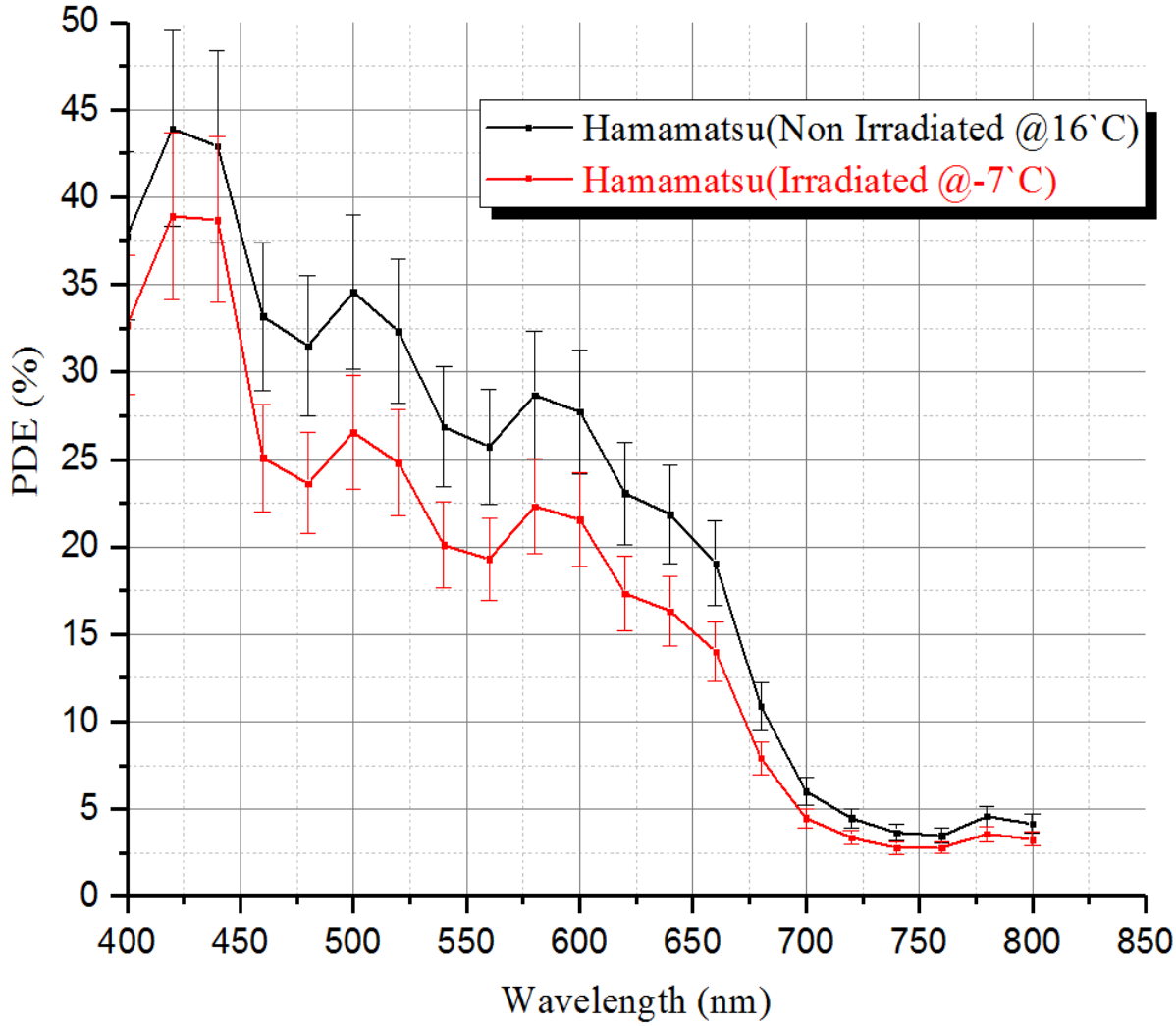

Fig. 55 Graph showing a comparison of PDE (avg. of 4 pixels) between Hamamatsu non-irradiated and irradiated array.

V. Summary and Outlook

In this thesis, assessment for the possibilities of using Silicon Photomultiplier (SiPM) technology in scintillator based neutron detectors for small angle neutron scattering (SANS) experiments has been carried out. Traditionally, photomultiplier tubes (PMTs) have been used in these experiments for photodetection. However, their limitation has motivated us to investigate a compact, robust, rugged, cheap, more efficient and more flexible photodetector that can be used in high magnetic fields at much lower bias voltages.

An evaluation on the base of the photon detection efficiency (PDE) has given us important insight towards this approach. We found that the comparative study of the effects the irradiation with cold neutrons have, at the photon detection performance of three SiPM arrays, produced by the three different manufacturers, namely *SensL, Ireland, Hamamatsu Photonics, Japan, and Philips Digital Photon Counting GmbH, Germany,* shows promising results to explore them further for this kind of applications.

These SiPM arrays show sufficient radiation hardness to rule out any major performance degradation concern, caused by the cold neutrons irradiation. The relative change in PDE observed by us for the analog arrays of *SensL* and *Hamamatsu* were 4.9% and 11.3% respectively, after irradiation with cold neutrons. The digital array manufactured by *Philips DPC* yields a change of 3.8 % only. These variation percentages were only for the photons having a wavelength of 420 nm. To get a better understanding of this behaviour, we tested the SiPM arrays over a wide range of wavelengths extending up to 1100nm in the NIR range and 300nm in the UV part of the spectra.

We did several tests and tried different approaches to get a reliable measurement results and a concrete conclusion. The relatively high overall change in the PDE of analog arrays was probably caused also by the measurement uncertainty and low signal to noise ratios achieved for the obtained results. We put our efforts in this limited period of investigation to increase the signal to noise ratio, but unexpected early saturation of the analog SiPM arrays proved it futile. We were not able to understand this saturation behaviour and hence had to stick with our measurements result. Further investigation of this issue will be carried out in the future.

We would like to emphasise that our systematic uncertainty (up to 16.6%) was too high to deliver a conclusion. Although we have enough evidence to say that the change in PDE, due to prolonged exposure with cold neutrons (wavelength λ_n = 5 Å or energy of E_n = 3.27 meV) up to a dose of 6×10^{12} n/cm^2, is acceptable considering the conditions normally present in SANS experiments and their added application advantages.

We would like to suggest that a more certain measurements should be done to strengthen our results. The area of scope will be in the improvement of the measuring system and methods used focusing on a stable monochromatic light source, having the flexibility in intensity of light with variable focusing areas and finding more precise breakdown voltages by the static measurements or using dynamic measurements. We had observed that the photon counting approach for the response of SiPM arrays proved more reliable than the photocurrent approach.

Another point we would like to add that it will be helpful to consider more pixels, i.e. at least half the number of the total pixels present in the array for the evaluation, so as to get enough data for better analysis. These improvements would definitely give more concrete results for this type of investigations.

References

[1] D.L. Price, K. Sköld, "Introduction to Neutron Scattering", Methods in Experimental Physics, Academic Press, vol. 23, Part A, 1996 pp. 1–97. http://dx.doi.org/10.1016/ S0076-695X(09)60554-2.

[2] Guinier, A. Ann. Phys. Paris., 12, 161–237 (1939).

[3] Probing nanoscale Structures –the SANS toolbox by Boualem Hammouda http://www.ncnr.nist.gov/staff/hammouda/the_SANS_toolbox.pdf

[4] 'ISIS - Neutron Scattering: Materials research for modern life', http://www.isis.stfc.ac.uk/news-and-events/news/2012/neutron-scattering-materials-research for-modern-life13460.html

[5] Search for alternative techniques to helium-3 based detectors for neutron scattering applications Karl Zeitelhack Neutron NewsVol. 23 ,Iss. 4, 2012

[6] http://www.apace-science.com/ast/g_scint.htm

[7] D. Durini et al., "Evaluation of the dark signal performance of different SiPM-technologies under irradiation with cold neutrons" Nuclear Instruments and Methods in Physics Research A 935, 99–109, 2016, http://dx.doi.org/10.1016/j.nima.2016.09.016

[8] Golovin, V, Patent No. RU 2142175, 1998.

[9] Sadygov, Z, Patent No. RU 2102820, 1998.

[10] Neutron Scattering: A Primer by Roger Pynn Los Alamos Science (1990) (www.mrl.ucsb.edu/~pynn)

[11] "CRC Handbook of Chemistry and Physics" (R. C. Weast, M. J. Astle, and W. H. Beyer, eds.), 65th ed., CRC Press, B o a Raton, Florida, 1994.

[12] Tsoulfanidis, Nicholas Measurement and Detection of Radiation (2nd ed.). Washington, D.C.: Taylor & Francis. pp. 467–501 (1995). ISBN 1-56032-317-5

[13] Ninkovic, J, Recent Developments in Silicon Photomultipliers, Nuclear Instruments and Methods in Physics Research A, 580, 1020-1022, 2007.

[14] Webb, P.P., McIntyre, R.J., Conradi, J., Properties of avalanche photodiodes. RCA Rev. 35, 234_278, 1974.

[15] Pansart, J.P., Avalanche photodiodes for particle detection. Nucl. Instrum. Methods Phys. Res. A. 387, 186_193, 1997.

[16] Renker, D., Lorentz, I., Advances in solid state photon detectors. J. Instrum. 4, P04004, 2009.

[17] S. Cova, A. Longoni, A. Andreoni "Towards a picosecond resolution with single photonavalanche diodes", Rev. Sci. Instrum. 52 (3), pp. 408 – 412 (1981)

[18] N. Dinu, Chapter 8, "Silicon Photomultiplier", B. Nabet Photodetectors: Materials, Devices and Applications, 1 edition. Cambridge, UK: Woodhead Publishing, 2015.

[19] España S, Fraile L M, Herraiz J L, Udias J, Desco M and Vaquero J J, Performance evaluation of SiPM photodetectors for PET imaging in the presence of magnetic fields Nucl. Instr. Methods Phys. Res. A 613 308-16, 2010

[20] Buzhan, P, et al., Silicon Photomultiplier and its Possible Applications, Nuclear Instruments and Methods in Physics Research A, 504, 48, 2003.

[21] TN - Intro to SPM Tech.pdf'.http://www.sensl.com/downloads/ds/TN%20-%20Intro%20to%20SPM%20Tech.pdf.

[22] Dalla Betta, G.F., Pancheri, L., Stoppa, D., Henderson, R., Richardson, J., Avalanche photodiodes in submicron CMOS technologies for high-sensitivity imaging. In: Dalla Betta, G.-F. (Ed.), Advances in Photodiodes. InTech, pp. 225_249. 2011

[23] Nicoleta Dinu, Détecteurs SiPM, Ecole microelectronique IN2P3, 24.06.2013

[24] D. Durini, Chapter-2 "Operational Principles of Silicon Image Sensors", High performance silicon imaging: Fundamentals and applications of CMOS and CCD sensors, 1 edition. Woodhead Publishing, 2014

[25] "Technical note MPPC", http://www.hamamatsu.com/resources/pdf/ssd/mppc_kapd9005e.pdf
[26] http://www.iue.tuwien.ac.at/phd/triebl/node20.html
[27] Rutherford, E.; Geiger, H. (1908). "An electrical method of counting the number of α particles from radioactive substances". Proceedings of the Royal Society. Series A. London. 81 (546): 141–161. doi:10.1098/rspa.1908.0065.
[28] Th. Frach et al., "The Digital Silicon Photomultiplier–Principle of Operation and Intrinsic Detector Performance" Nuclear Science Symposium Conference Record, N28-5, 2009
[29]'de_clerq_jarne.pdf',http://www.desy.de/2011summerstudents/2014/reports/de_clerq_jarne.pdf.
[30] R.J. McIntyre, Theory of micro plasma instability in silicon, J.Appl.Phys.32 983–995 (1961).
[31] https://www.electrical4u.com/
[32] N. Dinu, A.Nagai, A.Para, "Breakdown voltage and triggering probability of SiPM from IV curves at different temperatures", Nuclear Instruments and Methods in Physics Research A845 (2017)64–68
[33] A. Otte et al. "Characterization of three high efficiency and blue sensitive silicon Photomultipliers" Nuclear Instruments and Methods in Physics Research A 846 (2017) 106–125
[34] G.Collazuo et al., "Studies of silicon photomultipliers at cryogenic temperatures" Nuclear Instruments and Methods in Physics Research A Volume 628, Issue 1, 1 February 2011,Pages 389–392, https://doi.org/10.1016/j.nima.2010.07.008
[35] A. Lacaita, et al., IEEE Trans. Electron. Devices ED-40 (3) (1993) 577.
[36] H. Spieler : Semiconductor Part 2, SLUO Lectures on Detector Techniques, October 30, 1998, http://www-physicsl.b l.gov/-spieler/SLAC- Lectures
[37] J. Guldberg, ed. (1980) "Neutron-Transmutation-Doped Silicon", Neutron Transmutation Doping of Silicon (Proc. 3rd Int. Conf. Copenhagen, 1980), Plenum Press, NY, USA
[38] Y. Qiang, C. Zorn, F. Barbosa, E. Smith (2013) "Radiation hardness tests of SiPMs for the JLab Hall DBarrel calorimeter", *Nucl. Instr. Meth. A 698*, pp. 234-241, doi:http://dx.doi.org/10.1016/j.nima.2012.10.015
[39] T. Tsang, T. Rao, S. Stoll and C. Woody, "Neutron radiation damage and recovery studies of SiPMs", 2016 JINST 11 P12002
[40] G. O. Fiori (1983) "Neutron Transmutation Doped Silicon: Lattice Damage and Characterization Techniques", Latin American Journal of Metallurgy and Materials, Vol. 3, No. 2, pp. 98 – 105
[41] http://sensl.com/products/c-series/⟨ http://sensl.com/products/c-series/⟩.
[42] http://www.nuclear.gla.ac.uk/~jrma/A2/Tagger/NewFPD/SiPMT/KSX-I50014-E_S12642%20Series%20%283mm%E2%96%A1-TSV%E3%83%BCArray%29.pdf
[43] 'Philips Digital Photon Counting'http://www.digitalphotoncounting.com/wp-content/uploads/PDPC-TEK-Manual-v0.21.pdf
[44] http://aspect-sys.com/
[45] http://www.lot-qd.de/en/
[46] https://www.thorlabs.de/thorproduct.cfm?partnumber=MC2000
[47] http://www.femto.de/en/products/lock-in-amplifiers/module-series-lia-mv-200.html
[48] http://www.smcpneumatics.com/HEC012-W2A.html
[49] ⟨http://mh-powersupplies.com/sites/default/files/downloads/ea_catalogue.pdf⟩.
[50] https://www.meilhaus.de/en/redlab-tc.htm
[51] http://www.ni.com/en-gb/support/model.usb-6343.html
[52] V. Chmill, E. Garutti, R. Klanner, M. Nitschke, J. Schwandt, Study of the breakdown voltage of SiPMs, Nucl. Instrum. Methods Phys. Res. Sect. A Accel. Spectrometers, Detect. Assoc. Equip. (2016) http://dx.doi.org/10.1016/j.nima.2016.04.047

[53] N. Serra, G. Giacomini, A. Piazza, C. Piemonte, A. Tarolli, N. Zorzi, Experimental and TCAD study of breakdown voltage temperature behavior in +np /SiPMs, IEEE Trans.Nucl.Sci.NS-58(2011)1233–1240. http://dx.doi.org/10.1109/
[54] E. Garutti, M. Ramilli, C. Xu,W. Hellweg, R. Klanner, Characterization and X-ray damage of Silicon Photomultipliers, Proc. Sci. PoS(TIPP2014)070 (2014).
[55] D. Durini et al."Assessment of the photodetection performance of different silicon photomultiplier technologies under irradiation with cold neutrons" poster, Nuclear Science Symposium and Medical Imaging Conference (NSS/MIC), Strasbourg, France, 29.10 - 05.11. 2016.

Jül-4404
November 2017
ISSN 0944-2952